Extensions of the Principal Fiber Bundle Model for Locomoting Robots

Tony Dear

CMU-RI-TR-18-41

August 2018

The Robotics Institute
School of Computer Science
Carnegie Mellon University
Pittsburgh, PA 15213

Thesis Committee

Howie Choset (chair)
Matthew Travers
Scott Kelly, UNCC
Koushil Sreenath, UC Berkeley

Submitted in partial fulfillment of the requirements for the degree of Doctor of Philosophy in Robotics.

Abstract

Our goal is to establish a rigorous formulation for modeling the locomotion of a broad class of robotic systems. Recent research has identified a number of systems with the structure of a *principal fiber bundle*. This framework has led to a number of tools for analysis and motion planning applicable to various robotic configurations in different environments, but it also requires a number of assumptions that limit its usefulness to certain "idealized" systems. Systems that cannot be fully described with a principal fiber bundle or cannot make full use of the subsequent tools include those whose joints are not fully controllable, those with control inputs or dynamics external to their mechanism, and those whose external configurations do not form a symmetry group. In addition, the motion planning techniques derived from this structure have traditionally assumed a mapping from internal joint configurations to external position configurations. The reverse of this mapping will be discussed in this thesis, as well as the analysis and solutions for problems violating each of the above assumptions in turn. For each case, we introduce one or two motivating examples of robotic systems and discuss novel locomotive characteristics that do not previously appear under the standard assumptions. This thesis expands the applicability of the principal fiber bundle model, as well as derivative tools for analysis and motion planning, to a larger variety of locomoting systems.

Acknowledgments

I would first like to thank my advisor, Howie Choset, for taking me as a student and helping me develop my technical and professional scholarship. My committee members Scott Kelly, Matthew Travers, and Koushil Sreenath have also contributed to this endeavor in different ways, through classes, intellectual discussions, and hanging out at conferences. The weekly Skype meetings have been particularly memorable, whether they consisted of debates about geometric notation or linguistics tidbits from Scott. Finally, I am particularly grateful to Howie for recognizing my interests in pedagogy and giving me opportunities for meaningful work there alongside my research.

So many members of the Biorobotics Lab have shaped my graduate experience over the years. Past and concurrent doctoral students Matt, Dave, Chaohui, Glenn, Arun, and Julian have been impeccable role models, invaluable sounding boards for ideas, and wonderful socializers (I will especially miss those Udipi trips with Arun). This thesis is also due to the tireless efforts of the master's students with whom I worked, including Jaskaran, Blake, Hadi, Baxi, and Jin. Of course, my work stands on the shoulders of my predecessors Elie and Ross, and I must give a special acknowledgment to both Peggy and Suzanne for making mundane matters as lighthearted as can be.

It would have been impossible for me to have made it this far without the support of my friends. The "Wightmen" were solid housemates through my first year, while Team Winstinct has been an awesome and ruthless raid group in the past year. Outside Pittsburgh, I have been lucky to meet many great people in places like New York, SoCal, and the Bay Area. As for the friends who have had the patience to keep me in their lives despite being three timezones away—Jeff Z., Belle, Henry, William, Jason, Dustin, Jess, Wilson, Lincoln, Steven, Ben, Paul, Chasel, Jeff L., Sean, Spenser, Connie, Sam, Zoey, Jeff S.—I look forward to sharing many more life experiences with all of you.

No acknowledgment is complete without my family, who have raised me to work hard and pursue success. Having been away from home for so long, I am all the more grateful to my parents Bobbie and Lily for supporting my interests and life trajectory. With the both of us working on furthering our education and careers, my sister Annie always has interesting anecdotes about her experiences and social life. Whenever I visit home, the sight of my relatives Lena, Rose, *yi ma*, *yi zoeng*, Jenny and her family, Linda and Frank, Peter and Irene, and Sally and Celina has always given me a warm feeling of comfort and familiarity. And although they are not all with me, I know that my grandparents would have been proud to see me where I am today.

Finally, no mere words can express my feelings toward Yi, the bedrock of my last five plus years in Pittsburgh. I simply could not have completed this endeavor without his companionship and support. As we both move on to the next stage of our careers, I am confident that even greater success and advancement lie in the future for the both of us.

Dedicated to *ye ye*, *ngen ngen*, *gong gong*, *po po*, and Mo

Contents

List of Figures

Chapter 1

Introduction

For many robots and biological organisms, locomotion is a fundamental aspect of how they operate in the world. While the nuances of locomotion across different systems vary, the goal is generally the same—the agent exploits the underlying structure of its body and the environment to effect movement in a desired way. This structure is mathematically captured in the *configuration spaces* of these systems, and by identifying common geometric elements of arbitrary systems, one can produce analysis and synthesis methods that are adaptable to seemingly disparate problems. But while such techniques are powerful, they are currently limited in implementation due to the assumptions that traditionally define them. For example, that a given system has unrestricted control over its internal degrees of freedom is a common assumption in both the robotics and biological literature, such as the direct control that a horse can exert over its legs. The objective of this thesis thus seeks to greatly expand the scope of systems that can be treated using analysis and motion planning tools from and inspired by geometric approaches to locomotion science.

More specifically, robotic locomotion research has borrowed from differential geometry the structure of a *principal fiber bundle* to model the configuration space of a variety of robots. This bundle distinguishes between a robot's internal or joint configurations—the *base space*—and the robot's external position and orientation—the *fiber space*. Base trajectories can be mapped to fiber trajectories through a time-independent mapping called a *connection*. This machinery has led to a number

of novel tools to conduct analysis, for example identifying describing physical phenomena or assessing controllability, and engineer the design of gaits, cyclic paths in the base space, for motion planning.

However, the tradeoff for such utility is that the applicability of the principal fiber bundle framework and the aforementioned tools is strictly limited to systems for which all of the degrees of freedom of the system can be neatly categorized into either the base space or the fiber space. In prior work, when coordinating the internal variables to produce motion in the external ones, the base degrees of freedom are typically fully controlled. In addition, the fiber space must correspond to a *symmetry group*, which means that system properties, such as kinetic energy, do not depend on where the system is located in the associated space.

While the above assumptions may hold or approximately hold for a number of "idealized" systems, we assert that these make up only a portion of a larger landscape of locomoting systems. For example, a subset of the joints of a multi-link robot may fail during operation and become passive, or control may be applied in the form of a flow field rather than internally to the robot's joints. In these cases, in addition to using the knowledge of how the robot's internal joint motions effect locomotion in the external degrees of freedom, the robot must also coordinate the physical interaction between the uncontrolled internal degrees of freedom and any possible external forces, allowing it to indirectly control the joint behaviors that lead to desired locomotion. The goal of this thesis is to consider how the classical notion of the principal fiber bundle structure must thus be recast to expand the current landscape of applicable systems, introduce new design and analysis techniques to be used with elements of the established theory, and perform validation through simulation and experiments with representative robots in each case.

1.1 Locomotion

The problem of locomotion is inherently broad and appears not just in robotics, but also in biology and moving components in general mechanical systems. While the

nuances of locomotion in the different fields may vary, the goal is generally the same—the engineer or agent utilizes the knowledge and structure of the particular system to effect movement in the world in a desired way. The diverse modes of locomotion found in nature have inspired a parallel development in robots and mechanical systems, inviting rich opportunities for analysis.

Among terrestrial biological organisms, many locomote using legs or limbs that support the body from the ground [33, 68]. The number of limbs may vary, and the same is true for *biomimetic* robots based on examples from nature [83]. Bipedal robots have rapidly improved in performance and functionality, with locomotion planning ranging from higher-level walking patterns [41] to lower-level feedback control [100]; bipedal mechanisms also benefit by being dynamically stable due to their passive dynamics [20, 58]. On the other hand, quadrupedal robots are usually statically stable and can adaptively synthesize gaits [38] on many different terrains [30, 48]; BigDog [84] from Boston Dynamics was a prominent example that can locomote on rough uneven terrain. Finally, as the number of legs and thus degrees of freedom increases to six (or more), locomotive control of these hexapod robots has relied on central pattern generators [19] to produce high-level gaits and distributed control [8, 29] to adapt to different environments. While most hexapods in nature are found in insects, six legged robots have appeared in different sizes and are capable of fast and robust motions [94], a notable example being the RHex robot [87].

There is just as much biological diversity to be found in terrestrial organisms that locomote without legs at all, inspiring a field devoted to snake-like and slithering robots [39]. These robots are often termed *hyper-redundant mechanisms* [15, 16], because they have many more degrees of freedom than legged robots, allowing for flexible adaptability to terrains and navigation in tight spaces. Two classes of such robots in recent development include so-called *active cord mechanisms* [64, 65], composed of serial chains of segments with passive wheels attached to each, and snake robots that locomote directly with their bodies over the ground, such as the unified modular snake robot [102, 103]. Gaits for lateral undulation have been produced for the former [65], while the latter have also been shown to be able to execute sidewinding [12] and

sinus-lifting gaits [40].

Organisms and machines that locomote in fluids often do so via whole-body interactions with the surrounding medium [14], like those of terrestrial undulating mechanisms. The simplest models of these swimming agents consider deformable cylinders and circles that can accelerate from rest in ideal fluids [62, 86] as well as low Reynolds number fluids [9, 93]; motion planning for these systems can be cast as control problems [46, 47] optimizing for locomotive efficiency [2, 92]. While these models may appear primitive, they work well for microorganisms, whose locomotion is characteristic of low Reynolds number models [51, 80, 97]. The hydrodynamics governing these systems also lead to non-trivial interactions between multiple bodies [42, 79] that can be observed in bacteria and cellular systems [49], such as phase synchronization during motion [32, 81]. On the other hand, articulated mechanisms, for example composed of multiple rigid bodies, can achieve locomotion without requiring deformable components [3, 7, 31, 59, 96]. The gaits that emerge from these models are often reminiscent of those used by macroscopic swimmers, namely fishes and cetaceans, whose locomotion has been considerably addressed in biology [71, 88, 98, 104]. The robotics community has subsequently addressed the mechanics and control of fishlike robots [18, 45, 63]. Finally, more intricate swimming mechanical systems with different types of degrees of freedom [52] have also recently received attention, such as a hydrofoil with an internal rotor [44].

There is a miscellany of robots that are not directly biomimetic, but whose locomotion can be described using many of the geometric tools summarized in the next section. Many of them move using passive wheels that provide traction on the ground to provide no-slip nonholonomic constraints. Systems in this category range from the canonical two-wheeled robot [46] and multi-trailer system [85] to the active cord mechanisms based on snakes [64, 65], from toys like the Snakeboard [77] and the Robotrikke [17] to more exotic systems such as the ballbot [69], Chaplygin beanie [45], landfish [24], and all their variants. Given the prevalance of these systems, a large literature exists on aspects of their control [10] and motion planning [53, 67, 76]. Analogous to nonholonomic constraints governing the locomotion of mechanical sys-

tems is the principle of momentum conservation, which either works in tandem with the constraints or determines the systems' behavior completely, the latter describing free-floating robots and satellites [21, 70, 99].

We have summarized what appears to be an exposition of work in disparate areas, but it is desirable to find structures or techniques that are common to multiple problems. This would allow for a deeper understanding of, for example, relationships between certain robot morphologies and their biological counterparts, so that knowledge on one side can be carried over to the other. Or this would allow for the application of similar motion planning techniques to multiple classes of robots.

1.2 Geometric Mechanics

In recent decades, techniques and methods from geometric mechanics have been a popular way to model and control mechanical systems. A key idea is that of *symmetries* in a system's configuration space, which allows for the *reduction* of the equations of motion to a simpler form. This has been addressed for general mechanical systems by Marsden [55, 56, 57], as well as nonholonomic systems by Bloch [11] and Ostrowski [72]. For locomotive systems, geometric reduction is often leveraged in tandem with a decomposition of the configuration variables into actuated shape variables, describing internal system configuration, and position variables. If such a splitting is possible, then the configuration space often takes on a *fiber bundle* structure, whereby a mapping called the *connection* relates trajectories between each subspace. Analysis of the connection can then give us intuition into ways to perform motion planning and control of the system [46, 74].

Much of the progress in the geometric mechanics of locomotion is predicated on the assumption that the symmetries of a system coincide exactly with the external, or position, degrees of freedom. Following work by Ostrowski [75], Shammas elucidated a spectrum of systems whose motion and mathematical structure are governed by constraints only, momentum conservation only, or a mixture of both [89, 90, 91]. The former two categories are identified to be *kinematic*, or drift-free, while the last

category of systems are known as *dynamic*. For systems with two shape variables, Shammas proposed visualizations of a local form of the connection to aid in motion planning without requiring the parameterization of gaits. Hatton significantly improved this visual method for kinematic systems by optimizing coordinate choice to reduce the misleading effects of noncommutativity in the configuration space [35, 36].

More recently, there has been investigation of more general aspects of mechanical systems from a geometric perspective. For example, Kelly showed that a system governed by both momentum conservation as well as viscous dissipation exhibits two separate connections in its equations of motion [47], and certain means of locomotion result in a phenomenon known as *self-recovery* [25]. There has also been a push to make the geometric models more realistic by including skidding and friction, particularly for nonholonomic systems [6] such as the rolling disk [5] and the three-link kinematic snake [27]. Finally, we have also presented a geometric exposition of differential flatness [26], allowing for yet another means of nonlinear control of these systems.

1.3 Contributions

This thesis furthers the usefulness of geometric mechanics and the associated nonlinear control and motion planning techniques for locomoting systems. Traditionally, the configuration space of an applicable locomoting system must have a particular principal fiber bundle structure, wherein a splitting exists between a shape and a position space, as described previously. Simultaneously, however, the system must have symmetries in all of its position variables (and since the position variables often form a Lie group, they are *group-invariant*), and the system is fully actuated in all of its remaining shape variables. Our work seeks to relax some of the above requirements to broaden the landscape of relevant systems and elucidate the usage of both the established techniques as well as some new approaches based on nonlinear control for motion planning.

Chapter 2 introduces the necessary mathematical background for this work, mainly

based on geometric mechanics as applied to locomotion. We introduce structures such as groups, Lie algebras, manifolds, and fiber bundles. We also present the standard equations of motion, along with the different variations of the connection, and discuss how it is broken down for kinematic and mixed dynamic systems. We also summarize the usage of connection vector fields and connection curvature plots for visual motion planning in the shape space.

Chapter 3 introduces the modifications to the basic fiber bundle in order to remove the assumptions listed above by either partitioning the existing structures or amending them with vector fields or a subset of variables. We show that these modifications are general enough for a number of locomoting system classes that do not meet all of the standard assumptions. We also show that each of these classes can be identified based on the new structure's mapping relationships with the original fiber bundle part of the configuration space.

In Chapter 4 we present a detailed analysis of a multi-link nonholonomic snake robot with three or more links and one or more passive joints. Depending on the combination of joint and input configurations, we are able to derive either a kinematic or dynamic model for such a robot. In the kinematic case, we obtain different models of the robot's locomotion based on the relative locations of the actuated joints; the system's original geometric structure will inform us how to extract "useful" locomotion while avoiding stationary configurations in extra joints. With the dynamic model, we utilize joint harmonics and phase analysis to describe the passive shape trajectories and inform motion planning in tandem with the original connection picture.

Chapter 5 continues to utilize the example of a nonholonomic snake robot in the context of external actuation and dynamics. A simple example is subjecting it while completely passive to a constant external force field, such as gravity. A more complex scenario arises if we are able to control the ambient medium that affects the system, for example via coupling to an underlying movable platform. This system helps us illustrate the idea of a "stratified" fiber bundle with multiple fibers pertaining to one system. We show how the problem of external actuation can be easily solved using this structure, and how the problem of symmetry preservation comes into play

depending on the external inputs' frame of reference. We close the chapter by briefly discussing the impact of dissipative friction on the geometric structure of locomoting systems, namely the dynamic snakeboard.

In summary, we expand the applicability of the principal fiber bundle model, as well as derivative tools for analysis and motion planning, to a larger variety of locomoting systems. This will allow for greater integration with other classes of techniques used in the motion planning and control communities, particularly for complex systems that may benefit from both the analytical methods of this thesis as well as empirical methods from these fields.

Chapter 2

Mathematical Background

We begin by reviewing the necessary geometric mechanics and motion planning background for this thesis. We first devote a section to relevant concepts from differential geometry, which allows us to define the principal fiber bundle in the abstract sense. We then turn our attention to the Lagrangian mechanics formulation, starting with the Euler-Lagrange equations and then defining symmetries in order to perform a reduction process. We end up modeling the configuration space of a mechanical system as a principal bundle along with a connection mapping. Finally, we summarize the recent work in algebraic and visual analysis of the connection form for motion planning in the configuration space of a mechanical system, describing tools such as connection vector fields and curvature functions, as well as higher-order approximations.

2.1 Differential Geometry

The configuration space of a mechanical system often contains a subset of degrees of freedom that make up a *Lie group*. This Lie group can be used to model physical motions of a rigid body, where motions correspond to group *actions*, and configuration velocities corresponding to the degrees of freedom live in a *tangent space*. By defining these structures and the corresponding maps associated with the configuration variables, we may be able to identify the entire configuration space with a *principal fiber bundle* structure. This section will introduce these ideas at a high level, but also

grounded with examples for physical intuition. For a more in-depth coverage of these concepts, we refer the reader to [4, 43, 66].

2.1.1 Lie Groups and Group Actions

A *group* $(G, *)$ is a set G with a map $* : G \times G \to G$ that satisfies the four properties of closure, associativity, identity, and inverse. The latter two properties give rise to an identity element e of G, such that $e = gg^{-1}$. If the map $*$ is commutative, *i.e.* for $g_1, g_2 \in G$ we have $g_1 * g_2 = g_2 * g_1$, then the group is *Abelian*. The Cartesian product of two groups $(G_1, *_1)$ and $(G_2, *_2)$ is a *direct product group* $(G, \cdot) = (G_1 \times G_2, \cdot)$.The new map $\cdot$ applies the maps $*_1$ and $*_2$ to the respective group elements. Furthermore, if G_1 and G_2 are Abelian, then so is $G_1 \times G_2$. In this document we may write G as a shorthand for $(G, *)$ and $g_1 g_2$ to denote $g_1 * g_2$.

If a group $(G, *)$ is also a differentiable manifold, then G is known as a *Lie group*. Specifically this requires that the associated map $*$ as well as the inverse map to be differentiable. Two important examples of Lie groups that are relevant for rigid body motion are $\mathrm{SO}(n)$ and $\mathrm{SE}(n)$, both with the operations of matrix multiplication. The *special orthogonal group* $\mathrm{SO}(n)$ is defined as

$$\mathrm{SO}(n) = \{R \in \mathbb{R}^{n \times n} : RR^T = I^{n \times n}, \det R = 1\}$$

and corresponds to the group of rigid rotations. The set elements R are also known as rotation matrices. The *special Euclidean group* $\mathrm{SE}(n)$ is defined as

$$\mathrm{SE}(n) = \left\{ \begin{pmatrix} R^{n \times n} & p^{n \times 1} \\ 0^{1 \times n} & 1 \end{pmatrix} : p \in \mathbb{R}^n, R^{n \times n} \in \mathrm{SO}(n) \right\}$$

and corresponds to the group of rigid translations and rotations in n-dimensional space.

Given a Lie group G and an arbitrary set Q, a *left action* of G on Q is a smooth mapping $\Phi : G \times Q \to Q$ such that

1. $\Phi(e, q) = q$ for all $q \in Q$,

2. $\Phi(g, \Phi(h, q)) = \Phi(gh, q)$ for all $g, h \in G$ and $q \in Q$.

As a shorthand, we may write the action as $\Phi_g : Q \to Q$, such that $\Phi_g(q) = \Phi(g, q)$. A physical example of a group action is that of a rigid body transformation, such as a rotation or translation, of a robot.

We note that in the above definition of a group action we assumed that Φ_g plays the role of a *left action* L_g, since Φ_g acts on the group part of the configuration on its left. It is also possible to define a *right action* R_g in a similar manner, such that $R_g(R_h q) = R_{hg} q$. We will not make much use of this mapping, except in the definition of the adjoint map in the following subsection.

2.1.2 Lifted Actions and Lie Algebras

We can define the *tangent space* $T_q Q$ of a manifold Q at a point q as the vector space spanned by the tangent vectors to all curves on Q passing through q, at q. Vectors that live in the tangent space often correspond to velocities of trajectories on the manifold. If an action of a group G acts on Q, then we can also define a *lifted action* $T_q \Phi_g$ as

$$T_q \Phi_g : T_q Q \to T_{\Phi_g q} Q.$$

Thus, the action maps between points on Q, while the lifted action maps between the corresponding velocities.

If we consider the action and lifted action of a group G on itself, then two important examples of lifted actions are $T_g \Phi_{g^{-1}}$, which maps from $T_g G$ to $T_e G$ (the tangent space at the identity), and $T_e \Phi_g$, which maps from $T_e G$ to $T_g G$. In fact, $T_e G$ is often identified with the *Lie algebra* of the group $\mathfrak{g}$. Like $T_e G$, $\mathfrak{g}$ is a vector space, but with the additional requirement that it posseses a *Lie bracket* operation $[\cdot, \cdot] : \mathfrak{g} \times \mathfrak{g} \to \mathfrak{g}$ that satisfies bilinearity, skew commutativity, and the Jacobi identity. It is often desirable to perform analysis in $\mathfrak{g}$, since it has a linear vector space structure.

A special mapping can be defined on the Lie algebra itself. Consider the *inner automorphism* $I_g : G \to G$, defined as $I_g(h) = ghg^{-1}$. This applies a left action of g

and a right action of g^{-1} on h. This expresses a notion of the non-commutativity of the group action, since I_g is very often not equivalent to the identity map. If we now take the tangent of this map at the identity of the group, *i.e.*,

$$T_e I_g : T_e G \to T_{geg^{-1}} G,$$

then we have defined an automorphism on the Lie algebra, since that is associated with the above tangent space. We call this the *Adjoint map* and denote it $\mathrm{Ad}_g : \mathfrak{g} \to \mathfrak{g}$.

In addition to using the lifted action to map between the Lie algebra and tangent spaces on the group, we can also associate group configurations to an algebra element. The *exponential map* is an operation that takes an element in the Lie algebra $\xi \in \mathfrak{g}$ and maps it to the group element $g = \exp(t\xi)$. g is the result of flowing along $T_e \Phi_g \xi$ for time t with initial velocity ξ.

As an example of the above ideas, the Lie algebra of the special orthogonal group SO(3), the group of 3D rotations, is denoted so(3) and is defined as

$$\mathrm{so}(3) = \{\hat{\omega} \in \mathbb{R}^{3\times 3} : \hat{\omega}^T = -\hat{\omega}\}.$$

This is simply the set of 3 by 3 skew-symmetric matrices and is a linear, vector-space representation of an angular velocity. Conversely, given an angular velocity and an angle θ, the exponential map recovers the group element

$$\exp(\theta\hat{\omega}) = I + \hat{\omega}\sin\theta + \hat{\omega}^2(1 - \cos\theta),$$

which is the rotation matrix about the angular velocity vector ω by an angle θ.

2.1.3 Principal Fiber Bundles

Suppose that we have a manifold Q and a subspace B, and define the *fiber* G such that $B = Q/G$. Suppose also that we have a *canonical projection* mapping $\pi : Q \to B$. If π is differentiable and $Q = G \times B$ locally, then we refer to Q as a *fiber bundle* with *base space* B and *fiber space* G. If $Q = G \times B$ globally, then the bundle is *trivial*; if

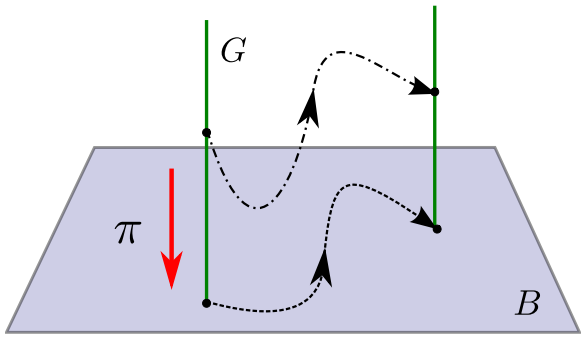

Figure 2-1: A typical visualization of a fiber bundle with base space B, fiber G, and a projection mapping π from from the full bundle Q down to B.

G has a Lie group structure, then the bundle is *principal*.

If we consider the lifted map $T\pi : T_qQ \to T_{\pi(q)}B$, then we can partition T_qQ as follows. Define the *vertical space* as

$$V_qQ = \ker(T_q\pi)$$

and the *horizontal space* as the complement of the vertical space such that

$$T_qQ = V_qQ \oplus H_qQ.$$

This direct sum decomposition of the tangent space means that any tangent vector v_q can be written as a linear combination of vertical and horizontal components as

$$v_q = \text{hor } v_q + \text{ver } v_q,$$

where $v_q \in T_qQ$, hor $v_q \in H_qQ$, and ver $v_q \in V_qQ$.

In the same way that the exponential map takes Lie algebra elements to a group element, we can take a single Lie algebra element ξ and define a vector field ξ_Q everywhere in the bundle. The vector field ξ_Q is known as the *infinitesimal generator* of the corresponding group action Φ due to ξ and is given by

$$\xi_Q(q) = \frac{d}{dt}\Phi(\exp t\xi, q)|_{t=0}.$$

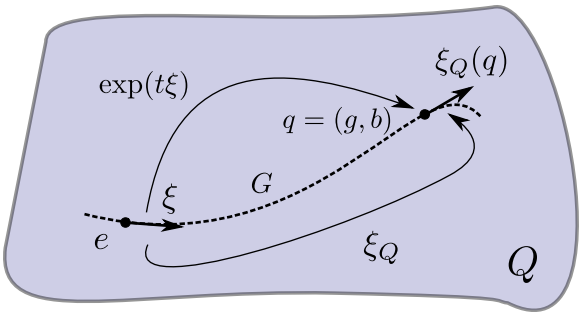

Figure 2-2: The exponential map takes ξ and flows along the fiber G to a group element g. The exponential generator is a velocity at the configuration q.

The vector that appears at the origin of the tangent space at the configuration q tells us how it would change if acted upon by Φ with the group element $\exp t\xi$, the flow due to ξ for t seconds. Because we are taking the derivative at $t = 0$, this gives us an infinitesimal change.

Finally, it is also possible to use the infinitesimal generator to produce a vector field in the Lie algebra. For a given $\xi \in \mathfrak{g}$, we can define a vector field $\xi_{\mathfrak{g}}(\eta)$ at every $\eta \in \mathfrak{g}$, just as we have a vector field $\xi_Q(q)$ at every $q \in Q$. This vector field is denoted $\mathrm{ad}_\xi \eta$. It can be shown that this is equivalent to the Lie bracket operation of ξ and η; *i.e.*, $[\xi, \eta] = \mathrm{ad}_\xi \eta$.

2.1.4 Principal Connections

A principal fiber bundle Q has an associated *principal connection*, a map $\mathcal{A} : T_qQ \to \mathfrak{g}$ that satisfies the following:

1. $\mathcal{A}(\xi_Q(q)) = \xi, \quad \xi \in \mathfrak{g}$

2. $\mathcal{A}(T_q\Phi_g(v_q)) = \mathrm{Ad}_g \mathcal{A}(v_q), \quad g \in G,\ q \in Q,\ v_q \in T_qQ$

The first condition defines $\mathcal{A}$ such that it maps any tangent vector that is an infinitesimal generator of a Lie algebra element ξ back to ξ. The second condition means that transforming a tangent vector via a lifted action in the bundle corresponds to transforming the resultant Lie algebra element by the corresponding Adjoint map Ad_g.

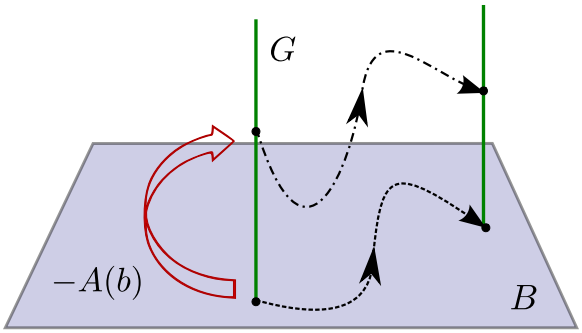

Figure 2-3: The local connection form $-A(b)$ is a base-valued mapping that takes base trajectories to fiber trajectories.

For generic vectors v_q that may or may not be a generator, it is also required that

$$(\mathcal{A}(v_q))_Q(q) = \text{ver } v_q.$$

Therefore, the horizontal space H_qQ is the kernel of the connection mapping, such purely horizontal velocities hor v_q have a zero vertical component [10].

For a trivial fiber bundle, the connection mapping can be written more explicitly with a local form. Recall that a bundle $Q = G \times B$ is trivial if the direct product structure holds globally. In this case, it can be shown [73] that

$$\mathcal{A}(\dot{g}, \dot{b}) = \text{Ad}_g(g^{-1}\dot{g} + A(b)\dot{b}).$$

Note that this equation entails a separation between fiber components g and base components b. The mapping $A(b)$ is known as the *local form* of the principal connection; the fact that it depends only on the base components allows us to study a reduced system.

2.2 Lagrangian Mechanics

Methods from Lagrangian mechanics allow us to perform analysis for mechanical systems in a streamlined way, starting with the quantity known as the *Lagrangian* and then using that to arrive at the equations of motion for the system. However, that

is often as far as the process will go; the resultant equations can be highly nonlinear and difficult to tackle. Previous work in the geometric mechanics of locomotion has sought to reveal common geometric features, such as *symmetries*, to a set of problems in order to simplify these equations and write them in a standard form. We review the standard Lagrangian approach, particularly in the way that it is used with the geometric ideas from the previous section. For further details on the topics of this section, we refer to [1, 10, 73, 89].

2.2.1 Euler-Lagrange Equations

A mechanical system is often described by a set of n *configuration variables* q, which provide a representation for the degrees of freedom. These variables then make up an n-dimensional *configuration space* Q. By studying the features and structures of Q, we can often infer interesting features about the system at hand. An important function is the *Lagrangian*, denoted $L : TQ \to \mathbb{R}$. It is defined as the difference between kinetic and potential energy:

$$L(q, \dot{q}) = \frac{1}{2}\dot{q}^T M(q)\dot{q} - V(q). \tag{2.1}$$

Here, the first term on the right-hand side is the kinetic energy, with the mass matrix $M(q)$ defining a kinetic energy metric on the tangent space, while $V(q)$ is the potential energy.

Once we have a Lagrangian for a mechanical system, it is straightforward to describe how it will evolve in time. The key descriptor is given by the Euler-Lagrange equations of motion, which are generally written as

$$\frac{d}{dt}\left(\frac{\partial}{\partial \dot{q}_i}L(q, \dot{q})\right) - \frac{\partial}{\partial q_i}L(q, \dot{q}) = \tau_i, \quad (i = 1, \ldots, n).$$

There is one equation for each configuration variable. The term τ_i corresponds to external forces acting directly on the ith configuration variable.

It is possible for a mechanical system to be subject to constraint forces. If such

constraints are nonholonomic and there are k of them written in the *Pfaffian form* as $\omega(q)\dot{q} = 0$, then the equations of motion are

$$\frac{d}{dt}\left(\frac{\partial}{\partial \dot{q}_i}L(q,\dot{q})\right) - \frac{\partial}{\partial q_i}L(q,\dot{q}) = \sum_{j=1}^{k}\lambda_j\omega_i^j(q) + \tau_i, \quad (i = 1,\ldots,n).$$

The object $\omega_i^j(q)$ refers to the ith column and jth row of $\omega(q)$. The quantity λ_j is a Lagrange multiplier to be solved with the configuration variables.

2.2.2 Symmetries and Momentum Maps

It is often the case that while a mechanical system may move or change its configuration over time, there are underlying quantities, such as momentum, that remain conserved. These conserved quantities often correspond to *symmetries* that exist in the system itself. If the system's configuration space has a principal fiber bundle structure, *i.e.*, $Q = G \times B$, then the Lagrangian is *invariant* with respect to G (or G-invariant) if

$$L(\Phi_g q, T_q\Phi_g\dot{q}) = L(q,\dot{q}).$$

This relationship determines a symmetry—in other words, the result of the Lagrangian mapping does not change when the system configuration is changed via a group action.

The notion of symmetries is closely related to that of *momentum maps*. Associated with the velocity v_q of a physical system is a momentum, which can be computed by a map $J : T_qQ \to \mathfrak{g}^*$. The space g^* is the dual Lie algebra, whose elements (momenta) are paired with Lie algebra elements (velocities) to produce a real number. This pairing is defined mathematically as

$$\langle J(v_q), \xi\rangle = \langle\langle v_q, \xi_Q(q)\rangle\rangle, \quad \xi \in \mathfrak{g},$$

where the mapping $\langle\langle\cdot,\cdot\rangle\rangle$ is the kinetic energy metric determined from the Lagrangian.

In the above definition of the momentum map, suppose that v_q is an element of the infinitesimal generator of a Lie algebra element η, *i.e.*, $v_q = \eta_Q(q)$. In this case it is possible to relate ξ and η via the *locked inertia tensor*, a mapping $\mathbb{I}(q) : \mathfrak{g} \to \mathfrak{g}^*$ defined as

$$\langle \mathbb{I}\eta, \xi \rangle = \langle \langle \eta_Q(q), \xi_Q(q) \rangle \rangle.$$

As with $J(v_q)$, the object $\mathbb{I}\eta$ lives in the dual Lie algebra, such that the pairing with ξ produces a real number according to the kinetic energy metric of the Lagrangian. The difference is that J acts on a velocity in the group, while $\mathbb{I}$ acts on a velocity in the Lie algebra.

The two mappings are related by a connection form. Recall that a principal fiber bundle has a principal connection $\mathcal{A} : T_qQ \to \mathfrak{g}$. For a system with a defined momentum map and a locked inertia tensor, this mapping can be written as a *mechanical connection* $\mathcal{A}(q, \dot{q}) = \mathbb{I}^{-1}(q)J(q, \dot{q})$. As expected, this relates group velocities v_q to Lie algebra elements η, while specifying that the kinetic energy metric be preserved through the definitions of the momentum map and locked inertia tensor.

2.2.3 Lagrangian Reduction

Having defined how the configuration of a mechanical system may take on geometric structure, we can use that structure to simplify, or reduce, the complexity of the equations of motion. While these equations nominally refer to those derived through the Euler-Lagrange formulation, we will also be able to recast them with the connection form mapping made explicit.

When our Lagrangian is G-invariant, we have a freedom in choosing the coordinates with which to describe the Lagrangian. One choice is to work at the group identity element by using the action $\Phi_{g^{-1}}$ and the corresponding lifted action $T_g\Phi_{g^{-1}}$. We refer to the Lagrangian written in this way as the *reduced Lagrangian*

$$l(b, \xi, \dot{b}) = L(g^{-1}g, b, g^{-1}\dot{g}, \dot{b}) = L(e, b, \xi, \dot{b}).$$

Here, we are explicitly defining ξ as the Lie algebra representation of the velocity $\dot{g}$; ξ is also the transformation of $\dot{g}$ to a frame attached rigidly to the system. For example, in SE(2) ξ can be written as

$$\xi = \begin{pmatrix} \xi_x \\ \xi_y \\ \xi_\theta \end{pmatrix} = T_g \Phi_{g^{-1}} \dot{g} = \begin{pmatrix} \cos\theta & \sin\theta & 0 \\ -\sin\theta & \cos\theta & 0 \\ 0 & 0 & 1 \end{pmatrix} \dot{g}. \tag{2.2}$$

It can be shown [73] that the reduced Lagrangian can be written in the following form:

$$l(b, \xi, \dot{b}) = \frac{1}{2} \begin{pmatrix} \xi^T & \dot{b}^T \end{pmatrix} \begin{pmatrix} I(b) & I(b)A(b) \\ (I(b)A(b))^T & m(b) \end{pmatrix} \begin{pmatrix} \xi \\ \dot{b} \end{pmatrix}.$$

Here, $I(b)$ is a local form of the locked inertia tensor, given by $I(b) = \mathbb{I}(e, b)$; *i.e.*, it is the inertia tensor at the identity of the group, as the reduced Lagrangian is also defined. $A(b)$ is the local form of the mechanical connection.

Using the definition of the momentum map, it can be shown that [10]

$$p = \frac{\partial}{\partial \xi} l(b, \xi, \dot{b})$$

is the local form of the momentum map that corresponds to the kinetic energy metric of the reduced Lagrangian. For unconstrained systems, this is also called the *generalized momentum*.

Because we have assumed that our Lagrangian is symmetric with respect to the fiber variables, the reduced Lagrangian has no dependence on them. By applying the Euler-Lagrange derivation to determine the equations of motion from the above form, we can find the *reconstruction equation*:

$$\xi = -A(b)\dot{b} + I(b)^{-1} p^T. \tag{2.3}$$

The significance of Eq. (2.3) is that the evolution of the fiber variables is first-order and depends only on the base variables and momenta. For a physical system, the

fiber variables usually correspond to an *external* configuration, such as position and orientation with respect to the environment. The base variables then usually describe the physical shape of a system and are thus also known as *shape*, *joint*, or *internal* variables. These may evolve according to their own dynamics, independent of the fibers, or can be directly commanded. The evolution of the momentum terms can be computed separately and often be done independently of the fiber velocities as well.

2.2.4 Kinematic and Dynamic Systems

In general, an unconstrained, n-dimensional system whose Lagrangian is G-invariant can be described by the reconstruction equation. Alternatively, a system governed by a set of k linearly independent Pfaffian constraints written in the form $\omega(q)\dot{q} = 0$ has a reconstruction equation as well, provided that the constraints are also G-invariant. The latter condition requires that

$$\omega(q)\dot{q} = \omega(\Phi_g q)T_q\Phi_g\dot{q},$$

where Φ_g is the group action. This then allows us to rewrite the constraint form ω in a reduced fashion in terms of the base variables only:

$$\omega_\xi(b)\xi + \omega_b(b)\dot{b} = 0. \tag{2.4}$$

These constraints constitute a set of k equations linearly relating the fiber and base velocities.

If the fiber space is l-dimensional, where $l > k$, an additional $l - k$ equations can be found by defining the *generalized nonholonomic momentum*. This restricts the flow of the system along the allowed directions, as specified by the constraints, and is given by

$$p_{\text{nh}} = \frac{\partial}{\partial\xi}l(b, \xi, \dot{b})\Omega^T,$$

where Ω^T is the null space of ω_ξ. It can be shown [89] that these equations can be

rewritten $l - k$ equations of the form

$$p_{\text{nh}}^T = \eta_\xi(b)\xi + \eta_b(b)\dot{b}.$$

These equations have the same form as the constraint equations, and taken with them together they constitute l linearly independent equations as

$$\begin{pmatrix} \mathbf{0} \\ p_{\text{nh}}^T \end{pmatrix} = \begin{pmatrix} \omega_\xi(b) \\ \eta_\xi(b) \end{pmatrix} \xi + \begin{pmatrix} \omega_b(b) \\ \eta_b(b) \end{pmatrix} \dot{b}.$$

They can thus be simultaneously solved to produce the reconstruction equation for a system with nonholonomic constraints.

Systems that evolve according to the full reconstruction equation, in which at least one momentum component of p^T or p_{nh}^T is nonzero, are referred to as *dynamic* systems. The reconstruction equation reflects the fact that such systems are governed by both nonholonomic constraints as well as some form of momentum conservation, which occurs when the former is insufficient to span the fiber degrees of freedom. An unconstrained system may also incur drift with a nonzero and evolving p^T when it is not at rest initially.

Systems with k constraints, where k is equal to the fiber dimension l, will have their motion completely defined by the constraint equations. Since ω_ξ is full rank, its null space and hence the nonholonomic momentum do not exist—the system literally cannot sustain motion without a nonzero base velocity input. These systems are referred to as *principally kinematic* and are governed by a *principal connection*:

$$\xi = -\omega_\xi(b)^{-1}\omega_b(b)\dot{b} = -\mathbb{A}(b)\dot{b}.$$

Example: Kinematic Snake Robot

A standard example of a principally kinematic mechanical system is the three-link robot shown in Fig. 2-4. The configuration of this "kinematic snake" on the plane is fully described by the group element $g = (x, y, \theta)^T \in G = \text{SE}(2)$, representing

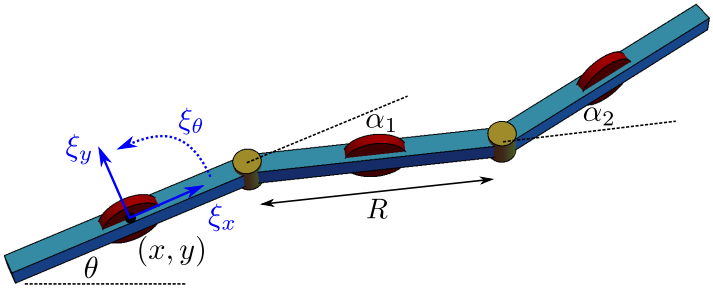

Figure 2-4: The three-link kinematic snake. The coordinates (x, y, θ) describe the inertial position and orientation of the first link, which can also be described in a body-attached frame with velocities $(\xi_x, \xi_y, \xi_\theta)$. The joint angles (α_1, α_2) describe the relative link configurations thereafter.

the system's position and orientation. The relative angles $b = (\alpha_1, \alpha_2)^T \in B = \mathbb{T}^2$ between the links constitute the base variables. The system's full configuration is thus defined by $q \in Q = G \times B$, in which Q is a fiber bundle over B with fiber G.

Now attached to each of the robot's links is a nonholonomically constrained wheel. These provide three constraints of the form

$$-\dot{x}_i \sin\theta_i + \dot{y}_i \cos\theta_i = 0,$$

where $(\dot{x}_i, \dot{y}_i)^T$ is the velocity and θ_i is the orientation of the ith link. The equations can be shown to be G-invariant and can be rewritten into the reduced Pfaffian form of Eq. (2.4), where $\omega_\xi \in \mathbb{R}^{3\times 3}$ and $\omega_b \in \mathbb{R}^{3\times 2}$. Finally, we can define the fiber velocities relative to a frame fixed to the first link as $\xi = (\xi_x, \xi_y, \xi_\theta)^T$, which is related to $\dot{g}$ by the lifted action.

Since we have three constraint equations and the fiber is also of dimension three, the constraints are sufficient to determine a principal connection for the system. The reconstruction equation can be written as

$$\begin{pmatrix} \xi_x \\ \xi_y \\ \xi_\theta \end{pmatrix} = -\underbrace{\frac{1}{D}\begin{pmatrix} \frac{R}{2}(\cos\alpha_1 + \cos(\alpha_1 - \alpha_2)) & \frac{R}{2}(1 + \cos\alpha_1) \\ 0 & 0 \\ \sin\alpha_1 + \sin(\alpha_1 - \alpha_2) & \sin\alpha_1 \end{pmatrix}}_{A(b)} \dot{b}, \tag{2.5}$$

where $D = \sin\alpha_1 + \sin(\alpha_1 - \alpha_2) - \sin\alpha_2$. Note that $\xi_y = 0$, since the wheel on the first link prohibits motion along this direction. Secondly, this equation is valid only if $D \neq 0$, or $\alpha_1 \neq \alpha_2$. Configurations in which the joint angles are equal are *singular configurations*, in which one of the three constraints becomes linearly dependent on the other two. Conventionally, the robot avoids operation near or at these configurations, since they usually entail unbounded constraint forces or the violation of one of the constraints. The compliant variation of this system, which can be designed to avoid these problems, is studied in this thesis.

As opposed to constrained systems, mechanical systems without constraints are governed fully by momentum conservation. In the special case that a system starts from rest, its generalized momentum will be zero and remain zero throughout the system's locomotion. This system is referred to as *purely mechanical*, with the reconstruction equation taking the same linear (in velocities) form as the principally kinematic case, since the momentum term vanishes. Here the local connection is referred to as *mechanical connection* and can be denoted $-A_{\text{mech}}$.

2.3 Tools and Analysis

Systems whose locomotion can be described by the reconstruction equation exhibit a certain structure that can be exploited for motion planning. In particular, if we assume that we have full control over the base variables, then the right side of the reconstruction equation suffices to describe the motion of the entire system. This process can be aided by visualizations of the local connection form through *connection vector fields* and *constrained curvature functions*[1]. Stokes' theorem can also be applied to find approximations for fiber displacement if cyclic base trajectories, or *gaits*, are of interest. The full exposition of these tools can be found in [35, 89].

[1]These were also referred to as *height functions* in previous work

2.3.1 Connection Vector Fields

The reconstruction equation (2.3) prescribes a linear relationship between base velocities $\dot{b}$ and body velocities ξ. This mapping is given by the local connection form $-A(b)$. For kinematic systems, analysis of $A(b)$ is sufficient to describe the full locomotion of the system; for systems with drift, it is still useful to understand how base trajectories are lifted to fiber velocities. From here through the end of the chapter, we assume that we have direct command over all base velocities.

As the local connection acts like a Jacobian, each row corresponds to a fiber component, while each column corresponds to a base component. For example, a system in SE(2) with two joint variables α_1 and α_2 has a 3 by 2 local connection matrix. The rows correspond to the body velocities ξ_x, ξ_y, and ξ_θ, respectively; the columns are the full body velocities in response to unit velocities in $\dot{\alpha}_1$ and $\dot{\alpha}_2$, respectively.

When the base space is two- or three-dimensional, then it is possible to visualize each row of $-A(b)$ as a vector field over B. These *connection vector fields* give us the response in the body velocities for a particular base trajectory. Specifically, a trajectory that generally flows in the same direction of the vectors will generate a positive contribution to the body velocity component, while flowing in the opposite direction will generate a negative contribution. Finally, flowing orthogonal to these vectors will yield trajectories with zero contribution—the kernel of the local connection matrix.

Fig. 2-5 shows the vector fields corresponding to the x and θ rows of the local connection for the kinematic snake, plotted using Eq. (2.5) with $R = 1$. Note that magnitudes are greater near singularity configurations; base trajectories moving along $\alpha_1 \approx \alpha_2$ correspond to "flapping" motions between straightened and 'C' configurations, leading to larger fiber motions. Conversely, moving along the antidiagonal in these configurations corresponds to moving toward 'S' configurations and tend to produce smaller displacement.

In addition to the body velocities, we may also be interested in the system's raw odometry ζ, or the net motion in each body direction, due to its base inputs. This is

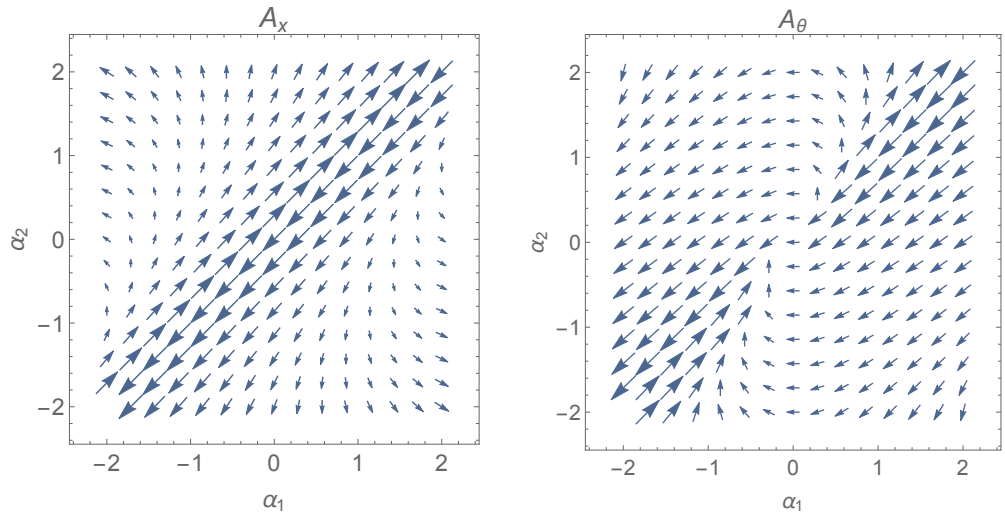

Figure 2-5: The x and θ connection vector fields, corresponding to the first and third rows of the local connection of the kinematic snake.

given by $\int \xi(\tau)\, d\tau$ and can be used to approximate the absolute displacement g under certain conditions. We can then perform a change of coordinates from time to shape to mathematically describe our previous observations about flow direction and body velocities via a line integral of the reconstruction equation on the connection vector fieldsa s

$$\zeta(T) = -\int_0^T A(b(\tau))\dot{b}(\tau)\, d\tau = -\int_\psi A(b)\, db, \tag{2.6}$$

where $\psi : [0, T] \to B$ is the base trajectory.

2.3.2 The Exterior Derivative

In the case that ψ is a closed trajectory, corresponding to a periodic input function, then the line integral along the trajectory can be expressed in another way. According to Stokes' theorem, the line integral of a differential form ω along the boundary of a closed manifold Ω is equal to the integral of the form's *exterior derivative* over the whole of Ω, *i.e.*,

$$\int_{\partial\Omega} w(u)\, du = \int_\Omega dw(u).$$

If we take a closed base trajectory ψ as the boundary of a region β in the base space, then we can rewrite Eq. (2.6) as

$$\zeta(T) = -\int_{\beta} dA(b). \tag{2.7}$$

For a two-dimensional base space, the integral becomes an area integral, and the exterior derivative is the curl of the connection vector fields.

Plots of the exterior derivative of the connection form can significantly aid motion planning and the understanding of the effects of various gaits in the base space. For example, a trajectory may enclose a net nonzero area in the plot corresponding to x, while enclosing a net zero area in y and θ. We can then conclude that such a gait would produce net motion along the system's body x axis only. It is also possible to numerically optimize the net odometry by looking for regions that have maximal or near-zero net area depending on the locomotion goal.

2.3.3 The Connection Curvature

By itself, the exterior derivative only captures the *nonconservativity* of a system, as it is a measurement of displacement in the fibers resulting from a closed trajectory in the base. Another aspect of a system's locomotion capabilities that can be inferred from its connection structure is its *noncommutativity*. For example, computing the raw odometry of a car with drive and steer inputs will result in zero in the direction, say y, perpendicular to the wheels. This is because the nonholonomic constraints prohibit any motion along y. However, this does not sufficiently describe the car's capabilities, as it can perform parallel parking and achieve net displacement in y through a series of maneuvers.

That a control system can achieve motion in a direction not prescribed by the original control vector fields (in this case, the connection form) is due to the noncommutativity of the underlying space. Given two vector fields X and Y, flowing along the directions X, Y, $-X$, and $-Y$ for an equal amount of time each may not necessarily return us to the initial configuration. The resultant displacement between the

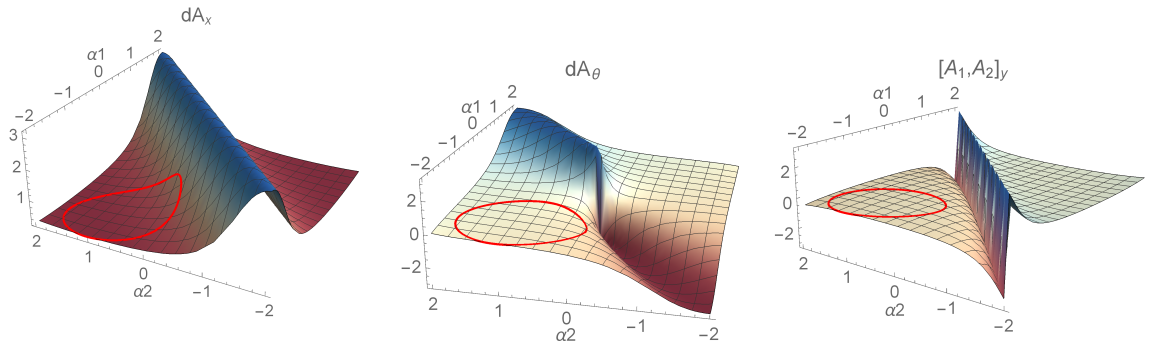

Figure 2-6: The x, θ, and y connection curvature components for the kinematic snake. The first two components are entirely due to the exterior derivative; the last is due to the Lie bracket term.

initial and final configurations for an infinitesimal flow is given by the Lie bracket of the vector fields. If X and Y are defined on an n-dimensional space, the Lie bracket is a vector field defined as

$$[X, Y] = \nabla Y \cdot X - \nabla X \cdot Y.$$

Thus for a two-dimensional base space, the local connection form has two columns $A_1(b)$ and $A_2(b)$, and the noncommutative contribution to displacement in the fiber directions is given by $[A_1, A_2]$. With this in hand we can also define the *curvature* of the connection as

$$-\mathrm{D}A(b) = -\mathrm{d}A(b) + [A_1(b), A_2(b)].$$

Integrating this quantity over a region of the base space provides a more faithful measure of the system's resultant motion relative to the body-fixed frame.

Fig. 2-6 shows the three components of the connection curvature for the kinematic snake, along with an arbitrary gait represented as a closed curve on these plots. Since the base space is two-dimensional, the exterior derivative can be computed as the curl of the vector fields. This is zero for the y component, while the x and θ components have the form shown in the first two subplots. As expected, gaits closer to the singularity configurations yield greater fiber motion, particularly in the body x direction. The Lie bracket, on the other hand, is zero for the x and θ components,

but not for y. This latter plot shows that the "parallel parking" motion can occur for this robot, particularly for gaits that reach close to $\alpha_1 = \alpha_2$.

2.3.4 Planning Gaits

The drawback of the above analysis is that one is often more concerned with raw displacement in the fiber variables with respect to an inertial frame, rather than a body-fixed frame. This is given by

$$g(T) = \int_0^T T_e \Phi_{g(\tau)} \xi(\tau)\, d\tau, \tag{2.8}$$

which may clearly have a dependence on the fiber variables. If the fiber is Abelian, the lifted action loses its dependence on the system's fiber configuration, and the raw odometry is equivalent to the absolute displacement (the Lie bracket terms also vanish, such that the exterior derivative becomes identical to the curvature). Otherwise, we can integrate the connection curvature as an approximation, being most useful for gaits of small amplitude.

For example, the lifted action for SE(2), shown in Eq. (2.2), has an explicit dependence on the fiber variable θ. This captures the discrepancy between the inertial frame and a frame attached to the system's body. For a gait cycle in which θ does not change too much, $T_e\Phi_g$ can be considered nearly constant and can be taken outside the integral in Eq. (2.8). On the other hand, it is possible that $\zeta(T)$ is completely different from $g(T)$ if the gait induces a large rotational displacement. If the system is moving "forward" relative to its own frame while simultaneously rotating, then a portion of its inertial displacement will occur either orthogonal or anti-parallel to the inertial "forward" direction.

Again referring to the connection curvature plots in Fig. 2-6, we have a base trajectory overlaid on each of the components. On the θ plot, the trajectory is located in a region with a very small net area, and indeed over the course of the gait it can be seen that θ does not change very much. The area integral of the region enclosed in the x plot thus provides both a measure of raw odometry as well as an apprxoimation

of absolute forward displacement. It is worth noting we would generally not have to worry about the Lie bracket contribution to the y displacement, as long as we operate away from singular configurations.

It has been shown [82, 35] that the connection curvature $\mathrm{D}A$ is the first term in an expansion that can approximate $g(T)$. This expansion is due to Magnus and provides that the exponential coordinates $z(t)$ for the displacement over a gait ϕ can be approximated as

$$z(t) = \int_{\phi_a} -\mathrm{D}A(b)\, db + \text{higher-order terms},$$

where ϕ_a is the area enclosed by ϕ. $g(T)$ can be computed by exponentiating $z(T)$.

Chapter 3

Beyond the Fiber Bundle Model

The framework summarized in the preceding chapter is powerful, as it allows for a structural separation between a system's internal (base) and external (fiber) degrees of freedom. Many mechanical systems have a configuration space that can be modeled as a principal fiber bundle, including wheeled robots on a homogeneous plane like the kinematic snake, as well as swimming robots in high or low Reynolds fluids. For all of these seemingly disparate systems, we are able to use this common underlying structure to understand how different modes of actuation produce locomotion as well as actively design gaits for movement. Analysis of the principal connection associated with the bundle is especially effective for motion planning as long as the base variables are fully actuated and the fiber variables do not factor into the system's dynamics.

However, the listed categories rigidly limit the scope of applicable systems. It is often the case that even slight physical variations of the examples listed above do not fit into this picture. These include those whose joints are not fully controllable, those with controlled degrees of freedom external to their mechanism, and those whose external configurations do not form a symmetry group. In this chapter we describe how some of the basic assumptions of the fiber bundle model limit analysis of these systems using these geometric tools. In all of these cases, we show that we can either amend or partition the standard bundle with a richer structure. This will turn out be be descriptive for a number of locomoting system classes that do not meet all of the standard assumptions, while each of these classes can be identified based on

the new structure's mapping relationships with the original fiber bundle part of the configuration space.

3.1 Systems with Base Dynamics

Rather than directly commanding the position or velocity of a robot's joint degrees of freedom, it is often the case that there exist non-negligible internal dynamics between the actuator and the joint's actual movement, or perhaps that the joints cannot be controlled at all. These issues may arise because of physical phenomena, such as nonlinear dissipation within the joints, by design when joints are turned off due to power limitations, or unintentionally due to failure during operation.

In the original derivation of the reconstruction equation [74], the evolution of the base variables can be found via the Euler-Lagrange equations. Assuming the existence of a G-invariant connection, we can define a *constrained Lagrangian*

$$l_c(b, \dot{b}, p) = l(b, \xi, \dot{b})|_{\xi = -A\dot{b} + I^{-1}p}.$$

This representation of the Lagrangian reduces the dynamics down to the base and momentum variables only. For kinematic systems, this expresses the fact that the evolution of the base variables is sufficient to recover the overall behavior of the system, since they do not depend on the fibers. If the base degrees of freedom are actuated via G-invariant forces τ, then the base variables evolve according to

$$\frac{d}{dt}\left(\frac{\partial}{\partial \dot{b}_i} l_c(b, \dot{b}, p)\right) - \frac{\partial}{\partial b_i} l_c(b, \dot{b}, p) = \tau_i.$$

It can subsequently be shown [74] that these equations can be rewritten in the form

$$\tilde{M}(b)\ddot{b} + \dot{b}^T \tilde{C}(b)\dot{b} + \tilde{N}(b, p) + \frac{\partial V(b)}{\partial b} = B(b)\tau. \tag{3.1}$$

While the full derivation of each of the terms in Eq. (3.1) has been done, this equation is generally bypassed in the development of the geometric motion planning

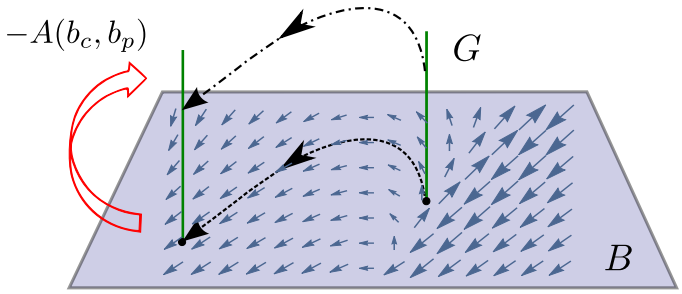

Figure 3-1: A fiber bundle with a subset of its base variables $b_p \in B_p$ evolving according to a set of dynamics rather than being directly commanded.

tools. However, systems for which we do not assume direct control over all base variables will have to incorporate the full base dynamics. For this type of system, we partition the base space as $B = B_c \times B_p$. We thus separately identify directly actuated base degrees of freedom $b_c \in B_c$ from indirectly actuated or unactuated joint variables $b_p \in B_p$.

This partition also distinguishes the notion of the full base space B from the control space B_c. In previous work where these were assumed to be the same, the local connection $-A(b)$ neatly lifted trajectories in B_c to the fibers. For systems in which B_p is not null, the connection is unchanged, but trajectories in B_c are no longer sufficient to determine system motion, since the fibers themselves depend on both b_c and b_p. The b_p variables then evolve according to Eq. (3.1) as vector fields on B, removing our ability to freely dictate their trajectories independently of b_c. This new fiber bundle structure is visualized in Fig. 3-1.

Example: Snake Robot with a Passive Joint

As an example, suppose that we only have direct control of one of the two joints of the three-link nonholonomic snake robot, say α_1. The other joint angle, α_2 is left to evolve passively, following the dynamics of a mass-spring-damper model. Thus, we have $\alpha_1 \in B_c = S^1$ and $\alpha_2 \in B_p = S^1$. Note that the modified system remains kinematic, as the nonholonomic constraints and thus local connection remain unchanged.

We use the Euler-Lagrange equations to derive the dynamics of the passive joint. As with the constraints, the kinetic energy is group-symmetric and does not depend

on the position and orientation of the system (although there is a base dependency in the potential energy). Denoting the inertial position of the passive joint as (x_p, y_p), we can derive the Lagrangian

$$L(b, \xi, \dot{b}) = \frac{1}{2} \sum_{i=1}^{3} \left(M_i(\dot{x}_i^2 + \dot{y}_i^2) + J_i \dot{\theta}_i^2 \right) - \frac{1}{2} k_p \alpha_2^2. \tag{3.2}$$

Here the quantities M_i and J_i are the masses and inertias of the respective links; k_p is the spring constant of the passive joint. We can then define a reduced Lagrangian $l(b, \xi, \dot{b})$ to work in the body frame, followed by a set of reduced Euler-Lagrange equations in the form

$$\begin{aligned} \frac{d}{dt}\left(\frac{\partial l}{\partial \xi_i}\right) &= (\omega_\xi)_i^T \lambda, \\ \frac{d}{dt}\left(\frac{\partial l}{\partial \dot{\alpha}_2}\right) - \frac{\partial l}{\partial \alpha_2} &= (\omega_b)_2^T \lambda - d_p \dot{\alpha}_2. \end{aligned}$$

The object $(\omega_\xi)_i$ refers to the ith column of ω_ξ in Eq. (2.4) (and similarly for ω_b), while the Lagrange multipliers $\lambda \in \mathbb{R}^3$ represent the constraint forces. The constant d_p is a damping coefficient and the term $d_p \dot{\alpha}_2$ is appended to the α_2 equation to capture any damping model component.

The above equations of motion display much more complexity than the reconstruction equation. As noted previously, we can use the latter to eliminate these dynamics' dependence on the fiber velocities ξ, while further manipulation can eliminate the Lagrange multipliers. Doing so will give us the vector fields dictating the evolution of α_2 trajectories in response to α_1 inputs, written generally as

$$\ddot{\alpha}_2 = f(\alpha_2, \dot{\alpha}_2, \alpha_1).$$

This differential equation is represented as a vector field on the base space. These fields (not to be confused with the connection vector fields) restrict the set of base trajectories that can arise given the system parameters and other directly controlled base inputs. We will explore a generalized version of this system and its dynamics in

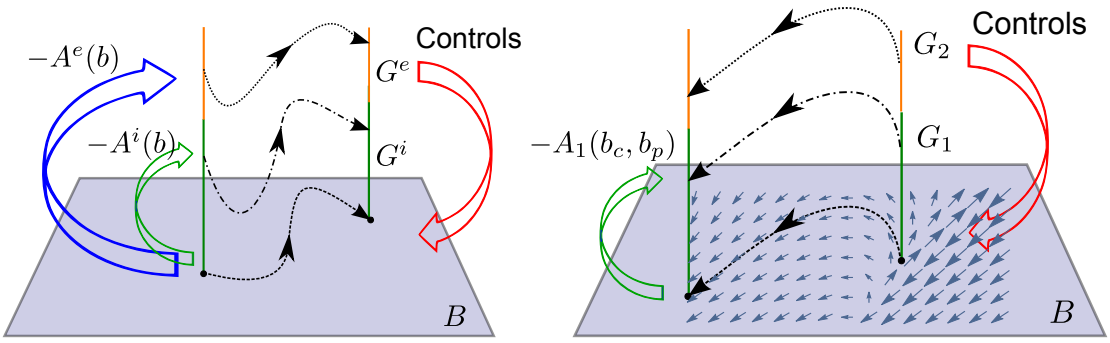

Figure 3-2: Left: A fiber bundle with an internal and an external fiber with controls in the base. Right: Controls in the external fiber determine trajectories in the base.

more detail in the next chapter.

3.2 Systems with External Interactions

The fiber bundle description of a system assumes that *all* of its configuration variables can be neatly categorized into either the base or the fiber. However, this is no longer sufficient when other configuration variables exist, such as the evolution of a non-static ambient medium. In such a scenario, these additional variables will form a third subspace, whose role depends on its interaction with the original fiber bundle and whether system symmetries are still preserved.

3.2.1 Stratified Fiber Bundle

If we consider the example of the three-link snake robot on a moving platform, then the position of that platform would live in a new space. However, just as the *robot's* position (its fibers) do not have any role in determining the overall system's dynamics and energetics[1], the *platform's* position is not important either. Therefore, we can say that the platform's position corresponds to another set of symmetries in the system, and hence makes up a *second* fiber space.

For this type of system, the fiber space takes on a stratified structure $G = G^i \times G^e$.

[1]This is also true for the robot's orientation if the platform's position is prescribed in the robot's body frame; the alternative, being prescribed in the body frame instead, is discussed in the next subsection.

We separately identify fiber variables associated with the configuration of the system $g^i \in G^i$ making up an *internal fiber*, describing the configuration of the robot, from those describing the configuration of the medium $g^e \in G^e$, the *external fiber*. This is visualized in Fig. 3-2(left). Note that the original fiber bundle is unchanged and we retain our original connection $-A^i(b)$. In addition, a second connection $-A^e(b)$ from the robot's base configuration to the medium's configuration can be derived in a manner analogous to $-A^i(b)$.

The structures of the two connections $-A^i(b)$ and $-A^e(b)$ can both be analyzed in the same visual manner using the connection curvature functions. For example, if we care only about the robot's fiber motion in response to certain joint trajectories without regard to how the platform moves, then we need only look at $-A^i(b)$, and the problem is unchanged from before. On the other hand, looking at $-A^e(b)$ tells us how the robot's joint trajectories lead to *motion* of the platform. Finally, a more interesting problem still is that of trying to effect certain fiber motion in both G^i and G^e, which would involve simultaneous search or optimization of base trajectories on both exterior derivative plots.

In this thesis, and in particular for the robot-platform system, we consider both the traditional problem of mapping base trajectories to the external fiber, as well as the reverse problem of having the controls in the external fiber G^e, with the base variables remaining passive. As shown in Fig. 3-2(left), the original splitting between B and G^i allows for analysis to be limited to the response of the base trajectories due to controls in G^e. Once we know our trajectories in B, the original connection $-A^i(b)$ ultimately lifts them to the internal fiber G^i. The problem of relating G^e to B is more difficult as the "inverse" mapping of $-A^e(b)$ may not be well defined. In our work we mainly consider cases in which an inverse can easily be found, and point to some alternative approaches when this is not possible.

3.2.2 Fibers Without Symmetries

In the robot-platform problem, the stratified fiber description and preservation of symmetries hold as long as all quantities are prescribed or expressed relative to the

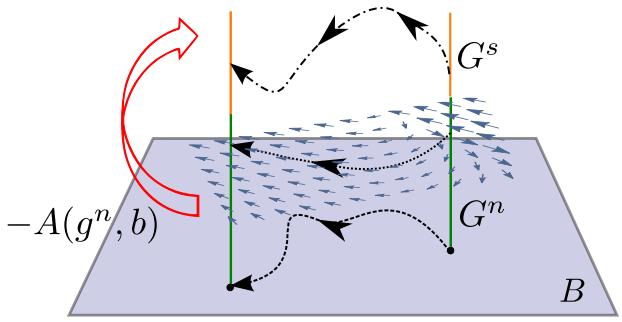

Figure 3-3: Trajectories in the base space determine the dynamics through which the "non-symmetric" fiber components evolve. These base trajectories are then mapped through the connection $-A_s$ to trajectories in G_s.

robot's body-fixed frame. If we do not have this luxury, *e.g.*, the platform inputs are prescribed relative to an inertial frame, then one of the fiber components, the robot's orientation θ, breaks this assumption. This is because θ must be known in order to determine the effect of the robot's and platform's movements on each other.

In general, this situation may also arise even if the ambient medium remains static but contains position-dependent disturbances that act on the system. Alternatively, the medium may facilitate interactions among multiple systems, but these interactions take place in a local manner, for example depending on the relative configurations of two neighboring swimmers.

In all of these cases, the system's dynamics will no longer be symmetric with respect to a subset of the fiber degrees of freedom. However, we may still be able to define a principal bundle on the base variables and the remaining fibers that are symmetric. For example, a falling, reorienting robot is affected by gravity in one fiber direction (or two, if orientation is also considered). A visual representation is shown in Fig. 3-3; like Fig. 3-2 we see the addition of a third subspace, but with two main differences. The first is that no separate connection lifts base trajectories to the non-symmetric fibers; second, the original connection now depends on both base trajectories as well as non-symmetric fiber trajectories.

To facilitate analysis we again consider a partitioning of the fiber space as $G = G^s \times G^n$, such that the system Lagrangian is only symmetric with respect to $g^s \in G^s$

but not $g^n \in G^n$. In other words,

$$L(\Phi_{(g^s,e)}q, T_q\Phi_{(g^s,e)}\dot{q}) = L(q,\dot{q})$$

is true, but not necessarily the broader invariance statement in which the action is due to a general group element Φ_g.

To see how this changes the derivation of the equations of motion, we write the reduced Lagrangian in the following way:

$$l(g^n, b, \xi^s, \dot{g}^n, \dot{b}) = \frac{1}{2}\begin{pmatrix}\xi^s & \begin{pmatrix}\dot{g}^n & \dot{b}\end{pmatrix}\end{pmatrix}\begin{pmatrix} I^s(g^n,b) & I^s(g^n,b)A^s(g^n,b) \\ (I^s(g^n,b)A^s(g^n,b))^T & m_{n,b}(g^n,b)\end{pmatrix}\begin{pmatrix}\xi^s \\ \begin{pmatrix}\dot{g}^n \\ \dot{b}\end{pmatrix}\end{pmatrix}$$

Here ξ^s refers to the velocities of the symmetric fiber variables transformed into a body frame. Conversely, we are not able to transform the velocities $\dot{g}_n$ to a body-fixed representation. While the Lagrangian is fundamentally unaltered from before, the new groupings change the quantities that we use to compute the reconstruction equation. In particular, the new local connection form $A^s : G^n \times B \to \mathfrak{g}^s$ lifts combined trajectories in both the base and the nonsymmetric fibers to trajectories in G^s.

For physical systems, however, it will be the case that the mass matrix of the Lagrangian has explicit dependencies on g^n in addition to b. For example, the kinetic energy of a fluid due to two bodies moving within is determined by the distance between the two bodies. Thus, the components $I^s(g_n, b)$ and $A^s(g_n, b)$ determine the new reconstruction equation as

$$\xi^s = -A^s(g^n,b)\begin{pmatrix}\dot{g}^n \\ \dot{b}\end{pmatrix} + I^s(g^n,b)^{-1}p^T. \tag{3.3}$$

By writing the equation in this way, it is clear that the variables g^n play a similar role as the base variables. The difference, however, is that we do not have control over g^n. Thus, if we define $B^n = G^n \times B$ as an *extended base space*, we return to the

problem in which we have incomplete control over all the base variables. The g^n are in effect *passive* base variables whose dynamics can be analyzed independently of ξ^s in a way analogous to Eq. (3.1). This "extended connection" mapping is depicted in Fig. 3-3.

3.2.3 Example: Snake Robot on a Movable Platform

Our motivating example for the ideas in this section is that of a completely passive three-link robot on a movable platform. The position of the platform, which we denote by (x_p, y_p), is itself a symmetry goup G_p since neither the robot's nor the system's dynamics depends on where the platform is located in space. The configuration manifold is now rewritten as $Q_p = G \times G_p \times B = \mathrm{SE}(2) \times \mathbb{R}^2 \times \mathbb{T}^2$. It is important to note that the connection relationship of Eq. (2.5) still holds, as the nonholonomic constraints are unchanged with the addition of the platform.

This system has a stratified bundle structure. In addition to the original connection between the robot's base variables B and the robot's fiber variables G, a second *mechanical* connection, derived using conservation of momentum rather than the presence of constraints, lifts trajectories from B to G_p, the fiber variables corresponding to the position of the platform. That is, a relationship between the motion of the robot's joints and the motion of the platform can be derived without regard to the robot's x-y location relative to the platform. This relationship can be exploited for motion planning for a completely passive robot, as we show in Chapter 5.

If the platform's position and velocities are written with respect to the robot's body frame, the above description would be sufficient for a motion control problem. Practically speaking, this may not be the case on a real system, for example if the platform's movement were confined to two fixed inertial directions. In such a case, the fiber space of the robot would be split in order to identify the robot's orientation θ as a non-symmetric fiber variable. In other words, $G = G_s \times G_n$, where $g_s = (x, y)$ and $g_n = \theta$. This splitting captures the fact that the robot's interaction with the moving platform depends on its relative orientation but not its relative position. In Chapter 5 we will explore this scenario as well.

3.3 Summary

We have presented an exposition of specific system classes that do not fit into the traditioanl geometric mechanics framework. These include systems with base dynamics, particularly those with passive joints, and systems exhibiting interactions with an external medium. For the first case, we must modify our geometric structure to include dynamics on the base. These dynamics then complement the original connection mapping on the bundle in order to fully determine system behavior.

The second class of systems gives rise to two complexities. The first is the possibility of multiple fibers, representing the configuration of external elements in addition to the fibers of the original system. While the separate fiber spaces may not interact with each other directly, they do so via separate connection mappings from the original base space. A second complexity is the possibility of any of the fiber variables breaking the symmetries of the original system, thus preventing full reduction of the problem as before. While we have described the general modification in the form of Eq. (3.3), specific methods for tackling the problem and extracting useful structure will depend on the example at hand.

Finally, we have briefly described modifications to the original three-link nonholonomic snake robot system to show how it may fit in any of the new problem statements above. These new instances will each be analyzed in detail in the following chapters.

Chapter 4

Systems with Base Dynamics

As we described in the previous chapter, the traditional fiber bundle model assumes full command of all base degrees of freedom. We made a simple modification to the nonholonomic three-link snake robot and showed that a single passive joint can increase the complexity of the locomotion model. While the reconstruction equation remains unchanged, the passive joint's dynamics are highly nonlinear and require further analysis for use in motion planning.

In this chapter we revisit this system, but in the context of a generalized m-link robot. This system shares many locomotion characteristics with a three-link robot, but the main difference is that a robot with four or more links cannot achieve arbitrary configurations in all of its joints without violating at least one nonholonomic constraint. Therefore, we *must* control this system by allowing at most two joints to be actuated. We show that the inputs to the actuated joints completely determine the passive dynamics of this system, contributing to overall locomotion, and show how one may consider gait design to achieve desired motion. This is done within both a kinematic and dynamic context, the former of which assumes two actuated joints and yields a chained form of equations, while the latter allows for the addition of compliance to the joints and assumes only one actuated input. We are also able to model the robot's locomotion when passing through singular configurations, which were previously difficult to handle with traditional kinematic models and full actuation of the robot.

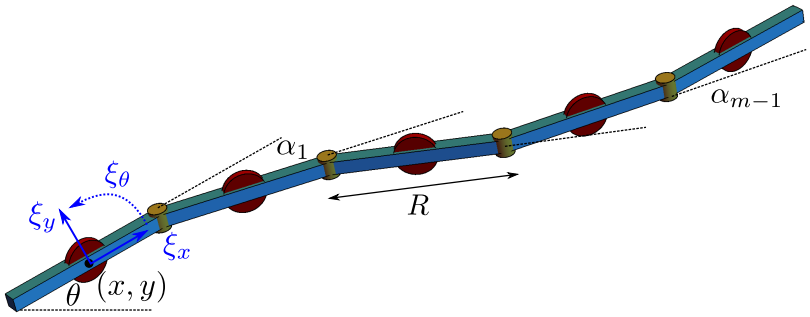

Figure 4-1: An m-link nonholonomic snake robot. The coordinates (x, y, θ) denote the inertial configuration of the proximal link, which also has body velocities $(\xi_x, \xi_y, \xi_\theta)$. Relative joint angles starting from the proximal link are denoted $(\alpha_1, \ldots, \alpha_{m-1})$.

4.1 Kinematic Model

We first consider a kinematic model for the generalized m-link robot. Actuation will be limited to two joints at a time; any more than that will lead to an overconstrained system, as we show below. We describe how singularities and locking behaviors arise due to relative phase relationships among the joints, and then show how the robot is able to execute more natural "slithering" gaits that lead to overall locomotion.

The system shown in Fig. 4-1 is a visual representation of a five-link nonholonomic snake robot. An m-link robot simply has the requisite number of links appended or removed as necessary. Each link has an identical length R and a nonholonomic constraint at the link center. The actuation of the joints and subsequent rotation of the links induce locomotion of the overall system, governed by the velocity constraints.

The robot's configuration is denoted $q \in Q$, where the configuration space Q is a product of two distinct subspaces, $G \times B$. For this system, $g = (x, y, \theta)^T \in G = \mathrm{SE}(2)$ are Lie group variables specifying the position and orientation of the proximal link (identical to the fiber of the three-link robot), and the joint angles $b = (\alpha_1, \ldots, \alpha_{m-1})^T \in B = \mathbb{T}^{m-1}$ describe the links' relative orientations to one another. Links are numbered 1 (proximal) through m (distal) and joints 1 through $m - 1$, with joint i connecting links i and $i + 1$.

The kinematics of the system are described by the set of nonholonomic constraints on the wheels, which prohibit motion perpendicular to each of the links' longitudinal

directions. They can be written as m equations of the form

$$-\dot{x}_i \sin\theta_i + \dot{y}_i \cos\theta_i = 0, \tag{4.1}$$

where $(\dot{x}_i, \dot{y}_i)$ is the velocity and θ_i is the inertial orientation of the ith link. These quantities can be computed recursively in order to express them as functions of q. Starting with the proximal link, we have that $(x_1, y_1, \theta_1) = (x, y, \theta)$; for $i = 2, \ldots, m$,

$$\begin{aligned} \theta_i &= \theta_{i-1} + \alpha_{i-1}, \\ x_i &= x_{i-1} + \frac{R}{2}(\cos\theta_{i-1} + \cos\theta_i), \\ y_i &= y_{i-1} + \frac{R}{2}(\sin\theta_{i-1} + \sin\theta_i). \end{aligned} \tag{4.2}$$

Typically, one assumes that input commands are sent to the joint variables b. For a three-link robot, the number of constraints concides exactly with the dimension of the fiber. By specifying trajectories in both joint (shape) variables, fiber trajectories are then determined exactly by the constraint equations. For a robot with greater than three links, or $m > 3$, each additional joint degree of freedom is added along with a new constraint on the overall system's motion, preventing the system from gaining an additional free controlled input. We can therefore arbitrarily control at most two joint degrees of freedom if all the constraints are to hold.

In this section we consider systems with exactly two input degrees of freedom at any given time, denoted as $b_c = (\alpha_i, \alpha_j)^T$. The rest of the joint variables are denoted b_p and evolve kinematically according to the constraints. The kinematics of the robot can then be rewritten as

$$\begin{aligned} \xi &= -A_c(b)\dot{b}_c, \\ \dot{b}_p &= \quad A_p(b)\dot{b}_c. \end{aligned} \tag{4.3}$$

Here we explicitly separate the mappings from $\dot{b}_c$ to ξ and $\dot{b}_c$ to $\dot{b}_p$; $A_c(b) \in \mathbb{R}^{3\times 2}$ is the local connection form as before, while $A_p(b) \in \mathbb{R}^{(m-3)\times 2}$ is a Jacobian-like relationship

(though not a connection) between the commanded joint velocities $\dot{b}_c$ and the passive ones $\dot{b}_p$. Eq. (4.3) can be further simplified into a chained form as follows.

Proposition 1. *Suppose that* $b_c = (\alpha_i, \alpha_j)^T$ *where* $i < j$. *Then*

$$\dot{\alpha}_k = \begin{cases} f_k(\alpha_k, \alpha_{k+1}, \ldots, \alpha_{j-1}, \alpha_j)\dot{b}_c, & k < i; \\ f_k(\alpha_i, \alpha_{i+1}, \ldots, \alpha_{k-1}, \alpha_k)\dot{b}_c, & k > j; \\ f_k(\alpha_i, \alpha_{i+1}, \ldots, \alpha_{j-1}, \alpha_j)\dot{b}_c, & i < k < j. \end{cases} \tag{4.4}$$

Furthermore, the kinematics of the proximal link can be written as

$$\xi = -A_c(\alpha_1, \alpha_2, \ldots, \alpha_{j-1}, \alpha_j)\dot{b}_c. \tag{4.5}$$

In other words, the kinematics of any joint only depend on the joint configurations between itself and the most distal controlled joint in both directions.

Proof. Due to the recursive nature of how the constraint equations are defined, one can algebraically show that the constraint matrices in Eq. (2.4) for this system have the forms

$$\omega_\xi = \begin{pmatrix} 0 & 1 & 0 \\ -\sin\alpha_1 & \cos\alpha_1 & f(\alpha_1) \\ -\sin(\alpha_1+\alpha_2) & \cos(\alpha_1+\alpha_2) & f_{1,2} \\ \vdots & \vdots & \vdots \\ -\sin\left(\sum_{l=1}^{m-1}\alpha_l\right) & \cos\left(\sum_{l=1}^{m-1}\alpha_l\right) & f_{1,m-1} \end{pmatrix},$$

$$\omega_b = \begin{pmatrix} 0 & 0 & 0 & \cdots & 0 \\ R/2 & 0 & 0 & \cdots & 0 \\ f(\alpha_2) & R/2 & 0 & \cdots & 0 \\ f_{2,3} & f(\alpha_3) & R/2 & \ddots & \vdots \\ \vdots & \vdots & \ddots & \ddots & 0 \\ f_{2,m-1} & f_{3,m-1} & \cdots & f(\alpha_{m-1}) & R/2 \end{pmatrix},$$

where $f_{i,j} = f(\alpha_i, \alpha_{i+1}, \ldots, \alpha_j)$.

The kth row of each matrix, which corresponds to the kth constraint equation, only has dependencies on the joint angles $\alpha_1, \ldots, \alpha_{k-1}$. Furthermore, since all m constraints are independent, the first $j+1$ rows of the matrices yield $j+1$ independent equations. These equations are linear in the body velocities (ξ_x, ξ_y, ξ_θ) as well as the joint velocities ($\dot{\alpha}_1, \ldots, \dot{\alpha}_j$). Given that we have command over the two joints α_i and α_j, this leaves us with $j+1$ unknown velocity quantities (three fibers plus $j-2$ joints), which can be linearly solved.

We now have a solution for the joint velocities $\dot{\alpha}_k$ with $k < j$. The kinematic maps for these solutions have dependencies from α_1 to α_j only, since no equations past the first $j+1$ rows of the constraint matrices are used. This thus proves Eq. (4.5). We can now solve for the joint velocities $k > j$ by successively using each of the constraint equations in order starting from row $j+2$ of the constraint matrices. Each equation has dependencies up to α_k and introduces one unknown joint velocity $\dot{\alpha}_k$, which can be solved since the previous velocities are already known.

We now know that the kinematics must be of the form

$$\dot{\alpha}_k = \begin{cases} f_k(\alpha_1, \ldots, \alpha_j)\dot{b}_c, & k < j; \\ f_k(\alpha_1, \ldots, \alpha_k)\dot{b}_c, & k > j. \end{cases} \tag{4.6}$$

A symmetry argument can be applied. Our choices of the proximal link and the joint α_1 are arbitrarily defined, with the physical kinematics of the system being unchanged if we had instead chosen to start α_1 from the most distal link. Therefore, by defining the constraints relative to that link and going through the same procedure as above,

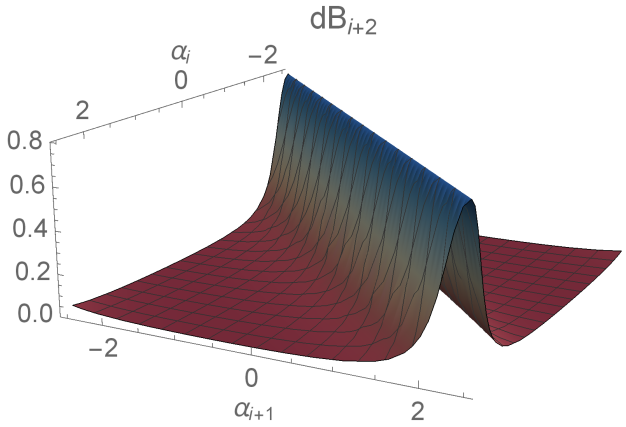

Figure 4-2: The Jacobian exterior derivative of A_{i+2} when α_{i+2} is close to but less than π.

we would obtain (in the original coordinates)

$$\dot{\alpha}_k = \begin{cases} f_k(\alpha_k, \ldots, \alpha_{m-1})\dot{b}_c, & k < i; \\ f_k(\alpha_i, \ldots, \alpha_{m-1})\dot{b}_c, & k > i. \end{cases} \tag{4.7}$$

In order for both Eqs. (4.6) and (4.7) to simultaneously hold, the dependencies must only occur in their intersection. In other words, the function f_k has a dependency on an arbitrary joint α_l only if this is true in both equations. Eq. (4.4) can then be proved by applying this observation to each joint velocity in turn. □

4.1.1 Adjacent Commanded Joints

In considering the overall locomotion of the multi-link snake robot, we first take the case in which the two commanded joints are adjacent to each other, *i.e.*, $b_c = (\alpha_i, \alpha_{i+1})^T$. Since each successive joint's kinematics depend only on that of the joints before it, the evolution of the passive joint variables increases in complexity as they get farther away from α_i or α_{i+1}.

Stationary Passive Joint

Our analysis for a three-link robot helps us understand the types of gaits that would emerge for a robot with more than three links, where the commanded joints are α_i and α_{i+1} and the ones on either side of them are passive. In general, the kinematics of a joint α_{i+2} (or α_{i-1} by symmetry) in response to two adjacent joints α_i and α_{i+1} are given by

$$\begin{aligned}\dot{\alpha}_{i+2} &= \frac{\cos(\frac{1}{2}\alpha_{i+2})}{\sin(\frac{1}{2}(\alpha_i - \alpha_{i+1}))}\left(\frac{\sin(\frac{1}{2}(\alpha_{i+1} - \alpha_{i+2}))}{\cos(\frac{1}{2}\alpha_i)}\dot{\alpha}_i - \frac{\sin(\frac{1}{2}(\alpha_i - 2\alpha_{i+1} + \alpha_{i+2}))}{\cos(\frac{1}{2}\alpha_{i+1})}\dot{\alpha}_{i+1}\right) \\ &\triangleq A_{i+2}\begin{bmatrix}\dot{\alpha}_i \\ \dot{\alpha}_{i+1}\end{bmatrix}. \end{aligned} \tag{4.8}$$

An immediate observation, other than the same singularity of $\alpha_i = \alpha_{i+1}$ of a three-link robot, is that $\alpha_{i+2} = \pm\pi$ are equilibria, as $\dot{\alpha}_{i+2}$ is zero at these configurations. This corresponds to the passive joint rotating all the way around such that link $i+2$ coincides with link $i+1$, normally an undesirable behavior. We must therefore investigate the stability of the equilibrium at π; in order to not remain stationary, $\dot{\alpha}_{i+2}$ should be negative if $\alpha_{i+2} = \pi - \epsilon$ and positive if $\alpha_{i+2} = -\pi + \epsilon$, where ϵ is a small positive number. It can be shown that Eq. (4.8) is simply negated when between the two cases, so any solution that causes one equilibrium to be unstable will also be sufficient for the other.

In the same way that we visualize the exterior derivative of the connection form, we can also visualize the exterior derivative of A_{i+2} of Eq. (4.8). By plotting the magnitude of the curl of A_{i+2}, we can see whether a given combination of α_i and α_{i+1} pushes α_{i+2} toward or away from $\pm\pi$. This is shown as the surface in Fig. 4-2 for $\alpha_{i+2} = \pi - \epsilon$, where ϵ is a small positive number (again, this would be negated for $\alpha_{i+2} = -\pi + \epsilon$). While the absolute magnitudes are not important, it is clearly positive everywhere. Any closed loop that is traversed in a *counterclockwise* direction on the surface will yield a positive net area, pushing α_{i+2} toward π. In order to obtain the opposite result, we must have gaits corresponding to *clockwise* loops, which integrate to negative values and push α_{i+2} away from π. In the α_i-α_{i+1} space, clockwise loops

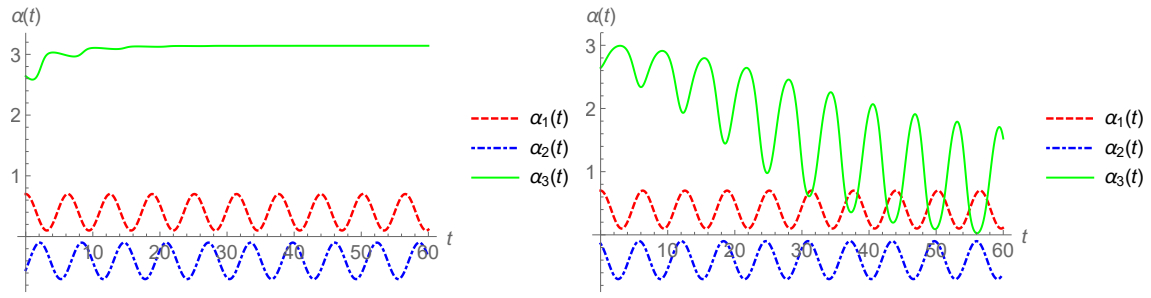

Figure 4-3: Trajectories of commanded inputs α_1 and α_2, and the passive response α_3. The inputs' relative phase determines the convergent behavior of α_3; α_3 moves toward a stationary configuration when α_1 leads α_2, while α_3 oscillates when the opposite is true.

are those in which α_{i+1} *leads* α_i; *i.e.*, their phase difference is between 0 and π.

Fig. 4-3 shows two simulations for a four-link robot verifying our conclusion. The commanded inputs (dashed lines) are $\alpha_1 = 0.3\cos(t)+0.4$ and $\alpha_2 = 0.3\cos(t+\phi)-0.4$, where $\phi = \frac{4\pi}{3}$ in the first simulation, causing α_2 to lag α_1, and $\phi = \frac{\pi}{6}$ in the second, so that α_2 leads α_1. In the former case, the passive response of α_3 (solid line) converges toward π and stays there throughout the trajectory. The opposite is true in the second plot, even though α_3 starts out very close to π and is even initially drawn to it before the end of the first gait cycle.

Oscillating Passive Joints

Assuming that α_i and α_{i+1} are prescribed so that the adjacent passive joint α_{i+2} does not remain stationary, α_{i+2} will have a steady-state oscillatory response. From the second plot of Fig. 4-3, we see that α_3 converges toward a trajectory that is nearly completely out of phase with α_2. This observation holds exactly if α_3 happens to intersect α_2 anywhere along its steady-state trajectory, *i.e.*, $\alpha_3(\tau) = \alpha_2(\tau)$ for some time τ, as Eq. (4.8) reduces to $\dot{\alpha}_3(\tau) = -\dot{\alpha}_2(\tau)$. This means that the two trajectories are out of phase with each other.

Based on simulations and a linearization analysis of Eq. (4.8), we make the following observations about the oscillatory response of α_{i+2} due to sinusoidal inputs with the same frequency but possibly different phase. We assume that ϕ is chosen

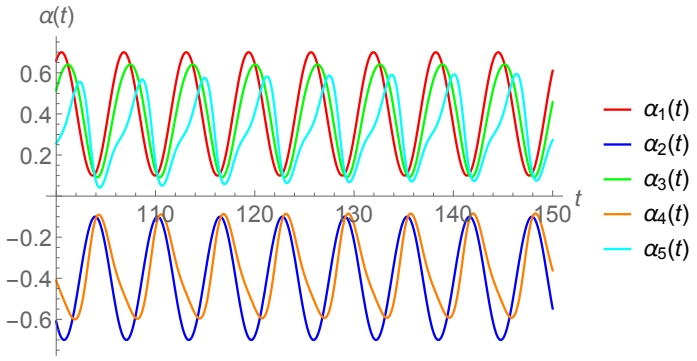

Figure 4-4: Trajectories of commanded inputs α_1 and α_2, and the passive response of joint angles α_3, α_4, and α_5.

so that α_{i+2} does not end up stationary. We also assume that the magnitudes and offsets are such that the α_i and α_{i+1} trajectories do not intersect, ensuring that the robot avoids singular configurations.

1. The magnitude of α_{i+2} depends on ϕ. When the commanded joints are in-phase, α_{i+2} has a magnitude close to the sum of the magnitudes of α_i and α_{i+1} (*i.e.*, they are superimposed). Otherwise, it is about the same magnitude as the smaller of α_i and α_{i+1}.

2. α_{i+2} operates nearly out of phase to α_{i+1}, regardless of the original phase ϕ.

3. The offset of α_{i+2} is closer to that of α_i than α_{i+1}, so that the proximal robot configuration tends toward a "zig-zag" shape.

These observations can be carried over to passive joints beyond α_{i+2}. Although the kinematics of an arbitrary joint α_j become increasingly complex and depend on all of the joints preceding it, the principal response of α_j is to move "opposite" to α_{j-1}. Thus, a natural mode of locomotion is that each successive joint trajectory alternates between the two forms set by the commanded joints, with slight decays in magnitude, phase, and offset going down the links. Fig. 4-4 depicts the trajectories of three passive joints in response to arbitrary inputs to α_1 and α_2. The first passive joint α_3 follows a trajectory close to α_1, while leading α_2 by about the same phase that α_2 leads α_1. The same statements can be made for α_4 and α_5, each relative

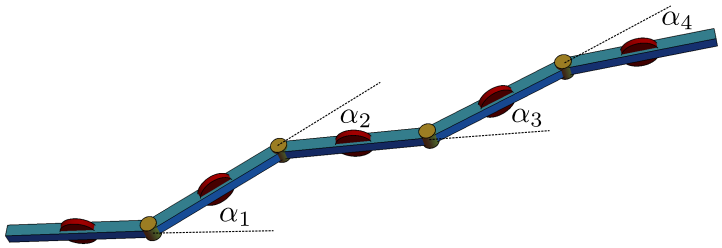

Figure 4-5: Depiction of the natural "zig-zag" configuraiton achieved by the passive joints (α_3 and α_4) of a five-link robot.

to the preceding joints. Note that the magnitudes and sinusoidal form increasingly decay as we move down the chain, since each passive joint does not perfectly replicate the opposite gait of the preceding one. A snapshot of the robot's configuration during these joint trajectories is shown in Fig. 4-5. This dynamic zig-zag shape is maintained throughout the locomotion of the robot.

We can make several statements about the overall locomotion of the robot as a result of different joint interactions. First, because the kinematics are of a chained form, the presence of links and passive joints beyond the standard three-link case does not change the locomotion of the proximal link as long as α_1 and α_2 are the commanded joints. Second, commanding successive joints in the interior of the robot, *i.e.*, joints that are neither α_1 nor α_{m-1}, is to be avoided in order to prevent an adjacent passive joint from becoming stationary. If α_i leads α_{i+1}, α_{i+2} will lock, as per our earlier conclusion; if the opposite is true, α_{i+1} leads α_i and so α_{i-1} will lock. Since it is inevitable that a passive joint on either side of the two controlled ones will become stuck, we can conclude that the two actuated joints must be located at either the proximal or distal end of the robot to avoid any of the joints becoming stationary.

4.1.2 Non-Adjacent Commanded Joints

The analysis of the previous subsection can be extended to situations in which the commanded subset of joints is not adjacently located. Previously, we found that to

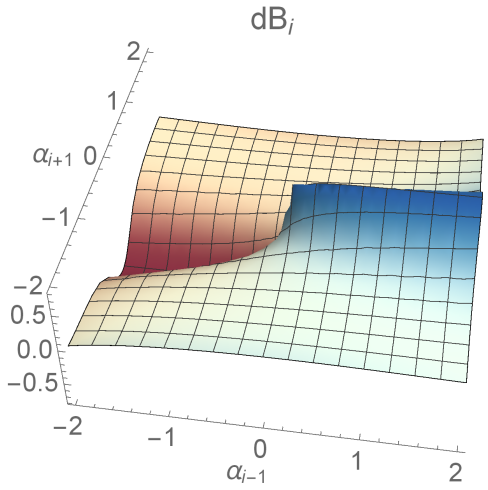

Figure 4-6: The exterior derivative of the Jacobian A_i close to a singularity, for $\alpha_i \approx \frac{1}{2}(\alpha_{i-1} + \alpha_{i+1})$.

avoid joint convergence to stationary configurations, the two adjacent commanded joints must be located at either the front end (α_1, α_2) or the back end (α_{m-1}, α_m), making the robot's fiber locomotion equivalent to that of a three-link robot. In other words, the kinematic model asserts that adding an arbitrary number of passive joints and links to a three-link robot with the original joints actuated does not change how the robot moves. Here we show that non-adjacent commanded joints can potentially avoid becoming stationary and allow for commanded joints away from the ends of the robot. The kinematics of a passive joint α_i between two commanded ones α_{i-1} and α_{i+1} are given by

$$\begin{aligned}\dot{\alpha}_i &= \frac{\cos(\frac{1}{2}\alpha_i)}{\sin(\frac{1}{2}(\alpha_{i-1} - 2\alpha_i + \alpha_{i+1}))}\left(\frac{\sin(\frac{1}{2}(\alpha_i - \alpha_{i+1}))}{\cos(\frac{1}{2}\alpha_{i-1})}\dot{\alpha}_{i-1} + \frac{\sin(\frac{1}{2}(\alpha_i - \alpha_{i-1}))}{\cos(\frac{1}{2}\alpha_{i+1})}\dot{\alpha}_{i+1}\right) \\ &\triangleq A_i \begin{bmatrix}\dot{\alpha}_{i-1} \\ \dot{\alpha}_{i+1}\end{bmatrix}. \end{aligned} \tag{4.9}$$

The form of this equation shares some similarities with Eq. (4.8). However, in addition to again having undesired equilibria at $\alpha_i = \pm\pi$, it is now also possible for the robot to passively find itself in a singular configuration if the sine term in the denominator goes to zero. Note that the singularities here are of a different nature

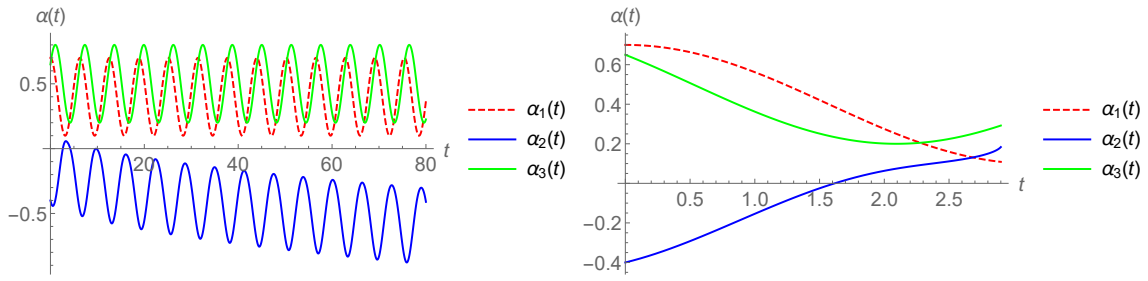

Figure 4-7: Trajectories of commanded inputs α_1 and α_3, and the passive response α_2. The inputs' relative phase determines the convergent behavior of α_2; the left simulation shows α_2 oscillating in a stable manner, whereas the right one has α_2 converging toward a singularity, preventing the simulation from running forward.

from those of Eq. (4.8), which correspond to the two adjacent joints having equal values. In that case, the inputs can directly be chosen to avoid those configurations. Here, in Eq. (4.9) a singular configuration is one in which $\alpha_i = \frac{1}{2}(\alpha_{i-1} + \alpha_{i+1})$, where the critical difference from the previous example is that the left-hand side is a quantity that we do not directly control.

Valid gaits are those that would push α_i away from the average of α_{i-1} and α_{i+1} when it is near the aforementioned value. As before, we can visualize the exterior derivative of the Jacobian A_i of Eq. (4.9), shown in Fig. 4-6 for $\alpha_i = \frac{1}{2}(\alpha_{i-1}+\alpha_{i+1})-\epsilon$, where ϵ is again a small positive number. Since we would like α_i to decrease, we seek a loop that encloses a negative net area. From inspection, we have that a loop lying mostly above the $\alpha_{i-1} = \alpha_{i+1}$ line (upper left side of the plot) should run counterclockwise, and vice-versa for a gait below that line. Unlike in Fig. 4-2, the surface of Fig. 4-6 is not sign-definite; the phasing of the gait is no longer sufficient to determine the sign of the enclosed area, and integration is required to determine the net area for gaits in which the averages of $\alpha_{i-1}(t)$ and $\alpha_{i+1}(t)$ are close in value. A rule of thumb is that the joint trajectory whose average value is smaller (a lower offset) should lead the other.

Fig. 4-7 shows the joint trajectories for a four-link robot, in which α_1 and α_3 are controlled and α_2 is passive. In both simulations, $\alpha_1(t) = 0.3\cos(t) + 0.4$ and $\alpha_3(t) = 0.3\cos(t + \phi) + 0.5$, with $\phi = -\frac{\pi}{3}$ in the first and $\phi = \frac{\pi}{3}$ in the second.

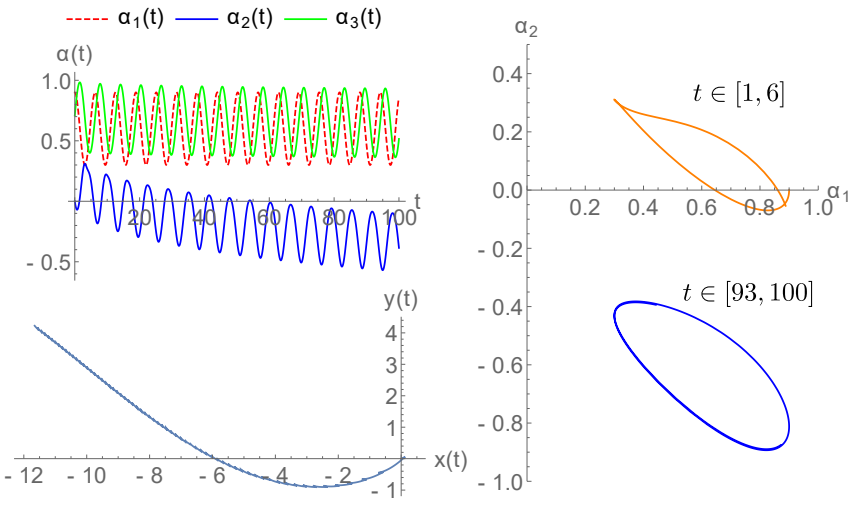

Figure 4-8: Using α_3 to shape α_2 over time (top left) and achieving a desired trajectory in the α_1-α_2 space (right). Bottom left: The robot's fiber motion.

In the first case, the α_1 trajectory, which has a smaller average value, leads α_3, so that α_2 is not attracted into the singular configuration and instead settles into an oscillatory trajectory with an offset opposite the trajectories on either side of it. This is consistent with what we found in Fig. 4-4, in which the roles of α_2 and α_3 are switched but the trajectories remain similar. However, when α_3 is made to lead α_1 in the second plot of Fig. 4-7, we have that α_2 is attracted to the value of $\frac{1}{2}(\alpha_1 + \alpha_3)$ at $t = 2.9$, at which point the kinematic model produces a singularity.

If we have a valid gait trajectory that can avoid singular configurations, the general characterizations of the passive joint behaviors in the previous subsection can be applied here to inform a rudimentary feedback controller for locomotion. For example, suppose that we have a four-link robot in which the two outer joints α_1 and α_3 are commanded and the inner joint α_2 is passive. Since we know that locomotion of the proximal link can be found from α_1 and α_2 only, we can achieve desired α_1 and α_2 trajectories by prescribing α_1 and then "shaping" α_2 using α_3. The qualitative aspects of a shaping controller are as follows.

1. The phase of α_2 is approximately the average of the phases of α_1 and α_3, plus an additional π offset.

2. The offset of α_2 depends on its initial value, but can be changed by shifting the offset or magnitude of α_3 relative to α_1 in the opposite direction.

3. The magnitude of α_2 is determined by its phase with respect to the commanded joints. A larger magnitude can be achieved by scaling α_3 proportionally when the trajectories are close to in-phase.

Given a fixed trajectory α_1 and a desired trajectory for α_2, we can use the above guidelines to impose proportional or more complex feedback controllers on the parameters of α_3. However, these controllers do not necessarily always converge, since the ability to shape the passive joint is rigidly limited by the possibility of hitting singular configurations. For example, the offset of α_2 may not be so close to the other two trajectories that it intersects them, limiting how much control we have over its magnitude. The robustness and convergence of this or an improved controller will be considered in future work.

In the simulation of Fig. 4-8, we have prescribed $\alpha_1(t)$, but we desire $\alpha_2(t)$ to be farther away from the origin with an offset a_d and a phase ϕ_2. We use a feedback controller of the form $\alpha_2(t) = \alpha_1(t - 2\phi_2) + a_3(t)$, where

$$a_3(t) = k_p \left(\frac{1}{2}(\alpha_1(t) - \alpha_2(t)) - a_d \right),$$

where k_p is the controller gain. As can be seen in the top left plot, the effect of the controller is to shrink α_3 (green) in magnitude and shift it downward over time. In response, α_2 (blue) decreases its offset away from α_1 and α_3. The right plot shows a sampling of the trajectories in α_1-α_2 space, where they are mostly elliptical loops starting near the α_1 axis (orange) and then eventually moving downward toward the $\alpha_1 = -\alpha_2$ line (blue). Finally, from the robot's connection curvature plots, we know that these gaits will increase the reorientation of the robot from negative to zero, which is verified by the bottom left plot of the robot's fiber trajectory showing the change in curvature over time. If α_2 is further decreased, then the gaits become closer to the negative regions of $\mathrm{d}A_\theta$, which will cause the robot's trajectory to acquire the opposite curvature.

4.2 Dynamic Model

We have shown that the kinematic model of the m-link robot is derived solely from the constraints, with each passive joint described by a first-order differential equation depending only on the joint angles between it and the commanded ones. Such a model is useful if exactly two joints are commanded. If only one joint is commanded, then a more general dynamic model is required to determine the interactions among all of the passive joints.

In addition, we have also seen that purely kinematic trajectories can be susceptible to joint locking, as well as singular configurations, such that the robot cannot execute arbitrary trajectories following the two prescribed inputs. We will show in this section that a full dynamic model (with only one commanded input) allows the robot to be designed or controlled in a way as to avoid joint locking and singularities.

We assume that each link i has mass M_i^l and moment of inertia J_i, in addition to the identical lengths R. Each joint α_i is represented as a point mass M_i^j, for example capturing motor mass, as well as spring constant k_i, which represents torsional springs on the passive joints; we assume that the resting configurations are all $\alpha_i = 0$. Now the Lagrangian of the whole system can be written as

$$L = \frac{1}{2}\sum_{i=1}^{m}\left(M_i^l((\dot{x}_i^l)^2 + (\dot{y}_i^l)^2) + J_i\dot{\theta}_i^2\right) + \frac{1}{2}\sum_{i=1}^{m-1}\left(M_i^j((\dot{x}_i^j)^2 + (\dot{y}_i^j)^2) - k_i\alpha_i^2\right), \quad (4.10)$$

where (x_i^l, y_i^l) and θ_i are the position and orientation of the ith link defined by Eq. (4.2), and (x_i^j, y_i^j) is the position of the ith joint. If the body velocities ξ are substituted in for the inertial fiber velocities, then the Lagrangian can be reduced to a form

$$l(b, \xi, \dot{b}) = \frac{1}{2}\begin{bmatrix}\xi^T & \dot{b}^T\end{bmatrix}\tilde{M}(b)\begin{bmatrix}\xi \\ \dot{b}\end{bmatrix} - \frac{1}{2}\sum_{i=1}^{m-1} k_i\alpha_i^2, \quad (4.11)$$

where $\tilde{M}(b)$ is a *reduced mass matrix* with dependencies on the system parameters and joint angles only.

The second-order Euler-Lagrange equations of motion can then be derived, giving

us three equations

$$\frac{d}{dt}\left(\frac{\partial l}{\partial \xi_{\{x,y,\theta\}}}\right) = \lambda(t)\omega_{\xi,\{x,y,\theta\}} \tag{4.12}$$

and $m-1$ equations

$$\frac{d}{dt}\left(\frac{\partial l}{\partial \dot{\alpha}_i}\right) - \frac{\partial l}{\partial \alpha_i} = \lambda(t)\omega_{b,i} - d_i\dot{\alpha}_i. \tag{4.13}$$

Here, $\omega_{\xi,\{x,y,\theta\}}$ and $\omega_{b,i}$ are the indicated columns of the constraint matrices in Eq. (2.4), and $\lambda(t) = (\lambda_1(t), \ldots, \lambda_m(t))$ is a horizontal vector of Lagrange multipliers corresponding to each of the constraints. Simple viscous dissipation terms $d_i\dot{\alpha}_i$ can be appended to the latter equations to ensure stability, where d_i are damping constants. Along with the constraint equations themselves, Eqs. (4.12) and (4.13) can be integrated in order to find the dynamic solutions of the robot.

The dynamical equations can be further reduced to the space of the joint variables only if desired. By solving the constraint equations along with Eqs. (4.12) and (4.13) as a linear system in the Lagrange multipliers, we can eliminate the $\lambda(t)$ variables and obtain a system in b only as

$$\tilde{M}_b(b)\ddot{b} + \tilde{C}(b,\dot{b}) + \tilde{K}(b) = 0. \tag{4.14}$$

These equations can then be analyzed for passive joint behaviors in response to commanded ones, without having to worry directly about the constraints or the fiber motion of the robot. Note that the *reduced shape mass matrix* $\tilde{M}_b(b)$ is different from the reduced mass matrix of Eqn. (4.11).

We note here that the dynamics also allow us to consider additional noise such as wheel slip close to singular configurations. If the kinematics are indeed modeled by "soft" rather than "hard" constraints to allow for wheel slip on arbitrary links, then it would be possible to allow for more than three commanded joints. The realization of soft constraints will be considered in future work.

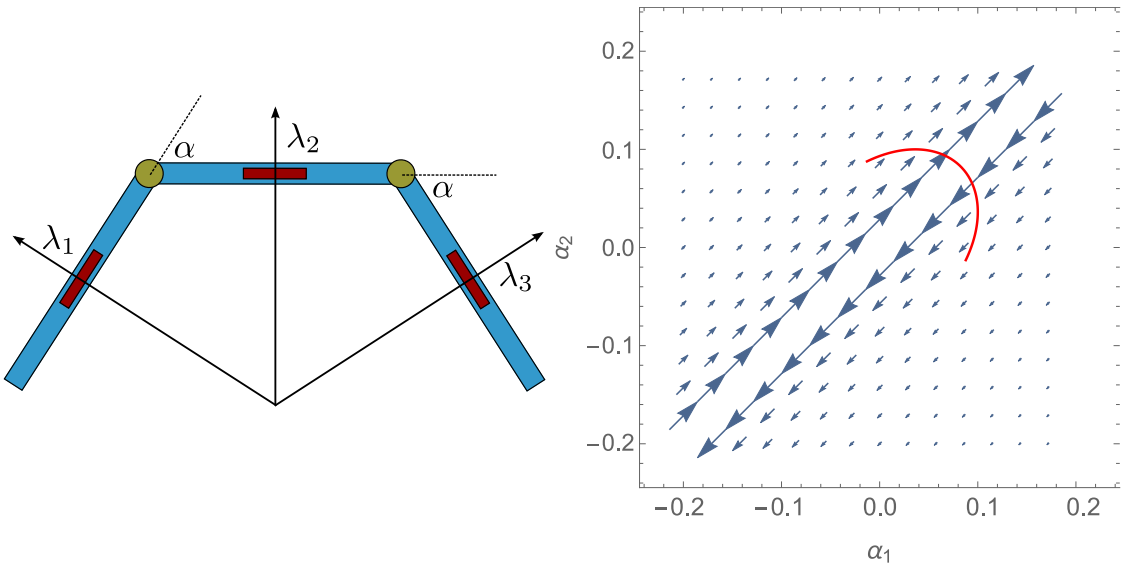

Figure 4-9: Left: The robot in an arc singular configuration, where $\alpha_1 = \alpha_2 = \alpha$. The directions of the three constraint forces $(\lambda_1, \lambda_2, \lambda_3)$ all intersect at a common point, meaning that one is redundant given the other two. Right: A joint trajectory of a three-link robot overlaid on the ξ_x vector field component of the connection. Because the trajectory satisfies $\dot{\alpha}_1 = -\dot{\alpha}_2$, it is able to pass through the $\alpha_1 = \alpha_2$ singular configuration without violating the constraints.

4.2.1 Singular Configurations

In our kinematic analysis of the multi-link robot, we have seen that singular configurations, *i.e.*, those for which the constraints are angled such that at least one is rendered redundant, can be problematic for locomotion since they lead to large constraint forces. For the three-link case, a closer look at the connection from Eq. (2.5) shows that the denominator D goes to zero when $\alpha_1(t_0) = \alpha_2(t_0)$ for some time $t = t_0$. Geometrically, the constraint directions intersect at a common point, as shown in Fig. 4-9(left), because any one of the constraints is redundant given the other two. Substitution of $\alpha_1 = \alpha_2$ into the constraints (Eq. (2.4)) yields a restriction on the velocities such that $\dot{\alpha}_1 = -\dot{\alpha}_2$. If this velocity condition is satisfied, the robot exhibits a hybrid behavior in which it enters a dynamic drifting state at $t = t_0$, followed by a transition back to a kinematic state after $t = t_0$.

Fig. 4-9(right) shows how the above condition appears on the vector field representation of the ξ_x component of the connection (prior to conversion to a scalar

function via the curl of the field). As stated previously, the singularity configurations occur along the line $\alpha_1 = \alpha_2$. In order for the robot to cross these configurations without violating any constraints, its joint velocities must satisfy $\dot{\alpha}_1(t_0) = -\dot{\alpha}_2(t_0)$, an example of which is shown by the trajectory overlaid on the vector plot.

Away from singularities, the line integral of the vector field along the trajectory provides us a measure of displacement along the body frame direction corresponding to the plotted field. For example, if the trajectory in Fig. 4-9(right) were traversed in a clockwise direction, the line integral would increase nearly everywhere along the path, and the robot would acquire a positive displacement in the body's forward direction. At the time t_0 where the path crosses $\alpha_1 = \alpha_2$, the corresponding vector has infinite magnitude. However, because the trajectory is such that $\dot{\alpha}_1(t_0) = -\dot{\alpha}_2(t_0)$, it passes exactly perpendicularly to the vector field direction, allowing the line integral contribution and thus displacement to be identically zero.

Although the line integral approximation of body displacement is still valid with this configuration at the singularities, we can no longer do the full Stokes conversion to an area integral if the trajectory passes through $\alpha_1 = \alpha_2$, even if we ensure that $\dot{\alpha}_1 = -\dot{\alpha}_2$ at those points. This is because any closed trajectory passing through a singular configuration actually encloses two distinct areas, one on either side of the singularity line. Because area integrals over these types of shape space regions can be challenging to compute, we use the vector field line integrals for displacement approximations, but will continue to use the scalar curl functions for visual representation.

With regard to our dynamic model of locomotion, we know that with only one commanded joint input, the solution of Eq. (4.14) for the remaining passive joint also satisfies $\dot{\alpha}_1(t_i) = -\dot{\alpha}_2(t_i)$ if the solution contains singularity configurations at times t_i. Since such gaits are symmetric about the origin of the joint space in the steady state, this allows for forward locomotion of the robot without net rotation, as we have seen from the curvature plots (Fig. 2-6). Fig. 4-10 shows two simulated trajectories of a four-link robot, where $\alpha_1(t) = 0.3\cos(0.5t)$. All parameters are assigned to a value of 1 in both, except the spring constant on the passive joints k_2 and k_3, which are 0 in the first plot. Without stabilizing springs, α_2 is able to drift away from the origin and

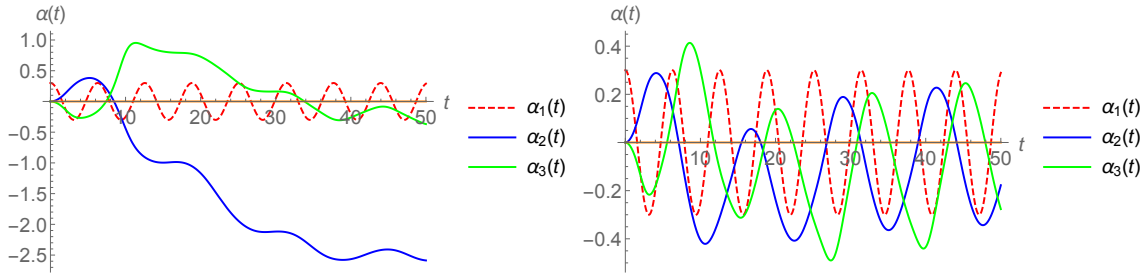

Figure 4-10: Left: α_2 and α_3 are completely passive joints, so that they can drift away from the origin. Right: α_2 and α_3 have stabilizing springs.

would in fact converge toward π if damping were also nonexistent ($d_2 = 0$), a situation detrimental to overall locomotion. In contrast, when $k_2 = 1$ the passive joints have stable oscillatory motions with amplitude and offset roughly equal to those of α_1.

We can use a geometric approach to derive an instantaneous dynamic model describing the robot's behavior while passing through a singular configuration $\alpha_1 = \alpha_2 = \alpha$. Since we lose a constraint, we have one greater fiber degree of freedom than number of governing equations. We therefore derive a momentum quantity to obtain the third equation. Since any velocity that satisfies two of the constraints will satisfy the third, we can take any two of the three rows of ω_ξ from Eq. (2.4), make the aforementioned substitutions, and obtain the reduced constraints

$$\tilde{\omega}_\xi(\alpha)\xi + \tilde{\omega}_\alpha(\alpha)\dot{\alpha} = 0 \tag{4.15}$$

with $\tilde{\omega}_\xi \in \mathbb{R}^{2\times 3}$ and $\tilde{\omega}_\alpha \in \mathbb{R}^{2\times 1}$. Allowed group velocities live in the null space of $\tilde{\omega}_\xi$, which is given by

$$\tilde{\Omega} = \text{span}\big(R\cos\theta, R\sin\theta, 2\tan(\alpha/2)\big). \tag{4.16}$$

We take the generalized momentum derived from the reduced form of the Lagrangian (3.2) as $\frac{\partial l}{\partial \xi}$ and project it onto $\tilde{\Omega}^T$. This gives us an expression for the generalized nonholonomic momentum p, which can be written as a linear combination of group and shape velocity components as

$$p = \eta_\xi(q)\xi + \eta_\alpha(\alpha)\dot{\alpha}, \tag{4.17}$$

where $\eta_g \in \mathbb{R}^{1\times 3}$ and η_α is a scalar function of α only. Stacking Eqs. (4.15) and (4.17) together gives us three independent equations, which can be rearranged in the same way as the original constraints to produce a new reconstruction equation, which takes the form

$$\xi = -A(\alpha)\dot{\alpha} + I(\alpha)^T p. \tag{4.18}$$

The system's locomotion, which is now dynamic rather than kinematic, is thus determined by a combination of actuation in α and momentum in p.

Practically, we know that these dynamics only apply when the system is in a configuration in which the joint angles are equal. If $\dot{\alpha} \neq 0$, the two joint angles will instantaneously move in opposite directions, violating the initial assumption and behaving kinematically once again. We can thus use a simplified model where only $\dot{\alpha} = 0$ is allowed:

$$\xi = I(\alpha)^{-1} p = \frac{(R(1+\cos\alpha), 0, 2\sin\alpha)^T p}{3(mR^2 + 4J + (mR^2 - 4J)\cos\alpha)}. \tag{4.19}$$

In addition, p is conserved ($\dot{p} = 0$) since there are no dissipative forces acting on the system and the system moves as a single rigid body. Eq. (4.19) thus shows that the robot is only able to move dynamically if starting with some nonzero initial momentum p_0 in this regime.

4.2.2 Analysis of Passive Joint Dynamics

Here we look exclusively at the problem of generating particular passive joint trajectories for a single-input multi-link robot, assuming stabilizing springs on the passive joints for stable oscillatory motions. In particular, we are interested in the response of the second joint α_2 (assuming the input is at the first joint α_1), since knowledge of the first two joint trajectories is sufficient to determine overall system locomotion. Assuming periodic inputs, we would like to be able to effect the shape and alignment of the closed gait in the α_1-α_2 joint space, as we know from the connection exterior derivative that the greatest area, and thus displacement, in the body x direction

occurs close to and along the $\alpha_1 = \alpha_2$ axis.

Assuming that we only have sinusoidal inputs, and therefore sinusoidal gaits, this allows us to narrow down our trajectories to only elliptical ones in the joint space. The alignment of such an ellipse, or whether it is wider or narrower along the $\alpha_1 = \alpha_2$ direction, is therefore determined by the magnitude, phase, and offset parameters of the input joint, just as with our observations for the kinematic case.

Joint Harmonics

The first assertion that we conclude is that the trajectory of α_2 tends to track that of α_1, with the exception of a phase offset. In other words, suppose that we command a finite sinusoidal trajectory $\alpha_1 : \mathbb{R}^+ \to B$ for a single-input m-link robot governed by Eq. (4.14), where the remaining joints are all spring-loaded. Then the trajectory of the proximal passive joint α_2 will tend toward a phase-shifted version of α_1, *i.e.*, $\alpha_2(t) \to \alpha_1(t - \phi)$ for some finite ϕ over time. The solution of this robot's nonlinear base dynamics thus produces sinusoidal shape trajectories given that α_1 is also sinusoidal.

For autonomous systems with a two-dimensional shape space, such solutions exist as limit cycles and can be analyzed using the Poincaré-Bendixson theorem, as described by [101, 34, 95]. [13] were able to analytically find limit cycle expressions for the passive orientation response of a two-link robotic swimmer given an input gait at its joint. However, our system cannot be simplified in the same way. An algebraic method that is applicable toward systems such as the multi-link snake robot is the *harmonic balance* method, presented and extended for various systems by authors such as [37, 60, 54]. This can also be seen as an alternative to asymptotic analysis via perturbation expansion, used by [78] to describe the dynamics of a three-link swimmer with a passive joint.

The general idea of harmonic balance, which we will use to show our assertion, is as follows. Instead of analyzing a nonlinear system of differential equations in the time domain, we transform it into a nonlinear system of algebraic equations in the frequency domain. The solution to the original differential equation, assumed to take a sinusoidal form, can be written as a Fourier series, or linear combination of

harmonics, and the coefficients of the harmonics are algebraically solved by *balancing* the corresponding frequency domain component at each harmonic. It may not always be possible to find exact solutions for all the chosen harmonics, particularly since in practice the series representation of the solution is truncated when an infinite series is required. However, the error in the difference is an indicative measure of the goodness of fit.

What we will do here is assume a general sinuosidal input $\alpha_1(t) = A_1 + B_1 \cos(\omega t)$. In the method of harmonic balance, the passive joint $\alpha_2(t)$ then follows a trajectory described by the Fourier series

$$\alpha_2(t) = A_2 + \sum_{k=1}^{N} B_{2,k} \cos(k\omega t) + C_{2,k} \sin(k\omega t). \tag{4.20}$$

Here, the order N of the series is often chosen to replicate the system response as closely as possible. A general system may have an infinite number of harmonics, but from simulations of our robot we observe that only the first harmonic (the same frequency as that of the input) is prevalent. If we choose to expand the series to higher-order harmonics we would find that the corresponding coefficients are orders of magnitude smaller.

We thus choose $N = 1$ and substitute both $\alpha_1(t)$ and $\alpha_2(t)$ and their time derivatives into Eq. (4.14). We then end up with an equation that is a linear combination of harmonics in $\cos(\omega t)$, $\sin(\omega t)$, $\cos(2\omega t)$, $\sin(2\omega t)$, and so on (higher order harmonics appear from products of first-order ones). Each harmonic term yields an individual algebraic equation for the coefficients in front of the harmonics, giving us a system of equations in the unknowns A_2, $B_{2,1}$, and $C_{2,1}$. Once we solve for these unknowns, we find that the solution for A_2 is approximately equal to A_1, while the coefficients $B_{2,1}$ and $C_{2,1}$ determine the magnitude and phase of α_2. Our numerical solutions indeed show that the magnitude $\sqrt{(B_{2,1})^2 + (C_{2,1})^2}$ is approximately B_1. Meanwhile, the offset A_2 generally tracks the input offset A_1.

For robots with more than three links, the observation that the α_2 joint, and indeed each of the remaining passive joints, is simply phase-shifted from the joint

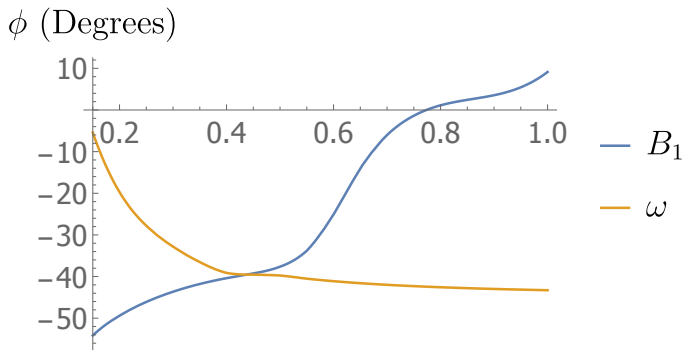

Figure 4-11: An example of the phase of the passive α_2 joint over a sweep of input amplitudes B_1 (where $\alpha_1(t) = B_1 \cos(0.3t)$) and frequencies ω (where $\alpha_1(t) = 0.3\cos(\omega t)$). We note that we specifically chose to show the same numerical domains of the two parameters. These functions are numerically computed using the harmonic balance equations.

prior to it still holds true. In applying the method of harmonic balance, we would have equivalent Fourier series representations, analagous to Eq. (4.20), for each of the passive joints. The number of unknowns, and correspondingly algebraic equations, then increases linearly with the number of additional links.

Joint Phase

In the harmonic balance equations above, the unknown coefficients of the passive response α_2 are solved via nonlinear equations in the known parameters of the input. Specifically, the values $B_{2,1}$ and $C_{2,1}$ change as functions of the input amplitude B_1 and frequency ω, and different value combinations of $B_{2,1}$ and $C_{2,1}$ then determine the resultant phase shift of the trajectory of α_2 from α_1.

While the harmonic balance equations are not very insightful and too lengthy to write out, we can visually show how the phase shift changes as functions of input amplitude and frequency. Fig. 4-11 shows the variation in phase as functions of magnitude and frequency, where the inputs are $\alpha_1(t) = B_1 \cos(0.3t)$ in the former and $\alpha_1(t) = 0.3\cos(\omega t)$ in the latter. We see that in general, phase increases as input magnitude increases or as input frequency decreases.

These results are useful for locomotion when viewed from a geometric perspective.

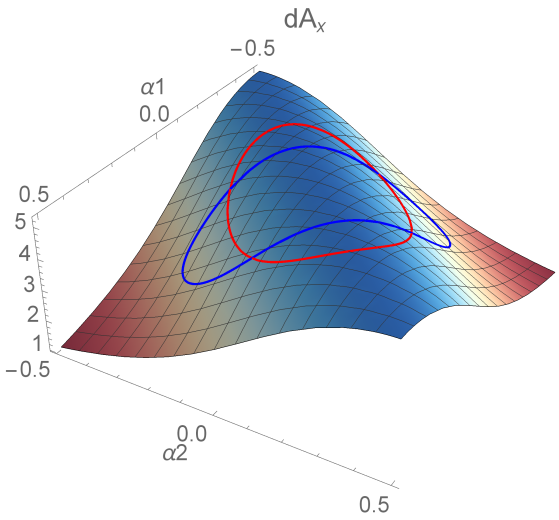

Figure 4-12: Two gaits of a four-link snake robot with a commanded α_1 joint and passive α_2. The gait with a phase of 150 degrees (blue) acquires less displacement per cycle than the one with a phase of 80 degrees (red).

Despite the robot having more than three links and only one commanded joint, the connection equation of Eq. (2.3) and the associated connection curvature plots are still valid descriptions of the robot. In other words, periodic gaits in the α_1-α_2 space overlaid on those plots give us a qualitative measure of the forward and turning displacement that the robot experiences when executing the corresponding α_1 input and experiencing the passive α_2 response. Fig. 4-12 shows two such gaits for a four-link robot, one with a phase of 150 degrees (blue) and the other 80 degrees (red), overlaid on the x component of the connection exterior derivative. For the same input magnitude, the latter is able to acquire significantly more displacement per cycle, as it is more aligned with the α_1-α_2 axis.

4.2.3 Gait Families

With the previous analysis, we know that we can exert some control over the passive joint's amplitude and offset, simply by changing the corresponding parameters of the actuated joint, as well as the relative phase between the two, by finding the right combination of amplitude and frequency in the actuated joint. However, despite the

complexity introduced by all these free parameters, we find that we can easily classify emergent gaits into one of two "gait families"—those that do not cross the singular configuration and those that do. We illustrate these findings with simulations and sample inputs, followed by a more general discussion.

Non-Singular Configuration Gaits

In the first scenario, we command the joint trajectory $\alpha_1(t) = 0.5 + 0.3\cos t$ for a three-link robot. The initial value for α_2 is -0.4 and the passive joint parameters are $k_2 = 1$, $d_2 = 5$. This is an example of a ratio of parameter values that causes the robot to avoid singular configurations. In the steady state, α_2 tends to oscillate about the origin due to the spring restoring force, but not symmetrically. Because d_2 is much higher than k_2, the combination of dissipation and the increasing constraint forces as α_1 and α_2 approach each other is large enough to stop α_2 before α_1 reaches its minimum. At the maximum of α_2, the spring and constraint forces push α_2 back toward the origin, thus giving rise to a periodic gait.

More importantly, this gait leads to nontrivial locomotion in the workspace, and is similar to hand-designed gaits in that it can be represented on the corresponding connection curvature functions, shown as the potato-shaped loop in the plots of the second row of Fig. 4-13. From a design perspective, the relative impedance of the passive joint due to the mass, spring, and damping values determine a tradeoff between gait amplitudes and the location in the joint space. A higher damping value allows for α_1 and α_2 to oscillate nearer each other, placing the gait closer to the high-volume, singular configurations to achieve greater displacement. However, this will also reduce the amplitude of α_2, leading to a narrow elliptical loop that encloses less area than a more circular, equal-amplitude gait would.

Singular Configuration Gaits

Opposite to the case described previously, we now consider system parameters where d_2 is smaller relative to k_2 or initial conditions where α_2 starts off much closer to the α_1 trajectory. An example of both of these changes is shown in Fig. 4-14, where

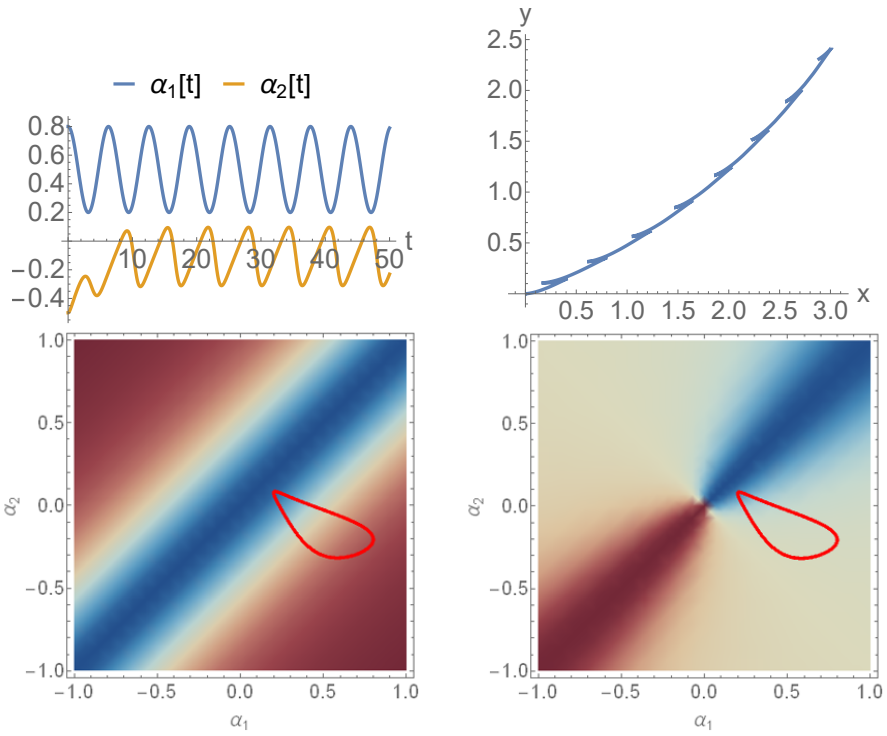

Figure 4-13: Top: The time trajectory of a gait that avoids the singular configuration and the corresponding workspace trajectory of the robot. Bottom: The gait shown in the robot's shape space, overlaid on the x (left) and θ (right) connection curvatures.

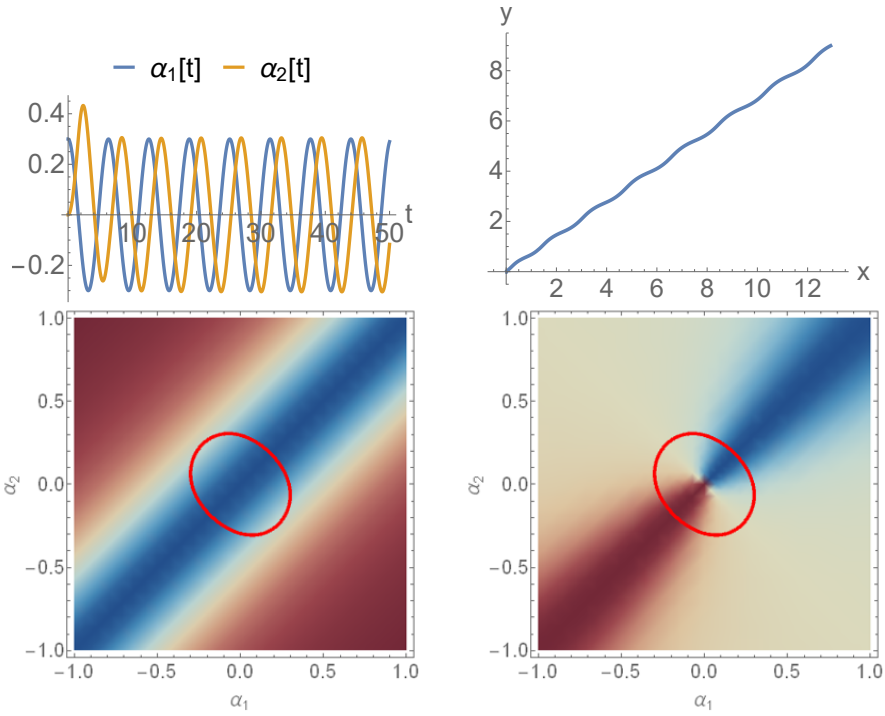

Figure 4-14: Top: The time trajectory of a gait that crosses the singular configuration and the corresponding workspace trajectory of the robot. Bottom: The gait shown in the robot's shape space, overlaid on the x (left) and θ (right) connection curvatures.

$\alpha_1(t) = 0.3\cos t$, and $k_2 = d_2 = 2$. Because α_2 lags α_1 in the steady state, the passive joint is in an asymptotically stable region of the phase space at almost all times, allowing it to track α_1). Note that α_1 and α_2 are allowed to periodically cross each other. Such a gait would have been very unintuitive to design even for a fully actuated system, as this single flow is the only trajectory that passes through without the constraint forces becoming unbounded.

The fact that the resultant gait tracks so close to the singular configuration is desirable from a locomotive efficiency standpoint. We overlay this gait on the x connection curvature function as the red loop in Fig. 4-14 and see that much of it encircles a high volume region (blue). This corresponds to a much larger forward displacement compared to the previous emergent gait or any hand-designed gaits that are restricted to half of the joint space to avoid the singularities. Directly comparing Figs. 4-13 and 4-14 shows that for an input of equal amplitude in α_1, the latter is able to locomote about four times more in absolute displacement. Furthermore,

because this particular gait is symmetric about the $\alpha_1 = -\alpha_2$ axis, it encloses minimal net volume on the θ connection curvature function. This then leads to minimal net rotation over the course of the gait, allowing the system to effectively move in a straight line as shown in Fig. 4-14. This could be useful if movement only in a certain direction is desired, for example.

The previous two gaits are representative of most types of gaits that can emerge from this active-passive joint system. If we selectively vary initial conditions and system parameters, we see that emergent gaits typically belong to one of two "families." Shown in Fig. 4-15, these gaits are either irregularly shaped non-singular loops or narrow (meaning that the joints are out of phase) singular loops. While all of these gaits provide different efficiencies for forward motion or reorientation, this is a qualitative representation of the effect of the passive joint dynamics.

4.2.4 Feedback Control

In addition to changing the passive joints' phase offset, the balance equations also show that those joints' magnitude and offset generally follow those of the commanded joint. This is sufficient for achieving arbitrary fiber motions on the plane, since we can use the kinematic model of geometric phase to approximate gaits that will mainly move the robot forward in the same body direction (centered about the origin), or those that turn the robot in a specific direction (offsetting the gait away from the origin). Feedback controllers, as described for the kinematic model, can then be imposed on the magnitude and offset of the input α_1 in order to achieve the same desired values for the passive joints. The net effect is to shift and shape the trajectory along the $\alpha_1 = \alpha_2$ line in the first two dimensions of the joint space in order to achieve a desired displacement and reorientation per cycle.

Fig. 4-16 shows an example of this controller applied to a four-link robot. The joint trajectories initially start centered around 0.2 radians, with a magnitude about the same. These are the loops centered around the first quadrant of the joint space plot (bottom left). The input frequency was chosen such that the resulting phase is about a third of a gait cycle. According to the θ connection curvature plot, the

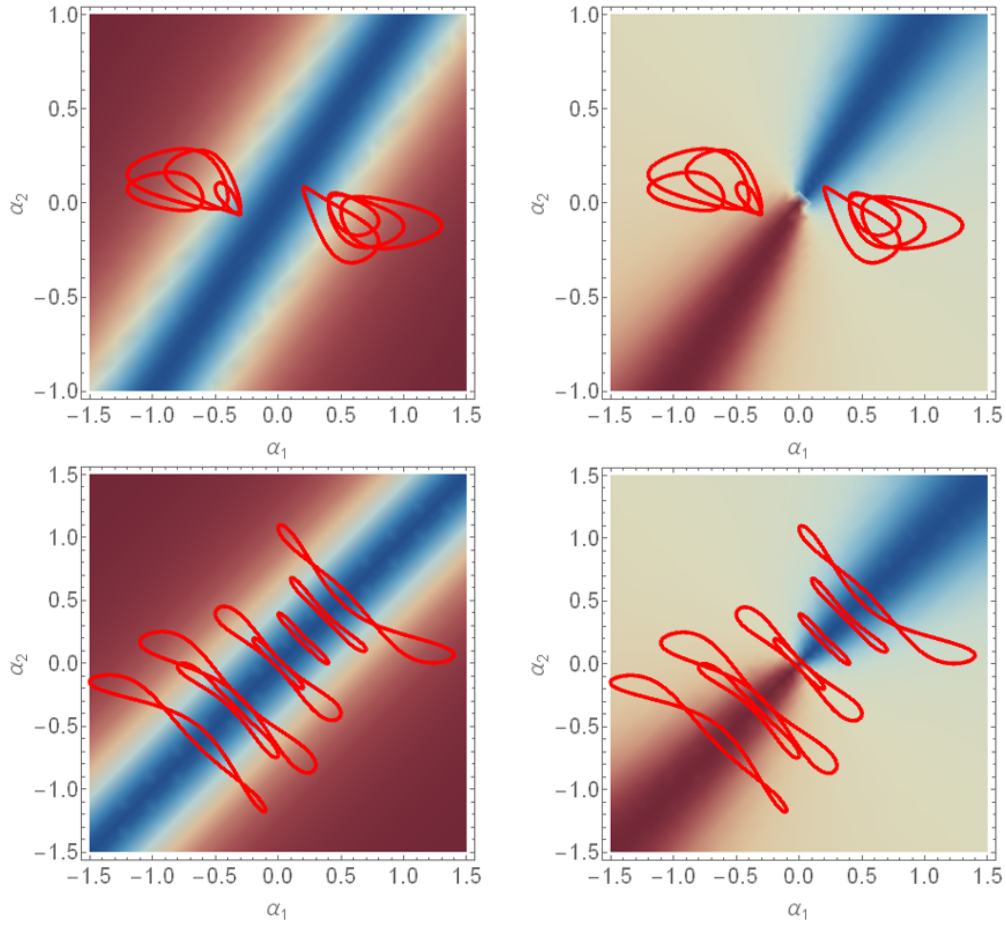

Figure 4-15: Two gait families that emerge in the active-passive three-link robot. The top row corresponds to less efficient gaits that avoid the singular configuration. The bottom row exhibits gaits that do cross the singular configuration, but efficiency is largely determined by the shape or phase of the gait itself.

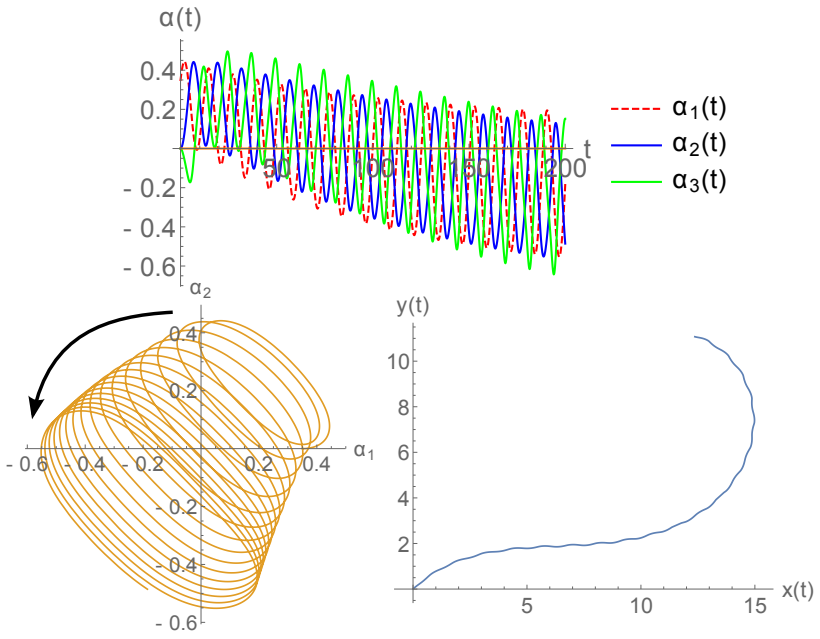

Figure 4-16: Top: Feedback-controlled trajectory of α_1 and passive responses of α_2 and α_3. Bottom left: The trajectory in α_1-α_2 space, shifting from first quadrant to the third quadrant. Bottom right: The robot's fiber trajectory, changing from a path of small negative curvature to one of larger, positive curvature.

robot follows a trajectory of slightly negative curvature and with a small forward displacement per gait cycle (bottom right). It is then desired for the robot to start turning more sharply in the opposite direction—this corresponds to shifting the gait downward to the third quadrant in α_1-α_2 space and increasing its magnitude. As shown in the top plot, this is achieved by increasing the magnitude and decreasing the offset of α_1 over time, causing both α_2 and α_3 to follow.

This controller design can be applied to robots with an arbitrary number of links. The passive joint trajectories will change since the presence of additional joints down the line couple into their dynamics. However, the commanded joint can still use feedback to shape the adjacent joint, followed by the remaining ones down the chain, with each successive one down the chain following its predecessor.

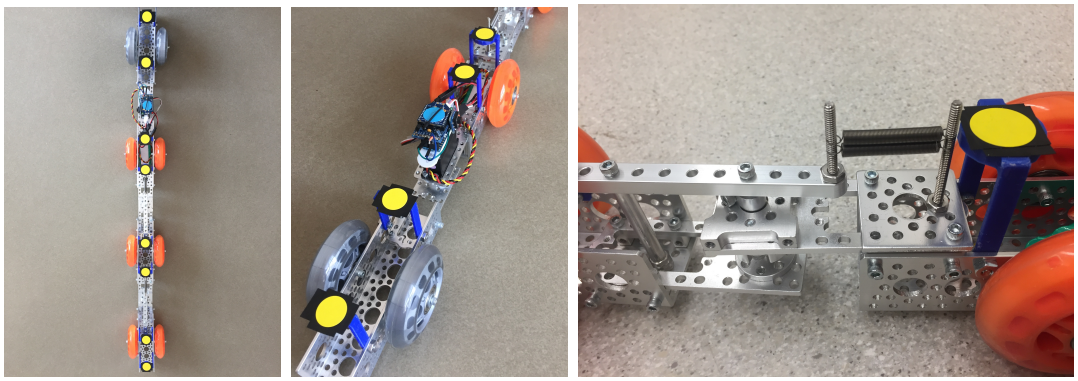

Figure 4-17: Left: Top view of an experimental four-link robot, actuated by one joint with a servo motor and the rest passively compliant. Middle: Closeup of the first two links and servo joint. Right: Detail of the linear spring implementation between the passive joints of the robot. The effective stiffness can vary in the number of springs.

4.3 Experimental Results

To verify some of our theoretical observations and analyses, experimental apparatuses resembling the three- and four-link nonholonomic snake robot models are used to qualitatively assess gait, joint-angle, and workspace trajectories. To facilitate easy development of different and modular configurations, we use prefabricated parts from Actobotics as the primary source of components for the robot. A physical realization of a four-link robot with a single commanded input joint and passively compliant joints is shown in Fig. 4-17(left and middle).

We use skate wheels made of polyurethane with standard ball bearings to realize the single wheel shown in the model. Note that while each link contains two wheels instead of one, the nonholonomic constraint on a single wheel is identical to those acting on the two wheels on each link in the experiments. Linear springs are used to model passive compliance. By attaching one end of the spring to a lever arm extended over a joint and the other end to the neighboring link, the spring can undergo linear deflections. The lever arm thus experiences a force similar to that of a torsional spring. An example of the configuration of each spring is shown in Fig. 4-17(right).

The modular nature of our system easily allows for the robot to contain an arbitrary number of links, from three to four or more. Each link is about 6 inches long and

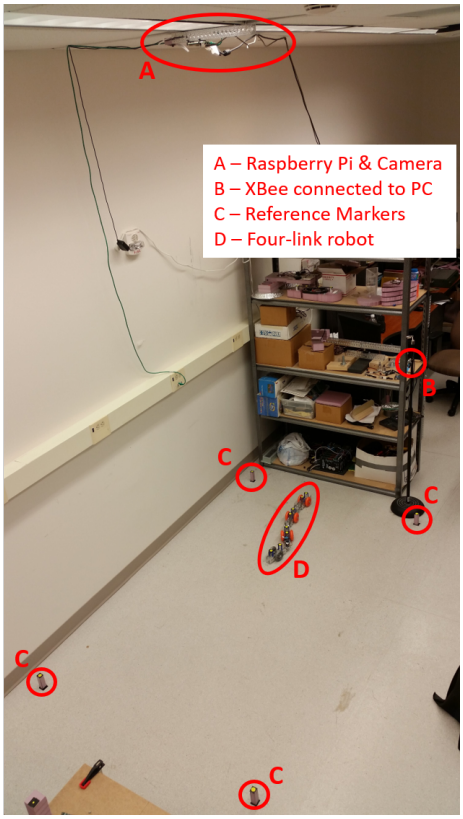

Figure 4-18: The experimental setup with camera and markers, along with the four-link robot in the workspace.

connects to neighboring links using identical parts for consistency and symmetry. The total lengths of the three- and four-link robots are about 24 inches and 33.5 inches, respectively. At the proximal input joint, the robot is equipped with an Adafruit Pro Trinket to control a servo motor. Communications and power are handled via an XBee Series 1 wireless communication module and a 6 V, 350 mAh NiMH battery.

Tracking of the robot is done via the position and orientation of each individual robot link, atop which is affixed two yellow markers equidistant from the center of the link. These markers' trajectories are tracked relative to the laboratory frame, which is defined also by four yellow markers placed at the corners of the general workspace area.

We capture video using a Raspberry Pi and Pi camera and postprocess these videos using MATLAB, in which the positions of each marker is identified and recorded on a frame-by-frame basis. These positions determine the centroid and thus position of

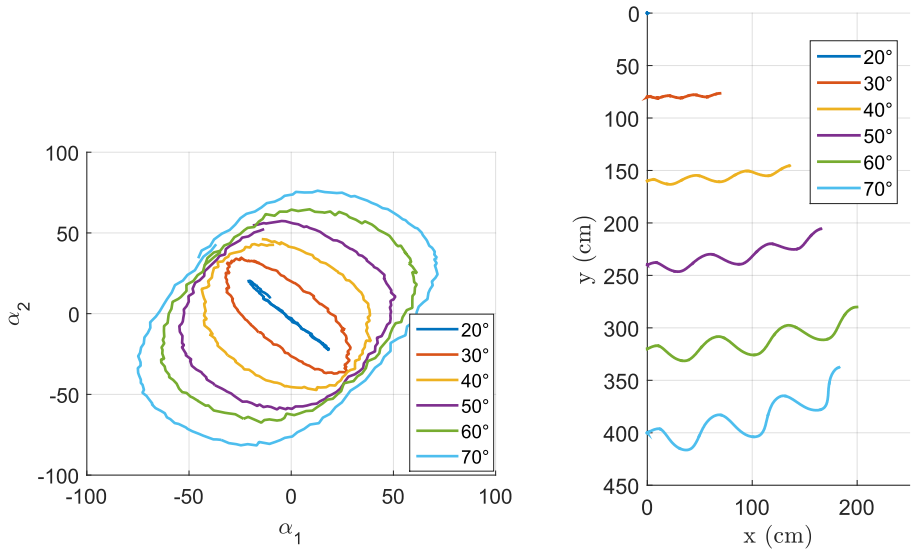

Figure 4-19: Shape space (top) and workspace (bottom) trajectories of a 3-link robot undergoing an amplitude sweep ranging from 20 degrees to 70 degrees for the commanded α_1 joint at frequency 0.3 Hz.

each link relative to the laboratory frame. Link orientations are determined using relative measurements between neighboring links. In all experiments, the orientation and trajectory of the robot relative to the laboratory frame is computed using the second link. The Raspberry Pi and Pi camera are mounted 10 feet above the workspace providing an effective area approximately 6 feet wide and 10 feet long. Fig. 4-18 shows a perspective of the workspace and the previously described components, along with the four-link robot in the space.

4.3.1 Parameter Sweeps

Recall that we observed that the relative phase of the robot's first two joint trajectories generally varies with both the amplitude and the frequency of the sinusoidal input. We perform sweeps in both parameters to show that the experimental robot exhibits qualitatively similar behavior. From our geometric understanding of the system, we also know that the relative phase directly affects locomotive efficiency, measured by displacement per gait cycle per amplitude. This relationship can be visually understood by the alignment of the closed loop in α_1-α_2 space.

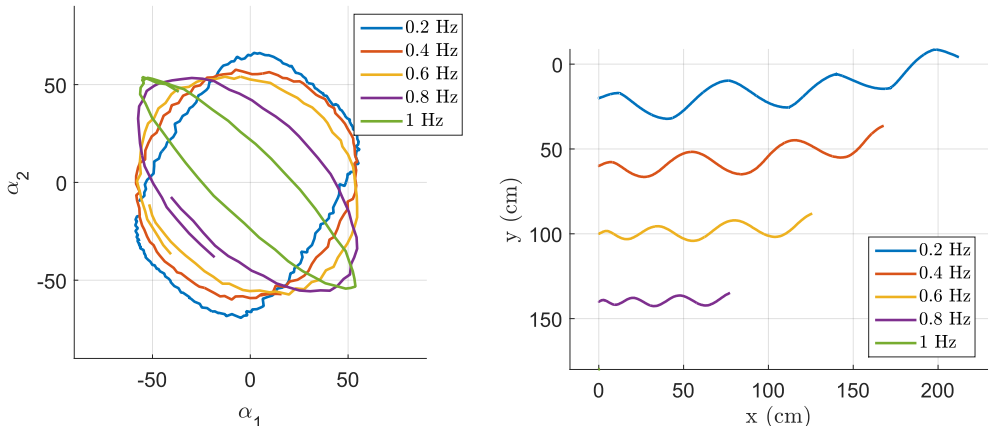

Figure 4-20: Shape space (top) and workspace (bottom) trajectories of a 3-link robot undergoing a frequency sweep ranging from 0.2 Hz to 1 Hz for the commanded α_1 joint at amplitude 55 degrees.

Fig. 4-19 shows an amplitude sweep for a three-link robot, where the amplitude of the input trajectory varies from 20 to 70 degrees while the frequency is kept constant at 0.3 Hz. As expected, the phase depiction of the gaits in the shape space shows the ellipses moving from alignment with the $-\alpha_1$-α_2 diagonal to alignment with the α_1-α_2 diagonal. Such a transition in the gait phase, as well as the fact that the subsequent experiments have a higher magnitude per gait cycle, results in the robot obtaining a higher displacement per cycle in the latter experiments. The workspace trajectories are shown side by side in the second plot of Fig. 4-19; they are placed at regular intervals along the y axis and reoriented such that the second link is aligned with the laboratory x axis. Note that at 70 degrees the workspace trajectory actually starts to turn away from its original heading. This is not surprising as large swings of the robot's links are prone to incur unmodeled effects such as slipping and resistance against neighboring links.

Similarly, Fig. 4-20 depicts a frequency sweep, where the frequency of the input varies from 0.2 to 1 Hz while the amplitude is kept constant at 55 degrees. As frequency increases, the shape space depiction of the gait becomes more anti-aligned with the positive α_1-α_2 diagonal. Since amplitude remains the same in each instance (*i.e.*, the path length of the shape space representation remains almost constant),

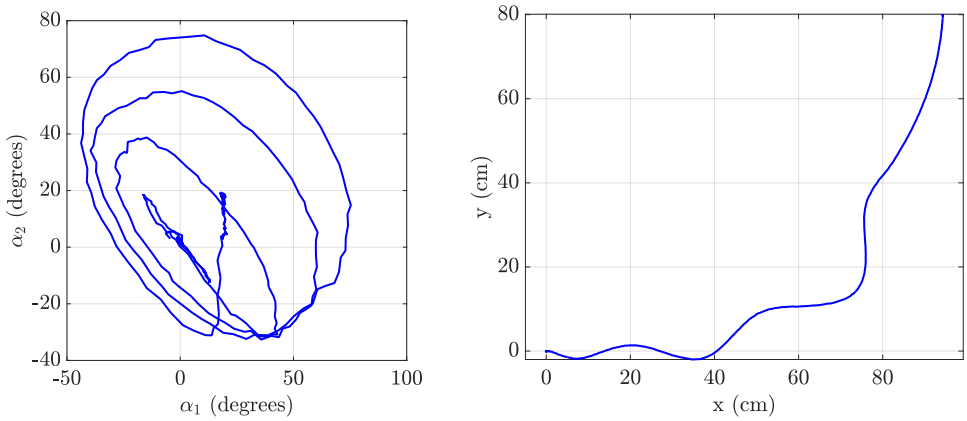

Figure 4-21: Shape space (top) and workspace (bottom) trajectories of a 4-link robot continuously varying its input offset parameter. When the commanded joint α_1 acquires an offset, the compliant joint α_2 is offset as well, resulting in a workspace trajectory with nonzero curvature.

we can fairly compare the effect of the relative gait phase on overall displacement, and we see that anti-alignment produces markedly less displacement per cycle than alignment with the α_1-α_2 diagonal. Note that at 1 Hz, the robot fails to generate any appreciable locomotion, hence the lack of a trajectory corresponding to that frequency in the second plot.

In the previous experiments, the offset of the sinusoidal input is zero, resulting in a mostly straight workspace trajectory aligned with the robot's initial heading. As we recall from the equation corresponding to the θ component of the robot's body velocity, as well as the corresponding connection curvature plot, a nonzero offset will introuce a nonzero curvature to the robot's trajectory. Fig. 4-21 shows that by introducing an offset into the input, the passive joint will track this offset as well. The offset of the commaned joint α_1 is continuously increased from the beginning of the experiment, resulting in the workspace trajectory having an increasing curvature.

4.3.2 Navigation

It is possible to use our knowledge about the dependence of workspace displacement and trajectory curvature on the robot's input parameters to conduct navigation of

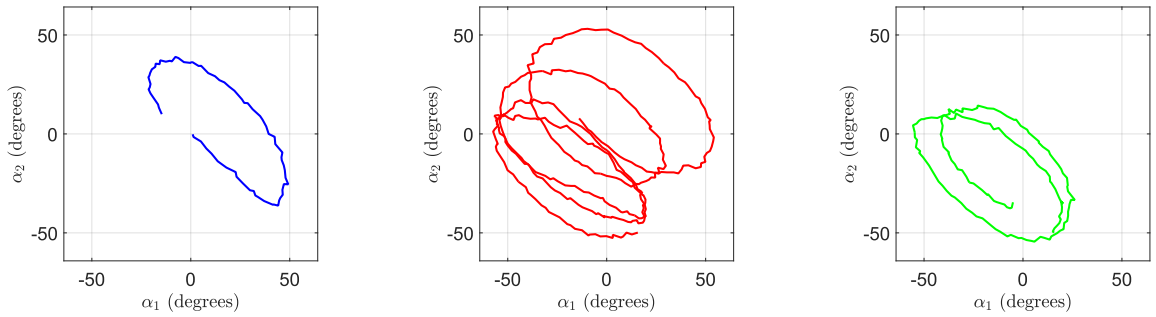

Figure 4-22: Three shape-space segments of a full trajectory of a 4-link robot modulating the offset of its input joint α_1. Starting at the origin, the robot has a positive offset, leading to initial orientation to its left. The second segment is a transition to a negative offset in order to zero out out the workspace curvature. The last segment smoothly increases the offset back to zero.

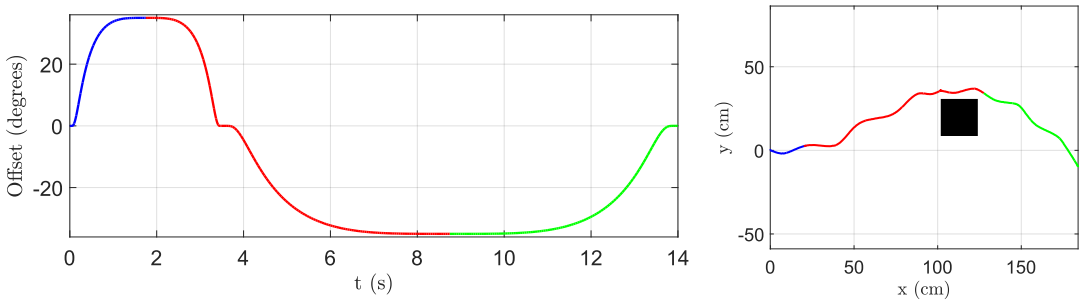

Figure 4-23: Left: Value of the input joint's offset over time, colored into three different segments corresponding to the gait segments in the shape spaces above. Right: Resultant workspace trajectory of the 4-link robot navigating around an obstacle.

the environment. For greater displacement per cycle, the robot commands the input joint to either increase amplitude or decrease frequency until the desired velocity is achieved. To turn around, the input must acquire a nonzero offset, with the sign of the offset determing the turn direction. For this experiment we introduce an obstacle along the robot's unmodified trajectory and precompute suitable trajectory segments that would allow the robot to navigate around it. These segments are then stitched together via smoothing functions to obtain a continuous input command. The resulting shape space depiction of α_1 and α_2, as well as the trajectory taken by the robot, are shown in Figs. 4-22 and 4-23.

4.4 Summary

In this chapter, we looked at a generalized m-link nonholonomic snake robot as an example of a system with passive base dynamics. From the kinematic model of the robot, we showed that such a system, with more than three links, in general must have passive joints in order for all the constraints to hold. However, we were also able to show that the joint kinematics take on a chained form, allowing us to determine gaits with two adjacent or non-adjacent joints that can avoid locked and singular configurations. We also characterized oscillatory modes for the passive joints that qualitatively inform a class of feedback controllers.

The dynamic model, though more complex, allowed for elements such as stabilizing torsional springs and locomotion of the robot by actuating only one joint. The method of harmonic balance provided an approximate solution to the robot's dynamics that allowed us to characterize the phase response of the passive joints, which were then connected to geometric phase analysis in order to describe the robot's motion. In particular, we showed that gaits tended to belong to a particular gait family, which was helpful for easily determining feedback controllers for desired motions. Finally, we were able to perform some experiments on a three- and four-link robot to show the utility of our analyses, as well as primitive navigation results.

Chapter 5

Interactions with the Ambient Medium

We now consider systems in which the locomotion of individual robots is due to interactions with external forces or inputs. In these examples, the environment itself may be passive, such as a constant force field, or it may be manipulated via user command. As a result, the robot would have to coordinate its internal actuation with the external interactions; if it is passive like the example of the previous chapter, then we additionally have to again take into account base dynamics. We start with an example of the three-link robot in a gravitational field to motivate the problem and show possible novel behaviors that arise. The second example is having the robot placed on an actuated medium, in which we illustrate the stratified bundle structure as well as the problem of symmetry-breaking fibers. Finally, we close with a slightly different example system, the snakeboard, in order to show interactions between external viscous friction and a dynamic robotic system.

5.1 Constant Force Field

Recall that a general m-link robot enters a singular configuration when its joint angles α_i all become equal in value. In addition, we showed for the three-link case (and indeed this is also true for a generalized m-link case) that the robot becomes

dynamic and starts to drift it were to remain in such a configuration. In our previous analysis, this behavior did not come into play in motion planning, whether a robot was fully or partially actuated; any gaits that were used had the robot simply passing through a singularity rather than remaining in one. We now return to this system and consider placing it in a constant force field, *e.g.*, gravity due to the robot being on a slope. If one of the joints of a three-link robot remains completely passive, the other can be switch-controlled so that the robot can enter or exit the singular configuration and take advantage of its drifting behavior.

Gravity introduces a potential energy term in the form of

$$U_\beta = \beta \sum_{i=1}^{3} M_i^l y_i, \tag{5.1}$$

which can be subtracted from the kinetic energy to form a new Lagrangian $L_\beta = T - U_\beta$. Here β governs the strength of the gravitational force, while y_i is one of the *inertial* fiber variables decribing the position of the ith link. Recall that when a joint becomes passive, we gain an unactuated degree of freedom in the passive joint, normally specified by the evolution of its dynamics. This degree of freedom can be "pulled" by gravity into the singular configuration since internal actuation alone is insufficient to do so. On the other hand, the introduction of gravity does not affect the robot's kinematic operation when both joints are actuated, as the three constraints sufficiently determine the evolution of the three group variables.

The presence of gravity means that the group symmetries are broken—specifically, the Lagrangian L_β now has an explicit dependence on the group configuration. The three equations corresponding to the group variables can be rederived using L_β, and we include a fourth equation for the passive joint:

$$\frac{d}{dt}\left(\frac{\partial L_\beta(q,\dot{q})}{\partial \dot{\alpha}^j}\right) - \frac{\partial L_\beta(q,\dot{q})}{\partial \alpha^j} = (\omega_r)_j \lambda. \tag{5.2}$$

The λ is again the vector of constraint forces, while $(\omega_r)_j$ is the row of $\omega_r(r)$ from Eq. (2.4) corresponding to the unactuated joint.

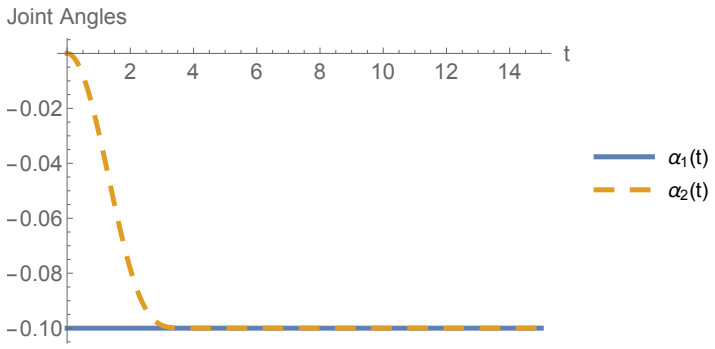

Figure 5-1: Simulation showing the passive joint α_2 converging to the value of the locked joint α_1, entering a singular configuration, as the system rolls down a hill (locomotes due to the effect of a constant force field).

In order to show that our new arrangement solves the problem of unbounded constraint forces, consider the simulation results shown in Fig. 5-1, with β set to 10. Here we start the system with $\theta = 0.1$ and $\alpha = (-0.1, 0)^T$, so that the first link is oriented "downward" while the other two are horizontal with respect to the slope direction. By keeping α_1 locked and leaving α_2 passive, the system obeys the dynamic equations and starts moving down the hill. At the same time, we see that the passive joint converges to the value of the locked one, naturally moving into a singular configuration.

5.1.1 Stability

A simple observation about the stability of such a maneuver and the singular configuration can be made using a standard Lyapunov function $V(\alpha) = (\alpha_1 - \alpha_2)^2$. It is positive as long as $\alpha_1 \neq \alpha_2$. We can then compute the time derivative

$$\dot{V}(\alpha) = 2(\alpha_1 - \alpha_2)(\dot{\alpha}_1 - \dot{\alpha}_2). \tag{5.3}$$

For the simulation above, $\dot{\alpha}_1 = 0$ and α_2 starts at a greater value than α_1. Since gravity pulls on the system such that $\dot{\alpha}_2$ is negative from the starting configuration, we have that $\dot{V}$ is negative and the singular configuration is asymptotically stable in this particular domain.

In general, Eq. (5.3) says that the singular configuration is stable as long as gravity

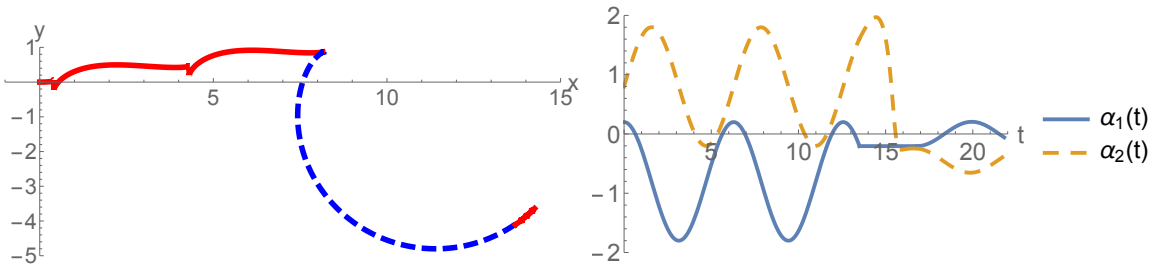

Figure 5-2: Illustration of a switching controller on the full hybrid model in a gravitational force field. Red portions of the trajectory indicate kinematic control, while the blue (dashed) portion indicates a locked-passive joint configuration acted upon by external forcing.

is either opening or closing the passive joint to match the locked one. For example, we would not have the same guarantee if we kept the same initial conditions as the previous simulation but flipped the robot around so that $\theta = \pi + \epsilon$, where ϵ is small and positive. Gravity would pull in the opposite direction and tend to "open" α_2 away from α_1. Another consideration is that such a statement only holds starting from rest; after the system gets moving, its momentum may interact with gravity to produce non-trivial joint behavior.

5.1.2 Switching Controller

These observations suggest a switching controller for maneuvering downward on a hill without joint actuation. By starting at rest and locking one joint, the system will converge to the singular configuration and traverse an arc down the hill with a curvature determined by the locked joint angle. To stop anywhere along the resultant trajectory, both joints can be actuated from zero with opposite velocities, popping the system out of the singular configuration and leaving us with full kinematic control once again.

Fig. 5-2 shows an example of such a composite trajectory combining a kinematic controller with dynamic movement. For the first part of our trajectory, we use the

simple gaits

$$\alpha_1(t) = \cos t - 0.8,$$
$$\alpha_2(t) = \sin t + 0.8,$$

which avoid singularities and locomote the system mostly in the x direction with some displacement in y. The first red solid portion of the trajectory plot shows the resultant movement from time $t = 0$ to $t = 13.5$.

The second part of the trajectory, shown in blue dashed, involves the system rolling dynamically down the hill starting from its current group configuration. We lock α_1 at its value at $t = 13.5$; practically, any other desired value can also be chosen since we still assume full control of the joint, and the locked angle determines the curvature of the trajectory undertaken by the system. For α_2, we make it passive starting from its current value, but it can also be reoriented closer to α_1 if necessary. As shown in the joint angles plot, α_2 moves toward α_1, overshoots, and corrects back as the system rolls down along the circle trajectory. With the joint angles staying so close together, such a maneuver would incur high constraint forces if relying on internal joint actuation.

In the third and final segment, we again assume full kinematic control of the system. From the current values of the joint angles at $t = 16.8$ we start actuating both joints with opposite velocities to move them away from each other. The last segment traveled is shown in the rightmost part of the trajectory in red in Fig. 5-2. The joint angles may now be controlled, again with the aid of curvature functions or other kinematic tools, to approach the most appropriate gaits for the next part of the desired trajectory.

One can potentially combine the different gaits explored to order to produce more flexible and complex trajectories. An example motion plan is shown in Fig. 5-3, where we stitch together two singularity-crossing gaits with a locked joint maneuver between them. The first and third parts of the motion plan effectively allow the system to move forward, as we recall that net reorientation is zero or minimal with a

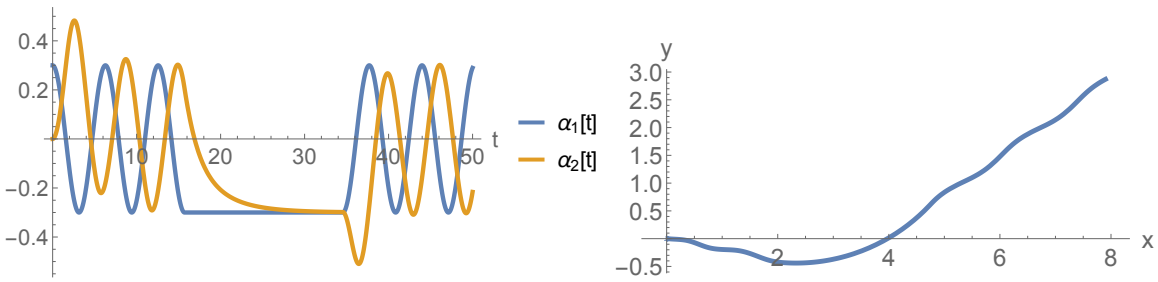

Figure 5-3: A trajectory that combines the forward gait with the dynamic rolling gait for reorientation.

gait symmetric about $\alpha_2 = 0$. The intermediate part pins the system on a trajectory with constant known curvature, so this can be used to achieve a rotational transition when desired. By combining individual trajectories like these in different ways, the robot can travel between any two neighborhoods in SE(2), a significant result as we are only controlling one degree of freedom at any given time.

5.2 A Controllable Medium

In the previous example, the robot's environment did not fundamentally change the overall system's configuration space; rather, it contributed additional dynamics that acted on the robot directly. Now we consider an environment that both increases configuration complexity and again causes a loss of symmetries. The example here is that of the same three-link robot placed atop a movable platform.

5.2.1 Snake Robot on a Platform

The addition of the platform to the snake robot system, as shown in Fig. 5-4, necessitates a modification of the configuration space. The position of the platform, denoted by (x_p, y_p), is itself a symmetry goup G_p since the modified system's properties do not depend on where the platform is located in space. The configuration manifold is now rewritten as $Q_p = G \times G_p \times B = \mathrm{SE}(2) \times \mathbb{R}^2 \times \mathbb{T}^2$, although it is important to note that the connection relationship of Eq. (2.5) still holds, as the nonholonomic constraints depend solely on how the robot moves relative to the platform.

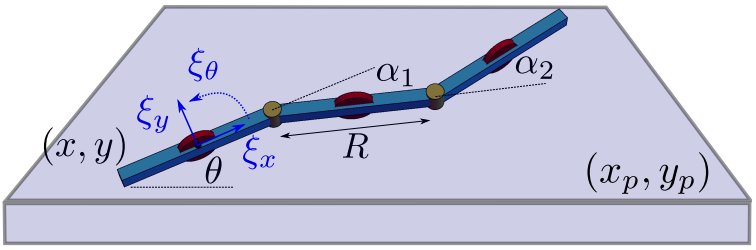

Figure 5-4: A three-link nonholonomic snake robot on top of a movable platform. The platform's inertial position is given by (x_p, y_p).

Suppose that each of the links has identical mass M^l and a moment of inertia J, while the platform has a mass M^p. Denoting the absolute positions of each of the links as $(\tilde{x}_i, \tilde{y}_i) = (x_i, y_i) + (x_p, y_p)$, the Lagrangian of the system is

$$L = \frac{1}{2}\sum_{i=1}^{3}\left(M^l(\dot{\tilde{x}}_i^2 + \dot{\tilde{y}}_i^2) + J\dot{\theta}_i^2\right) + \frac{1}{2}M^p(\dot{x}_p^2 + \dot{y}_p^2).$$

The momentum components of the entire moving system are given by the projection of $\frac{\partial L}{\partial \dot{q}_t}$ onto the directions of motion allowed by the constraints [11]. Since the constraints are independent of $\dot{x}_p$ and $\dot{y}_p$ while completely determining the trajectories of $(\dot{x}, \dot{y}, \dot{\theta})$, the free directions of motion are simply the degrees of freedom of the platform. The conserved momenta are given by

$$p = \begin{pmatrix} p_1 \\ p_2 \end{pmatrix} = \begin{pmatrix} \frac{\partial L}{\partial \dot{x}_p} \\ \frac{\partial L}{\partial \dot{y}_p} \end{pmatrix} = \rho_g(b)\dot{g} + \rho_b(b)\dot{b}. \tag{5.4}$$

Noting that the form of Eq. (5.4) is the same as the non-reduced form of Eq. (2.4), we can stack them together to obtain a set of full-rank equations, which we can then rearrange to obtain

$$\begin{pmatrix} \dot{x}_p \\ \dot{y}_p \end{pmatrix} = -\begin{pmatrix} \cos\theta & -\sin\theta \\ \sin\theta & \cos\theta \end{pmatrix} A_2(b)\dot{b} + \frac{1}{M}\begin{pmatrix} p_1 \\ p_2 \end{pmatrix}. \tag{5.5}$$

where $M = 3M^l + M^p$.

Here, the matrix $-A_2(b)$ is the external connection of our now stratified bundle

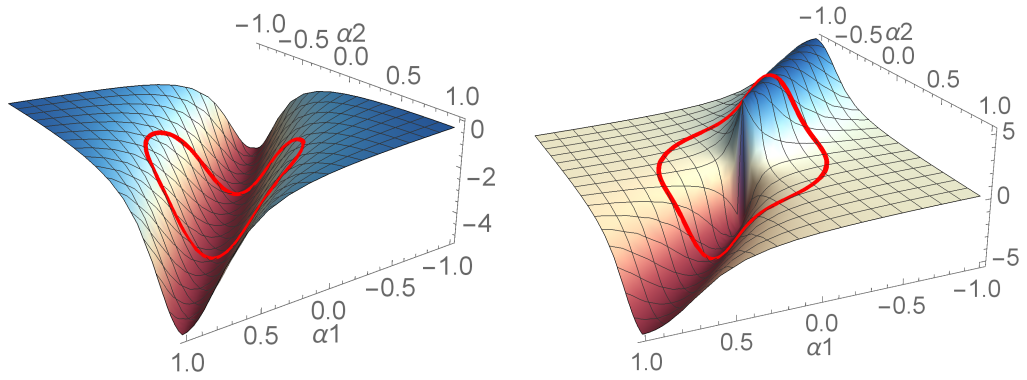

Figure 5-5: The u_p (top) and v_p (bottom) components of the connection exterior derivative for the platform.

structure. It is also the local form of the *mechanical connection*, again named because it is derived from the conservation of momentum for the combined robot-platform system. In practice, we can drop the momentum drift terms if the platform starts at rest. The main complexity comes from the rotation matrix in front of the mechanical connection—the range of the connection is still the robot's Lie algebra, or velocities expressed in the robot-fixed frame. In the next subsection we first bypass this problem by keeping track of the platform in the robot's body frame.

5.2.2 Platform Position in Robot's Body Frame

In deriving Eq. (5.5) we noted that the main difficulty in using it, even after dropping the drift terms using a start from rest assumption, is the presence of the rotation matrix. This relationship signifies a dependence on θ, the orientation of the robot relative to the platform (and inertial frame). However, if we know or can prescribe the platform's position with respect to the robot's body frame[1], we can directly use the external, mechanical connection $-A_2(b)$ without accounting for the effect of θ on the robot-platform interaction. In other words, we can choose to specify the platform's

[1]Of course, this assumes that we free control over the platform's motion in all directions, rather than along a set of fixed axes.

velocity using the variables

$$\begin{pmatrix} \dot{u}_p \\ \dot{v}_p \end{pmatrix} = \begin{pmatrix} \cos\theta & \sin\theta \\ -\sin\theta & \cos\theta \end{pmatrix} \begin{pmatrix} \dot{x}_p \\ \dot{y}_p \end{pmatrix}. \tag{5.6}$$

Again assuming that the system starts from rest, Eq. (5.5) then reduces to

$$\begin{pmatrix} \dot{u}_p \\ \dot{v}_p \end{pmatrix} = -A_2(b)\dot{b}. \tag{5.7}$$

Since $-A_2(b)$ plays a role identical to that of the kinematic connection for the robot, we can also plot its exterior derivative in the same way that we have done for the robot. Fig. 5-5 shows their shape for a set of chosen system parameters. The main observation one finds from these plots is that the x_p plot is in general a flipped version of the robot's x connection curvature plot (Fig. 2-6).

As the robot moves in the forward or backward direction, we would expect the platform to tend to move in the opposite direction, preserving net initial momentum of zero. Interestingly, exterior derivative for v_p (motion of the platform in a direction lateral to the robot's heading) looks like the robot's θ connection curvature flipped. This is sensible since rotating the robot also rotates the attached body frame, meaning that the initial progression of the platform along the robot's longitudinal direction now rotates into the lateral direction.

With the derivation of Eq. (5.7) we are now also able to consider the novel problem of controlling the platform's locomotion and inducing a completely passive robot to move. In other words, we will assume that we prescribe $(\dot{u}_p, \dot{v}_p)$ in order to cause motion in the robot's fiber components ξ. This problem thus amounts to using Eq. (5.7) to find resultant base trajectories given a set of platform velocity inputs, and then lifting those trajectories to ξ using Eq. (2.5).

In this case, "inverting" Eq. (5.7) really amounts to analyzing and solving a first-order ODE for the unknown shape trajectories $b(t)$. Moreover, since we already have the external connection $-A_2(b)$ and its associated visualizations (Fig. 5-5), we can

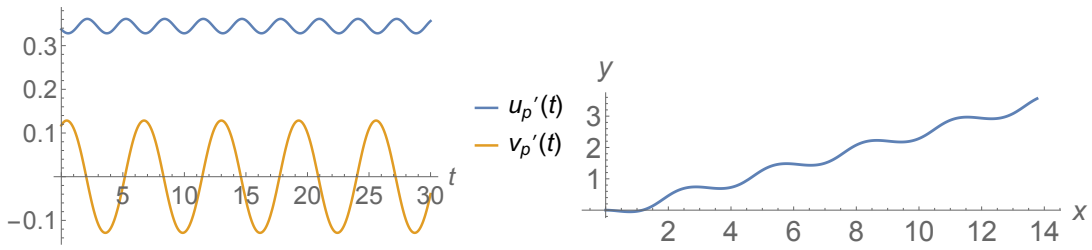

Figure 5-6: Top: The platform velocity inputs, relative to the robot's body frame, required to obtain the base gait in Fig. 5-5. Bottom: The robot's resultant fiber trajectory, which advances forward without reorientation, as expected.

use these to inform the types of platform trajectories we should prescribe to obtain desired shape trajectories. For example, suppose that we want the simple origin-centered loop shown in red in Fig. 5-5. This gait has the effect of moving the robot forward without reorienting it. From Eq. (5.7) and Fig. 5-5 we can find that the corresponding platform trajectory is that shown in Fig. 5-6 (top). Then, using this as the input to the system we see that we do indeed obtain the fiber trajectory of the robot, as shown in Fig. 5-6 (bottom).

Of course, one of the main drawbacks with the above approach is that there is no guarantee on the feasibility of platform input. For example, the required input of Fig. 5-6 requires a constant nonzero offset in $\dot{u}_p(t)$, meaning that the platform would essentially have to move on the plane with the robot. If we are able to directly invert Eq. (5.7), *i.e.*, specify $(\dot{u}_p, \dot{v}_p)$ to obtain a desired $\dot{b}$, then we can restrict ourselves to feasible inputs only.

That Eq. (5.5) is reduced, *i.e.*, we have eliminated all robot fiber dependencies from the equation, allows us to consider only the interaction between the robot's joints and the platform fiber variables. Furthermore, the equation bears a resemblance to the dynamics between a set of actuated and a set of unactuated joints on the same robot; the only difference is that the "actuated joints" in this case are external to the robot. This time, applying the *harmonic balance* method to analyze Eq. (5.5) shows that periodic inputs $(\dot{u}_p, \dot{v}_p)$ with no offset will also yield periodic joint trajectories in $\dot{b}$, whose magnitude, offset, and phase depend on functions of the inputs' magnitude and phase.

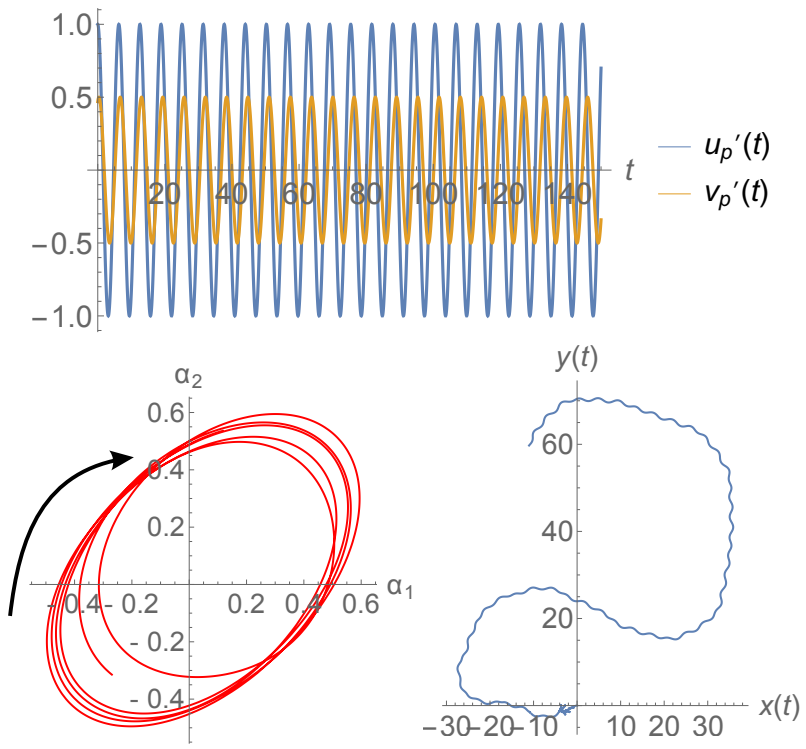

Figure 5-7: Top: A set of platform inputs in which the relative phase increases over time. Bottom left: The offset of the gait in shape space shifts from the third quadrant to the first. Bottom right: The resulting fiber motion of the robot, initially a trajectory with a negative curvature and then shifting to a positive one.

For example, it can be numerically shown that increasing the relative phase between the two input directions will increase the offset of the resultant joint trajectories. Such a gait is shown in Fig. 5-7 (top); note that $\dot{v}_p$ lags $\dot{u}_p$ more and more over time. This has the effect of shifting the center of the gait in shape space (Fig. 5-7, bottom left) from the third quadrant to the first quadrant. As we know from the θ connection curvature, gaits with negative offsets in α_1 and α_2 acquire negative net orientation; gaits with positive offsets acquire positive net orientation. In addition, the robot continues to move forward in its body direction while rotating, since all gaits enclose a positive net area in the x connection curvature. All of these observations are apparent in the robot's fiber trajectory for this simulation (Fig. 5-7, bottom right). It starts at the origin moving forward on a trajectory rotating clockwise (negative curvature) and halfway in starts rotating counterclockwise (positive curvature), as the relative

phase between $\dot{u}_p$ and $\dot{v}_p$ becomes large and the center of the resulting α_1-α_2 gait becomes positive.

5.2.3 Inputs in the Inertial Frame

In the previous subsection, the assumption that we can actuate the underlying platform relative to the robot body's longitudinal and lateral directions requires that the platform can freely move in *all* directions. An alternative scenario is that it may be limited to move only in two fixed directions, corresponding to two independent degrees of freedom. Assuming that the system starts from rest, this model is described exactly by Eq. (5.5).

Even if the system again starts from rest, dropping the momenta terms from the equation, the dependency of Eq. (5.5) on the robot's orientation θ introduces an additional complexity. We assume that we know the robot's orientation throughout the system's operation, for example via an overhead camera, so that θ is not an unknown quantity. However, it is a symmetry-breaking fiber variable that changes the form of the connection $-A_2(b)$ and its corresponding exterior derivative plots in Fig. 5-5.

Fig. 5-8 shows the effect of θ on $\mathrm{d}A_2(b)$; in other words, the plots show the exterior derivative, for different values of θ, of a θ-dependent connection

$$A_\theta(\theta, b) = \begin{pmatrix} \cos\theta & -\sin\theta \\ \sin\theta & \cos\theta \end{pmatrix} A_2(b). \tag{5.8}$$

The plots shown correspond to θ at 45, 90, and 180 degrees (of course, the nominal plots of Fig. 5-5 correspond to $\theta = 0$). As we would expect, the nature of the interaction between the robot and platform changes with the former's orientation. As the robot rotates to 90 degrees, its body x axis points along the inertial y axis, while its body y axis points along the inertial $-x$ axis. The x_p plot is thus identical to the $-v_p$ plot in Fig. 5-5, while y_p is identical to u_p. At 180 degrees, both x_p and v_p are completely inverted from u_p and v_p, the latter again corresponding to x_p and y_p

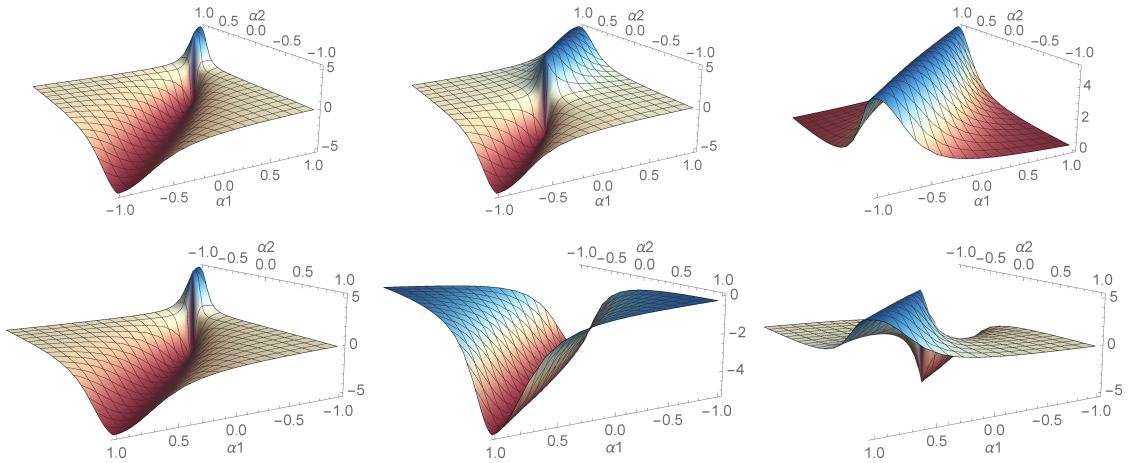

Figure 5-8: The x_p (top) and y_p (bottom) components of the connection exterior derivative for the platform, corresponding to the robot's orientation θ at 45 (left), 90 (middle), and 180 degrees (right). The case in which the robot is aligned with the platform ($\theta = 0$) is the same as the plots in Fig. 5-5. Note that the plots undergo an inversion as θ increase from 0 to 180.

at 0 degrees. Finally, as the robot reorients back to 0 degrees, both plots smoothly deform back to their nominal forms (Fig. 5-5).

With a varying θ, robot base trajectories no longer solely lie on the α_1-α_2 plane in interacting with the inertial platform velocities $\dot{x}_p$ and $\dot{y}_p$. However, we are able to simplify this problem and reduce motion planning to analysis of a single exterior derivative function as before if θ is known to be periodic. In other words, the robot may start out at some arbitrary orientation, but its net motion only moves it forward in the body direction and does not turn it away from its initial orientation. From Fig. 2-6 we know that such gaits are centered about the origin.

What we can do here is to *decouple* the dependency of the fiber trajectories on the evolution of the non-symmetric fiber $g^n = \theta$. Assuming that the joint trajectories α_1 and α_2 are also periodic, we can apply harmonic balance on the third line of Eq. (2.5), a first-order differential equation $\dot{\theta} = f(b, \dot{b})$, to obtain a solution for $\theta(t)$ in terms of

the parameters of $\alpha_1(t)$ and $\alpha_2(t)$. In other words, if

$$\alpha_1(t) = B_1 \cos(\omega t),$$
$$\alpha_2(t) = B_2 \cos(\omega t - \phi),$$

then we can find

$$\theta(t) = \Theta \cos(\omega t - \psi) + C,$$

where Θ, ψ, and C are functions of B_1, B_2, and ϕ. Taking this procedure one step further, we can apply trigonometric identities to write

$$\theta = a_1\alpha_1 + a_2\alpha_2 + C, \tag{5.9}$$

where a_1 and a_2 are the solutions of the nonlinear equations

$$\Theta = \sqrt{(a_1B_1)^2 + (a_2B_2)^2 + 2a_1a_2B_1B_2\cos\phi},$$
$$\psi = -\text{atan2}(-a_2B_2\sin\phi, a_1B_1 + a_2B_2\cos\phi).$$

The unknowns can be analytically solved as

$$(a_1, a_2) = \pm\left(\frac{\Theta\sin(\phi-\psi)}{B_1\sin\phi}, \frac{\Theta\sin\psi}{B_2\sin\phi}\right). \tag{5.10}$$

With the numerical values of a_1 and a_2 in hand, we can substitute Eq. (5.9) into Eq. (5.8) and obtain a reduced connection mapping solely between the joint variables b_w and the platform fiber variables x_p and y_p, without regard to θ. Again, this new connection assumes that θ is periodic and is only valid for the given or known functional form of θ, whether through analysis or visual tracking. With this connection form, however, we are able to reduce the previous exterior derivative plots from three dimensions (α_1, α_2, and θ) back down to two (α_1 and α_2 only).

Two "effective" connection exterior derivatives over different ranges of θ are shown

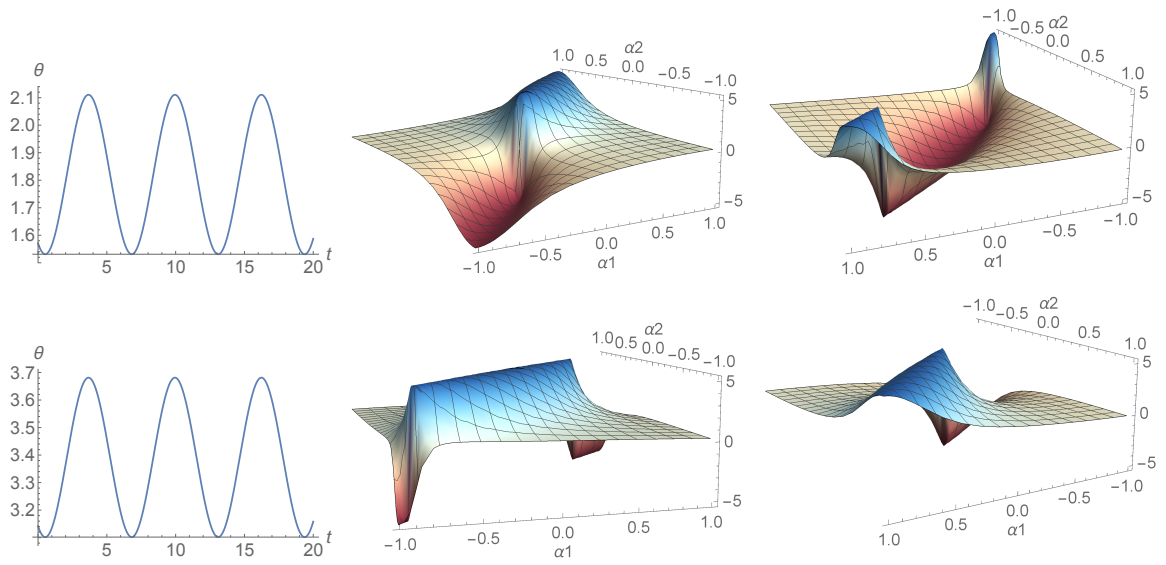

Figure 5-9: Top: The exterior derivatives of an "effective" A_θ for θ between $\frac{\pi}{2}$ and $\frac{2\pi}{3}$ (middle plot corresponding to x_p, right to y_p). Bottom: Same functions but for θ between π and $\frac{7\pi}{6}$. Note that some of the plots appear relatively unchanged from those of Fig. 5-8; the others acquire deformations starting from the edges.

in Fig. 5-9. In the first row, θ has a range from about $\frac{\pi}{2}$ to about $\frac{2\pi}{3}$; in the second, θ ranges from about π to about $\frac{7\pi}{6}$. In both rows, the representative exterior derivative functions corresponding to x_p and y_p are shown. Interestingly, the x_p plot in the first row and y_p plot in the second row are not very different from their constant θ counterparts at 90 and 180 degrees, respectively. This indicates that those particular surfaces are more stable and hold over large ranges of θ. On the other hand, the other two plots are noticeably different, particularly on the edges. In both the y_p plot in the first row and x_p plot in the second, the edges are the first regions to deform as θ changes.

Given that we are able to find single representative connection derivative plots over a given range of θ, we can use this visual tool for locomotion analysis and planning for the robot-platform system, whether the inputs are applied to the robot on a passive platform or to an actuated platform underneath a passive robot. Of course, the weakness of this approach is that the computed connection only holds for the specific θ range. If this range changes, whether by shifting or scaling, a new connection must be found.

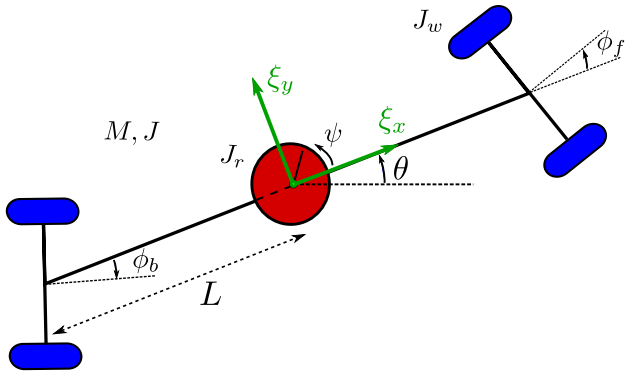

Figure 5-10: The configuration of the snakeboard. Parameters include M, L, J, J_r, and J_w. The joint angle inputs are ψ and $\phi = \phi_f = -\phi_b$. We can define a body frame at the rotor, giving us body velocities ξ_x, ξ_y, and ξ_θ.

5.3 Dissipative Friction

The last example of external dynamics that we consider in this chapter is that of a locomoting system being affected by friction. Unlike the other two cases, the system cannot take advantage of friction to help it locomote, nor can we manipulate this effect. Instead, a more realistic problem is finding motion controls for the system that would work similarly to the case in which friction is not present. We detail our work here with the *snakeboard* system, shown in Fig. 5-10. This system can move by means of turning two nonholonomic wheelsets, one in the front and one in the back of the body, as well as a momentum wheel in the center. Opposite to the three-link snake robot, it is dynamic since there are fewer constraints (two) than fiber degrees of freedom (three). However, because it has an analytical motion planning solution [22], we can use this example to illustrate how to modify such a solution when viscous friction is added.

5.3.1 Snakeboard Locomotion

The snakeboard's configuration is given by $q \in Q = (g, b)$, where the position variables $g = (x, y, \theta) \in G = SE(2)$ locate the snakeboard in the world and the shape variables $b = (\psi, \phi) \in M = \mathbb{S}^1 \times \mathbb{S}^1$ describe the joint configurations. The variables x and y denote the global position of the center of mass at the rotor, while θ denotes the

system's orientation with respect to the inertial x axis. ψ denotes the rotor angle, and ϕ_f and ϕ_b denote the angles of the front and back wheels, respectively, with respect to the longitudinal axis. We enforce the constraint $\phi_f = -\phi_b$ and henceforth use $\phi = \phi_f$.

The snakeboard's body frame is situated at the rotor, with its velocities ξ representing components in the forward, lateral, and rotation directions. We can relate ξ to the world velocity $\dot{g} = (\dot{x}, \dot{y}, \dot{\theta})$ by the usual mapping

$$\xi = \begin{pmatrix} \xi_x \\ \xi_y \\ \xi_\theta \end{pmatrix} = T_g \Phi_{g^{-1}} \begin{pmatrix} \dot{x} \\ \dot{y} \\ \dot{\theta} \end{pmatrix}. \tag{5.11}$$

The snakeboard's mass and inertia are denoted M and J, while the rotor and wheel inertias are denoted J_r and J_w. We assume that $ML^2 = J + J_r + 2J_w$ is the total inertia of the system, where the total length of the snakeboard is $2L$.

The snakeboard's Lagrangian is invariant to changes in the system's position or orientation in space ($SE(2)$) due to symmetry, so we can express it in body velocities instead of world velocities. The Lagrangian in the body frame becomes

$$l(\xi, \dot{r}) = \frac{1}{2} M(\xi_x^2 + \xi_y^2 + L^2 \xi_\theta^2) + \frac{1}{2} J_r \dot{\psi}^2 + J_r \xi_\theta \dot{\psi} + J_w \dot{\phi}^2. \tag{5.12}$$

Standard models assume no-slip nonholonomic constraints on the wheelsets. Like the Lagrangian, the constraints are invariant with respect to transformations in SE(2), so they can be written in terms of the local body coordinates only. They can be expressed in Pfaffian form $\omega(r)\xi = 0$, where

$$\omega(r) = \begin{pmatrix} \omega_f \\ \omega_b \end{pmatrix} = \begin{pmatrix} -\sin\phi & \cos\phi & L\cos\phi \\ \sin\phi & \cos\phi & -L\cos\phi \end{pmatrix}. \tag{5.13}$$

Instead of writing out the full Euler-Lagrange equations of motion, we take advantage of the nonholonomic constraints to derive the reduced equations of motion. From (5.12) and (5.13) we first compute the *nonholonomic momentum* using the definition

$p_{\text{nh}} = \langle \frac{\partial l}{\partial \xi}; \Omega \rangle$, where Ω is a basis of the null space of ω. We choose $\Omega = (L, 0, \tan\phi)^T$ and find

$$p_{\text{nh}} = ML(\xi_x + L\xi_\theta \tan\phi) + J_r\dot{\psi}\tan\phi. \tag{5.14}$$

Next we examine how joint velocities and momentum determine resultant body velocities. Combining the constraints (5.13) and the momentum definition (5.14), we find the following *reconstruction equation*.

$$\xi = -\begin{pmatrix} \frac{J_r \sin 2\phi}{2ML} & 0 \\ 0 & 0 \\ \frac{J_r \sin^2\phi}{ML^2} & 0 \end{pmatrix} \begin{pmatrix} \dot{\psi} \\ \dot{\phi} \end{pmatrix} + \begin{pmatrix} \frac{\cos^2\phi}{ML} \\ 0 \\ \frac{\sin 2\phi}{2ML^2} \end{pmatrix} p_{\text{nh}} \tag{5.15}$$

Finally, we solve for the *momentum evolution equation*, which describes how the momentum changes in time. Referencing the formulation in [72], we have

$$\dot{p}_{\text{nh}} = \left\langle \frac{\partial l}{\partial \xi}; [\xi, \Omega] + \dot{\Omega} \right\rangle = \dot{\phi}\sec^2\phi(ML^2\xi_\theta + J_r\dot{\psi}), \tag{5.16}$$

where $[\cdot, \cdot]$ denotes the Lie bracket operation. If we substitute in the constraint equations $\omega(r)\xi = 0$, we can eliminate the body velocities and obtain a differential equation in p_{nh}.

$$\dot{p}_{\text{nh}} = \dot{\phi}(p_{\text{nh}}\tan\phi + J_r\dot{\psi}) \tag{5.17}$$

Equations (5.15) and (5.17) constitute the first-order equations of motion for the snakeboard. Given shape inputs ϕ, ψ, and their derivatives, we can completely determine the snakeboard's configuration velocities. In particular, [76, 77] developed periodic inputs, or gaits, to achieve motion primitives such as forward movement, rotation, and parallel parking.

Motion Planning

Given a desired trajectory in space, the motion planning problem is to determine the joint inputs that will allow the snakeboard's COM to track it. A trajectory in $SE(2)$ is often described in inertial coordinates as functions of time; by the fundamental

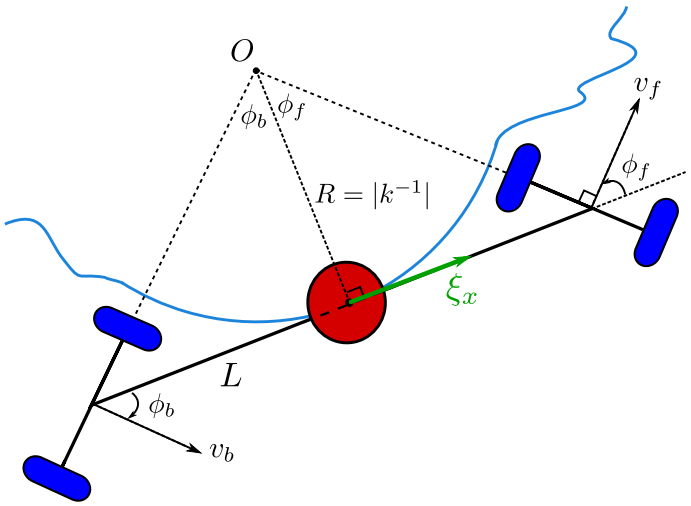

Figure 5-11: The geometry of the snakeboard's trajectory. The COM's velocity is instantaneously tangent to a path with curvature κ. This allows us to define a circle with radius R, with the wheelset axes intersecting at the circle center O.

theorem of curves [28], one can equivalently use an arclength and curvature parameterization. Let $r(t)$ denote the distance along the path, at time t, from the path starting point; for example, if t_0 is the starting time, then $r(t_0)$ is necessarily equal to 0. Let $\kappa(r)$ denote the curvature along the path. We can then define $c(t) := \kappa(r(t))$ to be the path curvature as a function of time. For example, $c(t_0) = \kappa(0)$ is the curvature of the path starting point.

As in [91] and [22], we also require ξ_x to be instantaneously tangent to the path while the COM tracking it, as shown in Fig. 5-11. If the local curvature at the point of contact is κ, then $R = |\kappa^{-1}|$ is the radius of curvature from the instantaneous center of rotation O. The snakeboard can then be represented by a generalized bicycle model, which requires that the wheelsets' disallowed directions of motion meet at O. This provides us a simple geometric solution for the wheel angle input in terms of the known path curvature function.

$$\phi(t) = \tan^{-1}(Lc(t)) \tag{5.18}$$

We can now establish a relationship between the body velocities and the trajectory profile. First we note that imposing the body tangency requirement enforces that

$\xi_x(t)$, the forward velocity of the snakeboard, be exactly equal to $\dot{r}(t)$, the magnitude of the velocity vector along the trajectory. Combining this with the constraints (5.13), we have that

$$\xi(t) = \begin{pmatrix} \xi_x(t) \\ \xi_y(t) \\ \xi_\theta(t) \end{pmatrix} = \begin{pmatrix} \dot{r}(t) \\ 0 \\ c(t)\dot{r}(t) \end{pmatrix}. \tag{5.19}$$

In the last step, we solve for the rotor input profile, $\dot{\psi}(t)$. If we differentiate the momentum in (5.14) and equate it to (5.17), we can eliminate p_{nh} and obtain an equation in the body velocities and shape variables. Replacing the body velocities with trajectory information using (5.19), we can obtain a solution for $\ddot{\psi}(t)$ (and via integration, $\dot{\psi}(t)$).

$$\ddot{\psi}(t) = -\frac{M}{J_r}\left(\frac{1}{c(t)} + L^2 c(t)\right)\ddot{r}(t) - \frac{ML^2}{J_r}\dot{c}(t)\dot{r}(t) \tag{5.20}$$

Given (5.18) and (5.20), the joint inputs can be numerically determined from the curvature and velocity profile of the desired trajectory. Certain trajectories may yield analytical solutions for $\dot{\psi}$ by explicit integration of (5.20). Dear et al. [22] goes over these special trajectories in more detail, along with cases of zero and infinite curvature; it is shown that we lose controllability in the former case, whereas the latter can be dealt with using angular momentum conservation.

5.3.2 Viscous Friction in Travel Direction

We now consider friction acting on the wheels in the direction of travel. Ostrowski [72] represented these forces by a group-invariant Rayleigh dissipation function, deriving the new reduced equations and illustrating the results on the snakeboard's forward equations. We first briefly review these results and then incorporate them into the inverse planning solutions for ϕ and $\ddot{\psi}$.

Motion Planning Solution

In order to define the dissipation function, we require the velocities at the center of each wheelset. Analogous to constraint directions $\omega(r)$ in (5.13), we can write down similar equations for the reduced forward velocities of the wheelsets:

$$\begin{pmatrix} v_f \\ v_b \end{pmatrix} = \begin{pmatrix} \cos\phi & \sin\phi & L\sin\phi \\ \cos\phi & -\sin\phi & L\sin\phi \end{pmatrix} \xi, \tag{5.21}$$

where v_f and v_b are the instantaneous velocity components of the front and back wheelsets, respectively (see Fig. 5-11).

We assume the same damping coefficient, k_d, for both wheelsets. Because the velocities in (5.21) are group-invariant, we can write a reduced *damping* Rayleigh dissipation function, proportional to the squares of the velocities.

$$R_{\text{damp}}(r,\xi) = \frac{1}{2} k_d (v_f^2 + v_b^2) \tag{5.22}$$

The inclusion of this dissipation function leaves our derivations unchanged up to the the momentum evolution equation (5.16). As shown by [72], the time change in momentum now takes on an additional term to account for the damping in the valid travel directions.

$$\dot{p}_{\text{damp}} = \left\langle \frac{\partial l}{\partial \xi}; [\xi, \Omega] + \dot{\Omega} \right\rangle - \left\langle \frac{\partial R_{\text{damp}}}{\partial \xi}; \Omega \right\rangle \tag{5.23}$$

The expression for p_{damp} is the same as that for p_{nh}; we introduce the new variable as its evolution equation (5.23) is different. Specifically, we can compute the new term by using the same Ω as before, and add the result to (5.17) to obtain

$$\dot{p}_{\text{damp}} = \dot{\phi}(p_{\text{damp}} \tan\phi + J_r \dot{\psi}) - \frac{2k_d}{M}(p_{\text{damp}} - J_r \dot{\psi} \tan\phi). \tag{5.24}$$

Note the change in behavior induced by the damping terms. As expected, there is a retarding force on the system proportional to its current momentum p_{damp}. If we

lock the wheelsets while locomoting ($\dot{\phi} = 0$), then p_{damp} exponentially approaches an equilibrium determined by $\dot{\psi}$. Ostrowski [72] showed the effect of a range of damping coefficients on various snakeboard gaits.

Our contribution is to incorporate the new damping terms into our joint solutions for the motion planning problem. Note that the wheel angle solution (5.18) does not change, as it is solely a function of trajectory curvature. On the other hand, if we follow the same process in solving for the rotor profile by differentiating (5.14) and equating it to (5.24), we obtain

$$\ddot{\psi}_{\text{damp}}(t) = \ddot{\psi}(t) - \frac{2k_d}{J_r}\left(\frac{1}{c(t)} + L^2 c(t)\right)\dot{r}(t). \tag{5.25}$$

Discussion and Simulations

The new solution (5.25) allows us to determine the required rotor input given a trajectory to track. Unlike in [22], we cannot find $\dot{\psi}(t)$ explicitly for general trajectories with constant velocity but varying curvature, due to integral dependence on $c(t)$. If instead we consider constant nonzero curvature c_0, we can obtain an analytical solution in the form

$$\begin{aligned}\dot{\psi}_{\text{cc}}(t) = &-\frac{M}{J_r}\left(\frac{1}{c_0} + L^2 c_0\right)(\dot{r}(t) - \dot{r}(t_0)) \\ &-\frac{2k_d}{J_r}\left(\frac{1}{c_0} + L^2 c_0\right)(r(t) - r(t_0)) + \dot{\psi}(t_0),\end{aligned} \tag{5.26}$$

where t_0 is the time at which $c(t)$ becomes constant.

Consider an example of a constant curvature trajectory with curvature function $c(t) = 0.1$ and a velocity profile $\dot{r}(t) = \sin^2(t)$. Here the snakeboard executes a periodic stop-and-go trajectory around a circle of radius 10. Along with the initial conditions $(x(0), y(0), \theta(0)) = (0, 0, 0)$, we use the following parameters, which will be the same in all simulations that follow.

$$M = 4, \quad J_r = 2, \quad J_w = 0.5, \quad J = 1, \quad L = 1$$

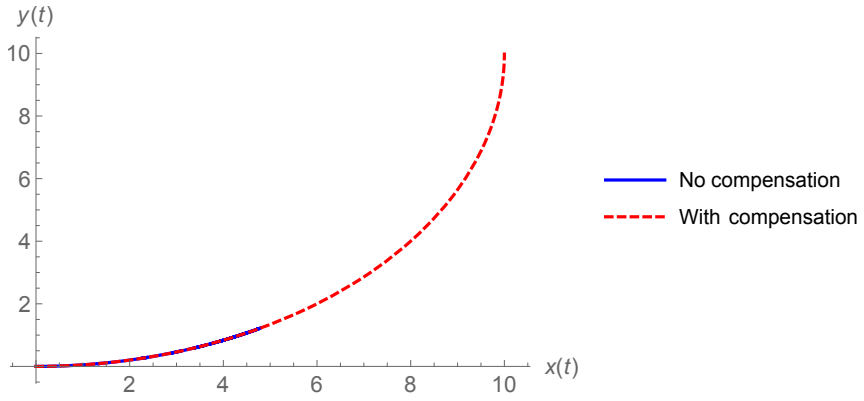

Figure 5-12: Comparison of resultant trajectories due to controllers without and with damping compensation. The latter is able to travel the required distance while the former lags far behind.

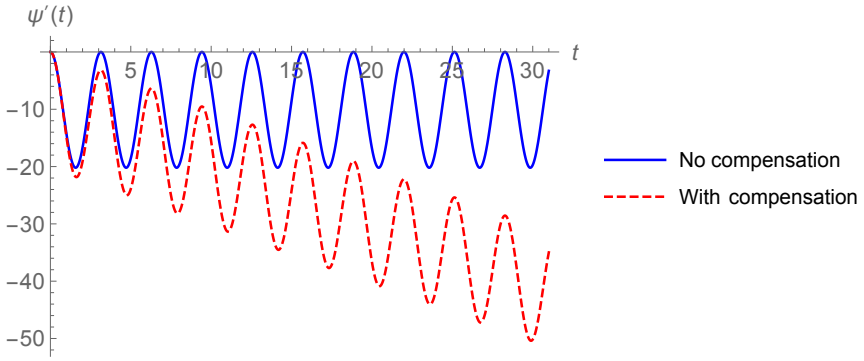

Figure 5-13: Rotor velocity comparison for scenario in Fig. 5-12. While the latter controller is superior for trajectory tracking, it causes the rotor velocity to grow unbounded.

Fig. 5-12 simulates the snakeboard's motion in the case of damping coefficient $k_d = 0.2$ for the two controllers (5.20) and (5.26) for about 31 seconds. Integrating our velocity function $\dot{r}(t)$ and evaluating the result at $t = 31$, we expect the system to have traveled a distance of about 15.7, or a quarter of the circle. This is exactly what we get with the damping-compensated controller (5.26), while the other is greatly slowed down by damping.

However, we note that for practical purposes the controller (5.26) may be difficult to implement. As shown in Fig. 5-13, the rotor velocity actually grows unbounded, while the original controller does not lead to this effect. This is expected because

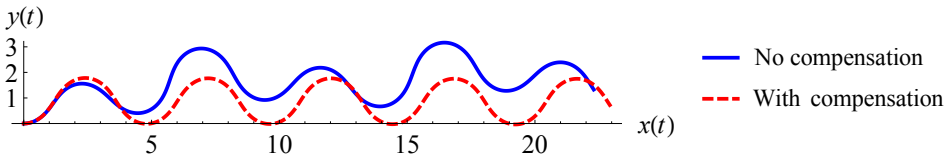

Figure 5-14: Serpenoid trajectory comparison for controllers without and with damping compensation. The latter controller for $\dot{\psi}$ saturates near small curvatures, but it is still able to track the desired path much more closely than the former.

the amount of damping compensation, which leads to a slightly greater rotor velocity each cycle, is cumulative as the snakeboard travels more distance.

The problem of unbounded rotor velocity can be addressed by utilizing a rotor "reset." To perform this maneuver, the snakeboard must be allowed to stop for a finite amount of time; hence $\dot{r}(t) = \sin^2(t)$ cannot be followed exactly. Once the system is stopped, we rotate its wheel angles to $\phi = 0$, rendering the snakeboard uncontrollable. Because it cannot locomote in this state, we can then reset its rotor velocity to 0, and then unrotate the wheel angles and resume as before. For further details on this technique, see [22].

For solutions of the general controller (5.25), this reset manuever may be particularly useful for nearly straight trajectories or dealing with corners or kinks in the path. As either $c \to 0$ or $c \to \infty$, $\dot{r}$ would have to decrease appropriately; in the limit, we have that a feasible $\dot{r}$ must be 0 and the snakeboard stops moving for both cases.

However, we can observe that if the system reaches these difficult conditions only momentarily, then (5.25) can still perform adequate tracking without deviating from the trajectory to reset. We consider the serpenoid curve [39], which is characterized by a curvature function of the form $c(t) = a\cos(bt)$, where a and b are parameters. Here we take $a = b = 1$ and prescribe constant unit speed ($\dot{r} = 1$). On this trajectory, the curvature periodically decreases to 0.

Fig. 5-14 compares the snakeboard's motion for the controllers (5.20) and (5.25), again with $k_d = 0.2$. For the latter, we clip the velocity where it becomes large (the clipping value is the maximum velocity from the solution of (5.20)). It is clear that even with the imposed saturation on the rotor, (5.25) produces a serpenoid trajectory

much closer to the friction-free case than that due to (5.20).

5.3.3 Skidding Orthogonal to Travel Direction

If the snakeboard's wheels skid, then the nonholonomic constraints are violated, as the wheel velocities have components in the no-travel directions. However, moving orthogonal to the directions of the wheelsets should still generate large resistive forces. We therefore propose to replace the "hard" nonholonomic constraints with "soft" dissipative forces, modeled by a *skidding* Rayleigh dissipation function.

$$R_{\text{skid}}(r,\xi) = \frac{1}{2}k_s\left((\omega_f\xi)^2 + (\omega_b\xi)^2\right) \tag{5.27}$$

Here, k_s is a skidding coefficient, and the vectors ω_f and ω_b are the same as those in (5.13). These directions are orthogonal to the ones used in the damping dissipation function (5.22).

Equations of Motion

To compute the equations of motion, we can evaluate the reduced Euler-Lagrange equations augmented with the dissipative forces from the Rayleigh dissipation function.

$$\frac{d}{dt}\left(\frac{\partial l(r,\xi)}{\partial \xi_i}\right) = -\frac{\partial R_{\text{skid}}(r,\xi)}{\partial \xi_i}; \quad i = x, y, \theta \tag{5.28}$$

Note that the partial derivatives of the Lagrangian with respect to the position variables vanish from the equations, as the Lagrangian is cyclic in those variables.

We can also reformulate the equations (5.28) in the form of a reconstruction equation together with a momentum evolution equation, analogous to (5.15) and

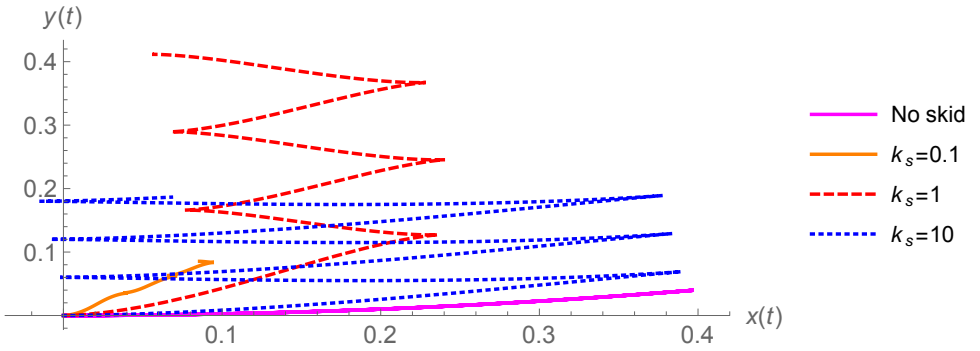

Figure 5-15: Resultant trajectories from constant curvature joint inputs over a range of skidding constants. The path degrades more and more from the ideal, no-skid case as k_s decreases.

(5.16). Referencing [46, 47] for the inclusion of dissipation in this form, we have

$$\xi = -\begin{pmatrix} 0 & 0 \\ 0 & 0 \\ \frac{J_r}{ML^2} & 0 \end{pmatrix} \begin{pmatrix} \dot{\psi} \\ \dot{\phi} \end{pmatrix} + \begin{pmatrix} \frac{1}{M} & 0 & 0 \\ 0 & \frac{1}{M} & 0 \\ 0 & 0 & \frac{1}{ML^2} \end{pmatrix} p \tag{5.29}$$

$$\dot{p} = \begin{pmatrix} -2k_s \sin^2(\phi) & 0 & k_s L \sin(2\phi) \\ 0 & -2k_s \cos(\phi) & 0 \\ k_s L \sin(2\phi) & 0 & -2k_s L^2 \cos^2(\phi) \end{pmatrix} \xi,$$

where $p = \frac{\partial l}{\partial \xi}$ is the *generalized momentum*. Unlike the nonholonomic momentum p_{nh}, there are three momenta components since there are no longer any hard constraints restricting the system's motion. From the above equations, we see that as $k_s \to 0$, it becomes harder to change p and subsequently ξ_x and ξ_y. Indeed, in the absence of friction entirely, applying a rotor input $\dot{\psi}$ will only affect angular velocity due to conservation of angular momentum.

To evaluate our model, we look at the behavior of the snakeboard over a range of skidding coefficients k_s. Consider the following shape inputs describing an oscillation along a constant curvature path, $\dot{\psi}(t) = -\sin(t)$ and $c(t) = 0.5$. With the regular nonholonomic constraints in place, the snakeboard oscillates along the same curve without going off its path, shown in Fig. 5-15. But if the system is allowed to skid,

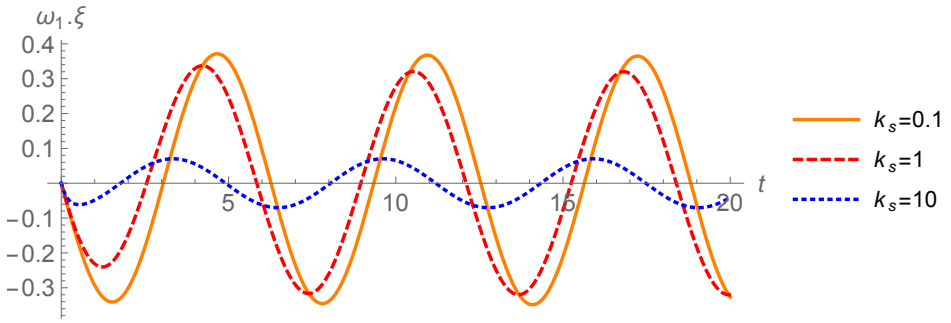

Figure 5-16: Front wheel velocities orthogonal to direction of travel (skidding velocities) for the trajectories in Fig. 5-15. The skidding components become larger as k_s decreases.

it deviates from its path and continues to do so as the gait is executed. Interestingly, the resultant trajectories are reminiscent of the "parallel parking" gait described in [72].

A second observation for this example is that the path deviations are more pronounced for small k_s; as k_s increases, the resultant trajectory becomes closer to the ideal one. We can also see this effect in Fig. 5-16, which shows the velocity component of the front wheel in the skidding (perpendicular to travel) direction, denoted by $\omega_f \xi$. This quantity is 0 for the no-skid case, and becomes larger as k_s decreases. Finally, we note that while the skidding velocities for the $k_s = 0.1$ and $k_s = 1$ cases are qualitatively similar, the corresponding trajectories in Fig. 5-15 are still very different, as the snakeboard is spinning more than translating in the former case.

Motion Planning Solution

Given our new model of system behavior, we would still like to derive explicit controllers for the shape inputs to track a given trajectory. A first approach would be to reuse the body velocity relationships with the desired trajectory (5.19). If we substitute these equations into (5.28), we can then numerically solve for inputs that move

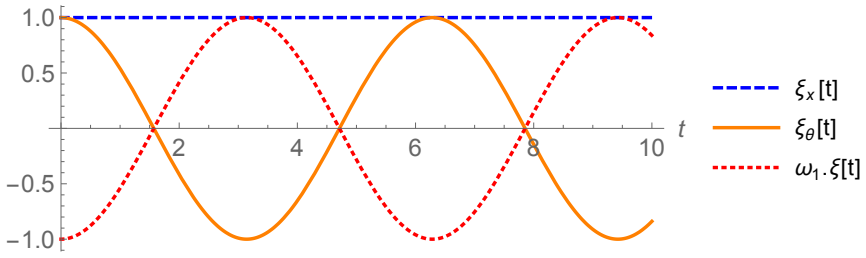

Figure 5-17: Body velocities while executing the serpenoid curve with locked wheels. All turning is effected by skidding.

the system around *as if the constraints were in place*.

$$0 = -M\ddot{r} + k_s(L\sin(2\phi)c - 2\sin^2(\phi))\dot{r} \tag{5.30}$$
$$J_r\ddot{\psi} = -ML^2(c\ddot{r} + \dot{c}\dot{r}) + k_sL(\sin(2\phi) - 2L\cos^2(\phi)c)\dot{r}$$

Given that we know the parameterization of the desired trajectory in $r(t)$ and $c(t)$, we can solve the first line of (5.30) for ϕ, followed by the solution for $\ddot{\psi}$ from the second.

One implication of this solution is that for locomotion with constant forward velocity ($\ddot{r} = 0$), a trivial solution is that $\phi = 0$, regardless of the path curvature. Any change in orientation will be effected by the skidding velocity component, which in turn comes solely from the rotor input. Consider again the serpenoid trajectory with $c(t) = \cos(t)$ and constant forward velocity $\dot{r} = 1$. The snakeboard is able to perfectly execute this gait without rotating its wheels; Fig. 5-17 shows the corresponding body and skidding velocities over time. This kind of locomotion would be impossible with the hard constraints in place, since rotor actuation has no effect when the wheels are locked at $\phi = 0$.

However, if we desire acceleration such that $\ddot{r} \neq 0$, then the space of valid exact solutions for this controller is actually quite restricted. In particular, the first line of (5.30) will yield a solution for ϕ only if the ratio $|\ddot{r}/\dot{r}|$ is bounded by a threshold dependent on the system parameters and path curvature. This also implies that the snakeboard cannot start from rest while exactly following a given path.

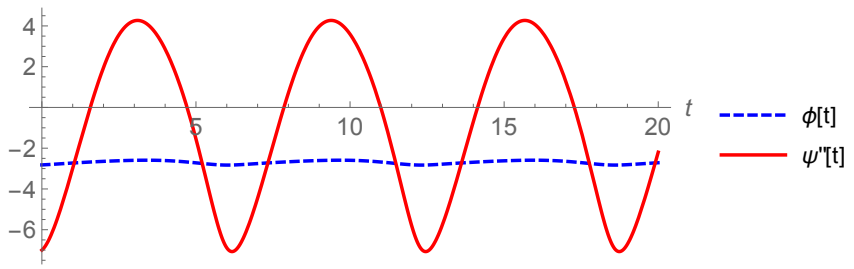

Figure 5-18: Shape inputs for a trajectory with varying speed over terrain with skidding constant $k_s = 10$.

To illustrate this point, we simulate and solve for the shape inputs to execute the following trajectory: $\dot{r}(t) = 4 + \sin(t)$, $c(t) = 0.5$. This commands the snakeboard to locomote around a circle of constant curvature but with oscillating speed; here, we used a skidding coefficient of $k_s = 10$. The solved shape inputs are shown in Fig. 5-18. This trajectory is only possible since the system starts off with nonzero speed. If the system loses forward velocity ($\dot{r}$ decreases), navigates a wider turn ($c(t)$ decreases), or experiences greater skidding (k_s decreases), then an exact solution may not exist.

5.4 Summary

In this chapter we have discussed several examples of locomoting systems that are affected by interactions with the ambient medium. A simple case is that of a constant force field, such as gravity, acting on a locomoting robot. We showed with the three-link robot how one may exploit this external force to get into unique configurations. This allowed us to develop a switching control strategy utilizing combinations of locked, passive, and actuated joints in order to alternate between kinematic and dynamic motions.

A different example was one in which we were able to actively control the underlying medium, in the case of the three-link robot on a movable platform. The presence of the platform required an addition to the original configuration space; due to preservation of symmetries in the new configuration variables, we were able to derive a second connection mapping for the external fiber space. Both connections

then inform the solution of finding specific platform inputs to achieve desired robot motions, for example using the harmonic balance method to analyze the periodic responses of the robot's joints. Finally, we also considered in this example the problem of the relative orientation affecting the system dynamics, if specifying the platform position and velocity in an inertial frame. By using the fact that this dependency is generally periodic, we found representative connections and curvature plots in the same reduced shape space for specific ranges of relative orientation.

Finally, we addressed the problem of motion planning in the presence viscous friction. For this chose to discuss the snakeboard, a dynamic system with an analytical motion planning solution derived in previous work. We showed that the geometric nature of the solution actually allowed for the incorporation of the dissipation function directly into the solution for the inputs, providing an easy way to compensate for friction damping the robot's movement. For the case of skidding, we replaced the system's hard constraints with a different dissipation function and found certain conditions for which the robot is still able to exhibit regular behavior.

Chapter 6

Conclusions and Future Work

6.1 Summary of Contributions

We have expanded the usage of ideas and tools from geometric mechanics to understand a larger landscape of locomoting systems. Whereas systems that were previously treated fell under a number of idealized assumptions, this thesis attempts to remove such assumptions in order to increase the utility of these analytical methods for more realistic or physical systems. In particular, we considered systems with passive joint dynamics and systems influenced by external interactions, all while staying within the framework of the principal fiber bundle structure.

For systems with non-trivially actuated base degrees of freedom, we noted the complexities of the emergent dynamics. However, it is still possible to use geometric structure that may have existed previously, as changing the actuation does not invalidate the underlying system configuration. The example of the multi-link nonholonomic snake robot was required to have passive joints in order to preserve all constraints. For this system, we derived both kinematic and dynamic models of its locomotion. In both cases, tools such as connection curvature functions and harmonic analysis were used to understand the passive joint kinematics and dynamics. Such analyses were naturally complementary to previous work exploiting the geometric nature of the three-link snake robot. Finally, we also performed experiments verifying our locomotion models.

Separately from systems that have various internal dynamics, we also focused on systems that locomote due to or in spite of external dynamics and interactions. This would typically lead to a different problem structure, such as that of a stratified fiber bundle to account for different components of the system configuration. More than one connection would emerge, and we use these mappings in different ways depending on where the "inputs" and "outputs" of the system are located. An example of the flexibility of this problem was whether the inputs were supplied to the robot and then transferred to a platform or vice versa, These external interaction problems also typically break symmetries, such as that of the orientation of a robot moving in response to an external platform or in a gravitational field. While such problems are more difficult to model, we can still find approximations to perform reduction, such as locking a joint degree of freedom as part of the motion plan or finding representative connections for a given range of orientations. Finally, dissipative friction is a special case of external forces that we addressed for the snakeboard system; rather than exploiting this effect for locomotion, we showed that the system can overcome it and locomote as if friction were not acting on it at all.

6.2 Future Work

The contributions of this thesis can neatly follow into several avenues of future work. All of these continue the goal of making geometric methods more amenable to real locomoting systems, particularly via tractable and intuitive control and accounting for environmental considerations.

Sophisticated Motion Controllers

While we have mostly emphasized the utility of using connection curvature functions to visually understand locomotive behavior, there are likely a wide range of sophisticated controls that do not fit into that framework but work well with the new internal or external dynamics that we have considered. In the case of the multi-link robot, we fixedly assume that each joint is either actuated or passive. But it may be possible

to turn combinations of joints on and off to achieve different desired configurations of the remaining joints. This would involve a more thorough investigation of how the passive joint responses change in the adjacent and non-adjacent commanded cases, as well as how to provably avoid locking configurations. In our dynamic analysis, the gaits that we considered are sufficient to propel and orient the robot in arbitrary directions, but they have all emerged to be symmetric about one of the shape space diagonals (*i.e.*, they cross singularities). While offset gaits like those of the kinematic model may not necessarily provide new locomotion modes, it may be interesting to see whether a greater variety of gaits can indeed be induced.

A More United Framework

The similarities in some of our methods for dealing with both internal and external dynamics hint that it may be possible to develope a more united framework for these different classes of systems. For example, the inversion of the connection mapping when pushing trajectories from one fiber to another in a stratified structure was done by analyzing the harmonics of the passive joint variables, in a manner very similar to that of a system with both actuated and passive base degrees of freedom.

It would also be desirable to link these results back to biological locomoting systems, from which many of the original ideas in locomoting robots had their inspiration. For example, snake robots often locomote using slithering motions similar to those of biological snakes. Since we have found that it is possible for a robot to to move in this way without actuating all of its joints, a comparison to observations of a snake's muscle actuation during movement would shed some light into the "naturalness" of this behavior. In addition, many organisms are often seen exploiting the forces in the ambient medium to move, such as fish swimming through the vortex wakes of their neighbors while exerting less effort.

Learning and Closing the Loop

An important aspect of matching models to reality is to derive the models from physical observations and experiments in the first place. This approach is especially

important when the system of interest is much too complicated for the governing physics to produce a sufficiently reduced model, such as when dealing with frictional forces at high speeds or fluids that are neither fully inviscid nor fully viscous. In these cases, we can utilize reinforcement learning methods or model-predictive control to empirically qualify these systems, but with an emphasis on preserving a reduced structure that fits into previously established "ideal" frameworks. This effort would also be useful for verification of approximations and assumptions that we preemptively make when deriving our models from the underlying physics.

Appendix A

Supplementary Example: Interacting Spherical Swimmers

In this section we provide a supplementary example of a hydrodynamic system that exhibits external interactions among multiple locomoting agents. Like the robot-platform system, locomotion arises due to the underlying medium, but in this example the medium *facilitates* interaction among two or more agents rather than causing locomotion directly. The broken symmetry in this case is required for locomotion, as a spherical swimmer attempting to achieve goemetric phase in isolation would not be successful.

A.1 Hollow Spheres Model

We refer to the model shown in Fig. A-1, which shows two spherical bodies with internal masses in an ideal fluid. The indicated axis connecting the centers of the two spheres, or line of centers, is particularly useful for approximating the motions of the two bodies. The derivation of the dynamics is done in detail by [50] and [61]; here, we briefly summarize the key points, since we want to focus on the geometric structure of the problem rather than the specific interaction model. We start with a hollow spheres model, assuming no internal masses.

From Fig. A-1, we see that a "body" frame $\{x^b, y^b\}$ can be defined and attached

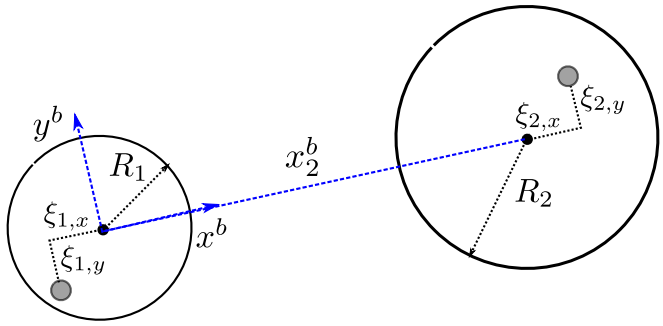

Figure A-1: Two spherical swimmers with radii R_1 and R_2, each with an internal mass. A body frame is attached to one body and oriented along the line of centers; the distance between the two bodies is x_2^b. The positions of the internal masses can be expressed relative to their respective sphere centers.

to one of the two spheres, just as we did in defining a body frame on the three-link robot. The difference here is that the orientation of the frame will change with the *displacement* of the second sphere relative to it, so that y_2^b is always zero. Thus, the frame is aligned with the line of centers connecting the two bodies. The velocities of the spheres relative to this frame are $(\dot{x}_1^b, \dot{y}_1^b)$ and $(\dot{x}_2^b, \dot{y}_2^b)$, their radii are R_1 and R_2, and their masses m_1 and m_2. The surrounding ideal fluid has density ρ.

The motion of the spheres within the fluid induces a velocity potential ϕ, which must everywhere satisfy Laplace's equation, $\nabla^2\phi = 0$. The boundary conditions are that the fluid is at rest infinitely far away from the spheres, while the motion of the spheres leads to a flux boundary condition on the bodies' surfaces. As we showed in our previous work ([23]), a useful way of approximating the latter condition is to superimpose the component corresponding to the spheres moving along the line of centers (thus ensuring that $\dot{y}_i^b = 0$ for both spheres) with the component corresponding to motion perpendicular to the line of centers ($\dot{x}_i^b = 0$).

The boundary condition can thus be approximated as

$$-\frac{\partial}{\partial n}\phi(x^b, y^b) = \frac{x^b\dot{x}_1^b + y^b\dot{y}_1^b}{R_1} + \frac{(x^b - x_2^b)\dot{x}_2^b + y^b\dot{y}_2^b}{R_2}, \tag{A.1}$$

where $-\frac{\partial\phi}{\partial n}$ is the flux going into each of the sphere surfaces. This flux can be viewed as a linear combination of the velocity components of each sphere. For example, suppose that the motion of the first sphere is entirely along the line of centers ($\dot{y}_1^b = 0$). In

that case, the flux component of the first term is maximal when $x^b = \pm R$ (the two antipodes on the equator) and minimal when $x^b = 0$ (the two poles).

A solution can be obtained for ϕ in the form of an infinite series using the method of image doublets ([50, 61]). The kinetic energy of the fluid is given by the integration

$$T_{hs} = -\frac{1}{2}\rho \int \phi \frac{\partial \phi}{\partial n}\, \mathrm{d}S_1 - \frac{1}{2}\rho \int \phi \frac{\partial \phi}{\partial n}\, \mathrm{d}S_2 \tag{A.2}$$

over the surfaces of each sphere, denoted by S_1 and S_2. The idea here is that $-\frac{\partial \phi}{\partial n}$ is the normal fluid velocity into each sphere, and $\rho\phi$ is an impulse that generates the motion. Integrating their product over both of the sphere surfaces then gives us the total kinetic energy from their motion.

Again, the full solution of ϕ is an infinite series whose higher-order terms can be effectively ignored, since the two spheres cannot approach arbitrarily close to each other due to their finite radii. An analytical form for the kinetic energy can be written as

$$T_{hs} = \frac{1}{2}M_1((\dot{x}_1^b)^2 + (\dot{y}_1^b)^2) + \frac{1}{2}M_2((\dot{x}_2^b)^2 + (\dot{y}_2^b)^2) - N\left(\dot{x}_1^b\dot{x}_2^b - \frac{1}{2}\dot{y}_1^b\dot{y}_2^b\right) \tag{A.3}$$

where M_i are the *effective masses* of each swimmer and N is a cross-coupling term between the two. Written up to order $(x_2^b)^{-6}$, they are

$$M_i = m_i + \frac{2}{3}\pi\rho R_i^3\left(1 + \frac{3R_1^3R_2^3}{(x_2^b)^6}\right), \quad i = 1, 2;$$
$$N = 2\pi\rho\frac{R_1^3R_2^3}{|x_2^b|^3}.$$

For the simulations that we perform, higher-order terms are negligible even when the spheres are adjacent to each other. The relative contributions of these terms can be computed for different model parameters, but this truncation is generally sufficient when the two spheres are of similar size.

Finally, if we limit the motion of the spheres to small oscillations, we can use the results of [50] to simplify the dynamics. Assuming the same frequency for all velocity

components, the mean value of the second-order terms in the Lagrange equations will be 0. Along the line of centers, the average forces act on the spheres in opposite directions with magnitude

$$F_x = 3\pi\rho R_1^3 R_2^3 \frac{2[\dot{x}_1^b \dot{x}_2^b] - [\dot{y}_1^b \dot{y}_2^b]}{(x_2^b)^4}, \tag{A.4}$$

where $[\dot{x}_1^b \dot{x}_2^b]$ is the mean value of $\dot{x}_1^b \dot{x}_2^b$ (and similarly for $[\dot{y}_1^b \dot{y}_2^b]$). The mean of the product of two sinusoidal functions differing by a phase is positive if the phase is less than a quarter period and negative otherwise. Then if the overall numerator of Eq. (A.4) is positive, the spheres experience repulsion from each another; otherwise, the spheres experience an attractive force toward each other. Although the magnitude of F_x varies inversely with the spheres' distances from each other, we need not worry about F_x becoming unbounded since we assume finite, rigid radii for both spheres.

Finally, there are also forces acting on the bodies *perpendicular* to their line of centers. They are given as

$$\begin{aligned} F_{y,1} &= 3\pi\rho R_1^3 R_2^3 \frac{[(\dot{x}_2^b - \dot{x}_1^b)\dot{y}_2^b]}{(x_2^b)^4}, \\ F_{y,2} &= 3\pi\rho R_1^3 R_2^3 \frac{[(\dot{x}_2^b - \dot{x}_1^b)\dot{y}_1^b]}{(x_2^b)^4}. \end{aligned} \tag{A.5}$$

Unlike the forces along the line of centers, this one does not act equally on both bodies in opposite directions. Instead, the two magnitudes will vary if $\dot{y}_2^b$ and $\dot{y}_1^b$ are different.

A.2 Adding Internal Masses

We now consider the presence of a small mass inside each sphere, each of which can move as an actuation mechanism for the spheres. If the masses inside swimmer 1 and swimmer 2 are μ_1 and μ_2, respectively, and their configurations measured from their

respective sphere centers are $(\xi_{1,x}, \xi_{1,y})$ and $(\xi_{2,x}, \xi_{2,y})$, then their kinetic energy is

$$T_\mu = \frac{\mu_1}{2}((\dot{\xi}_{1,x})^2 + (\dot{\xi}_{1,y})^2) + \frac{\mu_2}{2}((\dot{x}_2^b + \dot{\xi}_{2,x})^2 + (\dot{\xi}_{2,y})^2). \tag{A.6}$$

The total kinetic energy of the system is then $T = T_{hs} + T_\mu$, and we can use this to obtain the updated equations of motion and description of forces on the spheres. In particular, exciting μ_1 and μ_2 with periodic oscillations ensures that the force contributions from T_μ have a mean value of 0, so Eqs. (A.4) and (A.5) acting on the spheres remain unchanged.

We now recast this problem into the principal bundle formulation. We have a base space $B = \mathbb{R}^2 \times \mathbb{R}^2$ formed by all possible mass configurations $(\xi_{1,x}, \xi_{1,y}, \xi_{2,x}, \xi_{2,y})$ and a set of fibers $\mathbb{R}^2 \times \mathbb{R}^2$ defined by the positions $(x_1^b, y_1^b, x_2^b, y_2^b)$ over B. Because of our definition of the "body frame," none of the equations derived in the previous subsection have an explicit dependence on the fiber variables, with the exception of x_2^b. This is thus a symmetry-breaking fiber variable, capturing the role that the distance between the two bodies plays in determing their interaction. In addition, unlike with θ for the robot-platform system, x_2^b generally does not have periodic trajectories in the long term (*i.e.*, the bodies may oscillate but may also displace).

In cases in which the spheres are sufficiently far away from each other, we can make the following approximation of a principal connection. Momentum conservation dictates the response of each sphere due to actuation of its own internal mass, ignoring the presence of the other sphere. This gives us a constant, diagonal *mechanical connection* relating the mass velocities to the sphere's perturbation velocities as

$$\begin{pmatrix} \dot{x}_{1,k} \\ \dot{y}_{1,k} \\ \dot{x}_{2,k} \\ \dot{y}_{2,k} \end{pmatrix} = - \begin{pmatrix} \frac{\mu_1}{\mu_1+M_1} & 0 & 0 & 0 \\ 0 & \frac{\mu_1}{\mu_1+M_1} & 0 & 0 \\ 0 & 0 & \frac{\mu_2}{\mu_2+M_2} & 0 \\ 0 & 0 & 0 & \frac{\mu_2}{\mu_2+M_2} \end{pmatrix} \begin{pmatrix} \dot{\xi}_{1,x} \\ \dot{\xi}_{1,y} \\ \dot{\xi}_{2,x} \\ \dot{\xi}_{2,y} \end{pmatrix}. \tag{A.7}$$

In other words, we explicitly separate each fiber component $(x_i^b, y_i^b) = (x_{i,k}, y_{i,k}) + (x_{i,d}, y_{i,d})$. The first component solely captures the kinematic, oscillatory response

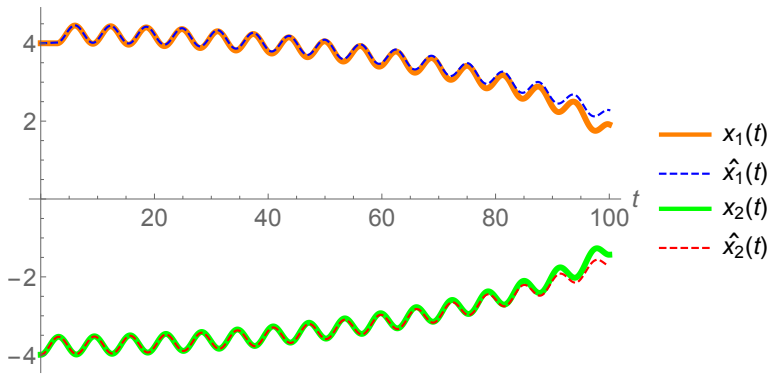

Figure A-2: The attraction of two spheres in response to out-of-phase perturbations of their internal masses. Solid trajectories $x_i(t)$ are computed via the full equations of motion; the dashed $\hat{x}_i(t)$ are a sum of individual and coupled approximations.

of the spheres due to interaction with their internal masses. The second component captures the dynamic displacement of the spheres due to their interaction with each other.

Thus, given known actuation of the internal masses, we first use Eq. (A.7) to find the resultant oscillations. These are then used in a modified version of the external force from Eqs. (A.4) and (A.5) to find the external interactions as

$$\begin{aligned}
\tilde{F}_x &= 3\pi\rho R_1^3 R_2^3 \frac{2[\dot{x}_{1,k}\dot{x}_{2,k}] - [\dot{y}_{1,k}\dot{y}_{2,k}]}{(x_{2,d})^4}, \\
\tilde{F}_{y,1} &= 3\pi\rho R_1^3 R_2^3 \frac{[(\dot{x}_{2,k} - \dot{x}_{1,k})\dot{y}_{2,k}]}{(x_{2,d})^4}, \\
\tilde{F}_{y,2} &= 3\pi\rho R_1^3 R_2^3 \frac{[(\dot{x}_{2,k} - \dot{x}_{1,k})\dot{y}_{1,k}]}{(x_{2,d})^4}.
\end{aligned} \tag{A.8}$$

The sum of the two responses, one kinematic and one dynamic, approximates the complete motion of the system. An example simulation showing the validity of this approximation is shown in Fig. A-2. We set the parameters $\rho = 1$, $R_1 = R_2 = 2$, $m_1 = m_2 = 0$, $\mu_1 = \mu_2 = 5$, and command the inputs $\xi_{1,x} = \cos t$, $\xi_{2,x} = \cos(t - \frac{11\pi}{12})$. For this simulation we constrain motion to occur along the line of centers, so that $\xi_{i,y}$, $\dot{y}_{i,k}$, and $\tilde{F}_{y,i}$ are all zero.

Our first observation is that because the spheres' oscillations are nearly a half-cycle out of phase with each other, the forces on each are attractive, verifying Lamb's

assertion. Furthermore, the trajectories $\hat{x}_i(t)$ obtained from superimposing the individual and coupled responses of the spheres follow very closely the actual trajectories $x_i(t)$ from the full equations of motion. They only begin to diverge around $t = 90$ as the spheres nearly collide. On the other hand, if the spheres were actuated so as to repel each other, this approximation would hold throughout.

A.3 Simplifying Motion Primitives

The value of the numerator terms of Eq. (A.8) can be arbitrarily designed by choosing the desired oscillations with the right amplitude and phase. In particular, if all oscillation components take the form

$$\begin{aligned}\dot{x}_{i,k} &= A_{x,i}\cos(\omega t - \phi_{x,i}),\\ \dot{y}_{i,k} &= A_{y,i}\cos(\omega t - \phi_{y,i}),\end{aligned}$$

then Eq. (A.8) can be simplified to

$$\begin{aligned}\tilde{F}_x &= \frac{3\pi\rho R_1^3 R_2^3}{(x_{2,d})^4}\Big(A_{x,1}A_{x,2}\cos(\phi_{x,1}-\phi_{x,2}) - \frac{1}{2}A_{y,1}A_{y,2}\cos(\phi_{y,1}-\phi_{y,2})\Big),\\ \tilde{F}_{y,1} &= \frac{3\pi\rho R_1^3 R_2^3}{(x_{2,d})^4}\frac{A_{y,2}}{2}\Big(A_{x,2}\cos(\phi_{x,2}-\phi_{y,2}) - A_{x,1}\cos(\phi_{x,1}-\phi_{y,2})\Big),\\ \tilde{F}_{y,2} &= \frac{3\pi\rho R_1^3 R_2^3}{(x_{2,d})^4}\frac{A_{y,1}}{2}\Big(A_{x,2}\cos(\phi_{x,2}-\phi_{y,1}) - A_{x,1}\cos(\phi_{x,1}-\phi_{y,1})\Big).\end{aligned} \tag{A.9}$$

These equations effectively render all of the numerators as constants, since all time dependence is eliminated. Producing a desired amount of force in the numerator term then becomes a problem of solving the above nonlinear equations for the oscillation parameters.

However, $x_{2,d}$ still appears in the denominators, generally changing the effective forces on the bodies as they locomote. This difficulty normally necessitates an integration to find the resultant trajectories of the spheres, but certain motion primitives can simplify or avoid this problem altogether. We propose three motion primitives—attraction or repulsion, parallel motion, and orbiting around their centroid. The first

type has $\tilde{F}_x \neq 0$, $\tilde{F}_{y,i} = 0$, and the second two types have $\tilde{F}_x = 0$, $\tilde{F}_{y,i} \neq 0$.

Attraction and Repulsion

We have already shown how to induce either attraction or repulsion along the line of centers only using different phase relationships in the input oscillations, *e.g.* in Fig. A-2. In both cases, the $\dot{y}_{i,k}$ component velocities were zero, leading to zero net forces on the spheres in the y^b direction. This can also be achieved if both $\dot{x}_{i,k}$ component velocities are zero and both $\dot{y}_{i,k}$ components are nonzero. In either case, we have that $\tilde{F}_{y,1} = \tilde{F}_{y,2} = 0$ and the displacement between the two spheres evolves as

$$\ddot{x}_{2,d} \sim (x_{2,d})^{-4}.$$

The numerical solution of this differential equation can then be used to inform the scaling in the numerator of the first line of Eq. (A.9). For example, as $x_{2,d}$ decreases, the acceleration $\ddot{x}_{2,d}$ and force along the line of centers $\tilde{F}_x$ increases rapidly. Thus, in order to maintain a constant force, the oscillation velocities must be correspondingly reduced, which is easily done by simply scaling the inputs. The opposite would hold if $x_{2,d}$ were to increase, with the force $\tilde{F}_x$ dropping off very quickly.

Parallel Motion

When the spheres move parallel to each other, $x_{2,d}$ remains constant, while $\tilde{F}_x = 0$ and $\tilde{F}_{y,1} = \tilde{F}_{y,2}$. The easiest way to achieve these conditions is to first ensure that $\dot{y}_{1,k} = \dot{y}_{2,k}$, leading to equal forces acting on both spheres in the direction perpendicular to the line of centers. Then to have $\tilde{F}_x = 0$, we can simultaneously solve this nonlinear equation (using the first line of Eq. (A.9)) and either of the two $\tilde{F}_{y,i}$ equations (since they are identical) for the desired amount of force.

Orbit Around Centroid

The last motion primitive for which Eq. (A.8) is useful is for the spheres to orbit their centroid, thus keeping $x_{2,d}$ constant. This type of motion allows for the relative

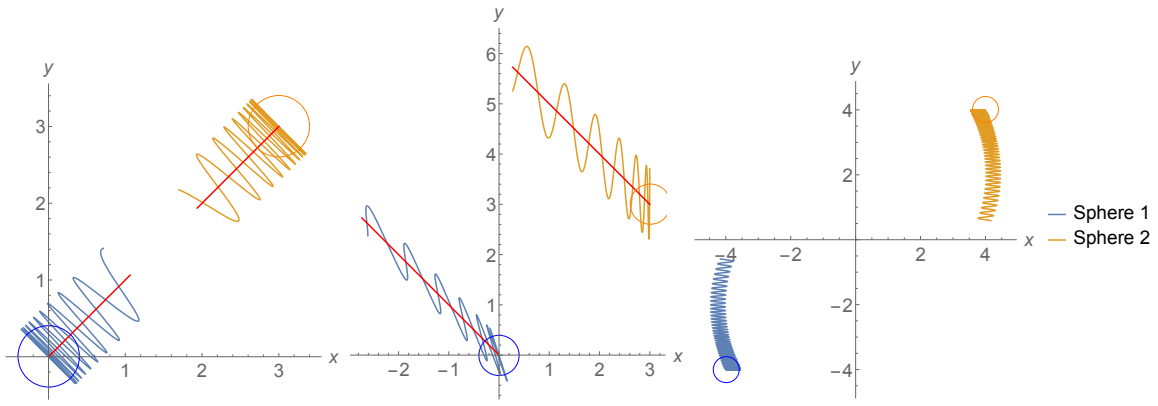

Figure A-3: The three types of motion primitives that can be easily effected using Eq. (A.9). The first type, motion along the line of centers, was detailed previously and only relies on $\tilde{F}_x$ to change $x_{2,d}$. The other two, parallel and orbital motion, keep $x_{2,d}$ relatively constant and thus can be planned without regard to the evolution of the spheres' configurations.

reorientation of the two bodies, which, when combined with displacement along and perpendicular to the line of centers, leads to coverage of the entire plane. The first condition for this motion is that $\tilde{F}_{y,1} = -\tilde{F}_{y,2}$, which can be achieved if $\dot{y}_{1,k} = -\dot{y}_{2,k}$. Secondly, $\tilde{F}_x$ must act attractively on the spheres with the same magnitude as $\tilde{F}_{y,i}$. These two stipulations thus inform the space of acceptable inputs for both $\dot{x}_{i,k}$ and $\dot{y}_{i,k}$.

Stitching Primitives Together

Simulations depicting the three types of motion primitives are shown in Fig. A-3. In each of them, the spheres start at the positions indicated by the circles, and undergo the trajectories shown in their respective colors. The overlays in red depict the mean trajectories of the spheres. Note that in all of them, we can command oscillations to the spheres so that they are able to execute their motions despite an arbitrary starting orientation. This is particularly striking in the middle figure, in which the spheres undergo parallel locomotion. The input oscillations to each sphere are not symmetric, but their overall motions are still the same since the forces in the *body frame* are identical.

These three motion primitives can be concatenated in various combinations to

move two bodies to any two planar locations to cover all of $\mathbb{R}^2$. A systematic way of doing so is as follows. Suppose we want to move the two bodies from their current *inertial* locations (x_1, y_1) and (x_2, y_2) to two desired inertial locations (x_1^*, y_1^*) and (x_2^*, y_2^*). We also define the quantities

$$d^* = \sqrt{(y_2^* - y_1^*)^2 + (x_2^* - x_1^*)^2},$$
$$\theta^* = \text{atan2}(y_2^* - y_1^*, x_2^* - x_1^*).$$

Then we simply execute the following motions in order:

1. Use attraction or repulsion to move the bodies along their current line of centers such that $d_{2,x} = d^*$.

2. The bodies should then undergo an orbital motion so that their relative orientation $\theta = \theta^* \pm \frac{\pi}{2}$. The bodies are now aligned orthogonally to their desired final locations.

3. The bodies undergo parallel motion such that their current line of centers intersects the centroid of the desired locations. In other words,

$$\frac{1}{2}(x_1^* + x_2^*) = x_1 + c(x_2 - x_1),$$
$$\frac{1}{2}(y_1^* + y_2^*) = y_1 + c(y_2 - y_1)$$

   for some constant c.

4. Undo the orbital motion from Step 2 and align the bodies such that θ is equal to θ^*.

5. The two displacement vectors between each body and its respective final location are now parallel to each other. Thus, a final parallel movement is sufficient to finish the sequence.

This particular concatenation of motion primitives allow two bodies to move from any two initial positions to any two desired positions in the plane. This is of course

in contrast to the case of a single spherical body by itself, which is unable to achieve any net locomotion at all.

Bibliography

[1] Ralph Abraham, Jerrold E Marsden, and Jerrold E Marsden. *Foundations of Mechanics*, volume 36. Benjamin/Cummings Publishing Company Reading, Massachusetts, 1978.

[2] J. E. Avron, O. Gat, and O. Kenneth. Optimal swimming at low reynolds numbers. *Physical Review Letters*, 93(18):186001, 2004.

[3] J. E. Avron and O. Raz. A geometric theory of swimming: Purcell's swimmer and its symmetrized cousin. *New Journal of Physics*, 10(6):063016, 2008.

[4] Andrew Baker. *Matrix Groups: An Introduction to Lie Group Theory*. Springer Science & Business Media, 2012.

[5] Salah Bazzi, Elie Shammas, and Daniel Asmar. Novel modeling of skidding effects on the nonholonomic motion of a vertical rolling disk. In *2013 16th International Conference on Advanced Robotics (ICAR)*, pages 1–6, Nov 2013.

[6] Salah Bazzi, Elie Shammas, and Daniel Asmar. A novel method for modeling skidding for systems with nonholonomic constraints. *Nonlinear Dynamics*, 76(2):1517–1528, 2014.

[7] Leif E. Becker, Stephan A. Koehler, and Howard A. Stone. On self-propulsion of micro-machines at low reynolds number: Purcell's three-link swimmer. *Journal of Fluid Mechanics*, 490:15–35, 2003.

[8] Randall D. Beer, Roger D. Quinn, Hillel J. Chiel, and Roy E. Ritzmann. Biologically inspired approaches to robotics: What can we learn from insects? *Communications of the ACM*, 40(3):30–38, March 1997.

[9] J. R. Blake. Self propulsion due to oscillations on the surface of a cylinder at low reynolds number. *Bulletin of the Australian Mathematical Society*, 5(02):255–264, 1971.

[10] Anthony M. Bloch, John Baillieul, Peter Crouch, Jerrold E. Marsden, Perinkulam Sambamurthy Krishnaprasad, Richard M. Murray, and Dmitry Zenkov. *Nonholonomic Mechanics and Control*, volume 24. Springer, 2003.

[11] Anthony M. Bloch, P. S. Krishnaprasad, Jerrold E. Marsden, and Richard M. Murray. Nonholonomic mechanical systems with symmetry. *Archive for Rational Mechanics and Analysis*, 136(1):21–99, 1996.

[12] Joel W. Burdick, Jim Radford, and Gregory S. Chirikjian. A 'sidewinding' locomotion gait for hyper-redundant robots. pages 101–106 vol.3, May 1993.

[13] Lisa Burton, Ross L Hatton, Howie Choset, and Anette E. Hosoi. Two-link swimming using buoyant orientation. *Physics of Fluids*, 22(9):091703, 2010.

[14] Stephen Childress. *Mechanics of Swimming and Flying*, volume 2. Cambridge University Press, 1981.

[15] Gregory S. Chirikjian and Joel W. Burdick. A modal approach to hyper-redundant manipulator kinematics. *IEEE Transactions on Robotics and Automation*, 10(3):343–354, 1994.

[16] Gregory S. Chirikjian and Joel W. Burdick. The kinematics of hyper-redundant robot locomotion. *IEEE Transactions on Robotics and Automation*, 11(6):781–793, 1995.

[17] Sachin Chitta, Peng Cheng, Emilio Frazzoli, and Vijay Kumar. Robotrikke: A novel undulatory locomotion system. In *Proceedings of the 2005 IEEE International Conference on Robotics and Automation*, pages 1597–1602. IEEE, 2005.

[18] J. Edward Colgate and Kevin M. Lynch. Mechanics and control of swimming: A review. *IEEE Journal of Oceanic Engineering*, 29(3):660–673, 2004.

[19] James J. Collins and Ian N. Stewart. Coupled nonlinear oscillators and the symmetries of animal gaits. *Journal of Nonlinear Science*, 3(1):349–392, 1993.

[20] Steve Collins, Andy Ruina, Russ Tedrake, and Martijn Wisse. Efficient bipedal robots based on passive-dynamic walkers. *Science*, 307(5712):1082–1085, 2005.

[21] Peter Crouch. Spacecraft attitude control and stabilization: Applications of geometric control theory to rigid body models. *IEEE Transactions on Automatic Control*, 29(4):321–331, 1984.

[22] Tony Dear, Ross L. Hatton, Matthew Travers, and Howie Choset. Snakeboard motion planning with local trajectory information. In *ASME 2013 Dynamic Systems and Control Conference*, pages V002T33A002–V002T33A002. American Society of Mechanical Engineers, 2013.

[23] Tony Dear, Scott David Kelly, and Howie Choset. Control and locomotion of hydrodynamically coupled rigid spheres. In *American Control Conference (ACC), 2017*, pages 4845–4850. IEEE, 2017.

[24] Tony Dear, Scott David Kelly, Matthew Travers, and Howie Choset. Mechanics and control of a terrestrial vehicle exploiting a nonholonomic constraint for fishlike locomotion. In *ASME 2013 Dynamic Systems and Control Conference*, pages V002T33A004–V002T33A004. American Society of Mechanical Engineers, 2013.

[25] Tony Dear, Scott David Kelly, Matthew Travers, and Howie Choset. Dissipation-induced self-recovery in systems on principal bundles. In *ASME 2014 Dynamic Systems and Control Conference*, pages V001T11A004–V001T11A004. American Society of Mechanical Engineers, 2014.

[26] Tony Dear, Scott David Kelly, Matthew Travers, and Howie Choset. Motion planning and differential flatness of mechanical systems on principal bundles. In *ASME 2015 Dynamic Systems and Control Conference*, pages V003T40A002–V003T40A002. American Society of Mechanical Engineers, 2015.

[27] Tony Dear, Scott David Kelly, Matthew Travers, and Howie Choset. Snakeboard motion planning with viscous friction and skidding. In *2015 IEEE International Conference on Robotics and Automation (ICRA)*, pages 670–675. IEEE, 2015.

[28] Manfredo Perdigao Do Carmo. *Differential geometry of curves and surfaces*, volume 2. Prentice-hall Englewood Cliffs, 1976.

[29] Kenneth S. Espenschied, Roger D. Quinn, Randall D. Beer, and Hillel J. Chiel. Biologically based distributed control and local reflexes improve rough terrain locomotion in a hexapod robot. *Robotics and Autonomous Systems*, 18(1):59 – 64, 1996.

[30] Yasuhiro Fukuoka, Hiroshi Kimura, and Avis H. Cohen. Adaptive dynamic walking of a quadruped robot on irregular terrain based on biological concepts. *The International Journal of Robotics Research*, 22(3-4):187–202, 2003.

[31] Ramin Golestanian and Armand Ajdari. Analytic results for the three-sphere swimmer at low reynolds number. *Physical Review E*, 77(3):036308, 2008.

[32] Ramin Golestanian, Julia M. Yeomans, and Nariya Uchida. Hydrodynamic synchronization at low reynolds number. *Soft Matter*, 7(7):3074–3082, 2011.

[33] Sten Grillner. *Control of Locomotion in Bipeds, Tetrapods, and Fish*. John Wiley and Sons, Inc., 2011.

[34] John Guckenheimer and Philip Holmes. *Nonlinear oscillations, dynamical systems, and bifurcations of vector fields*, volume 42. Springer Science & Business Media, 2013.

[35] Ross L. Hatton. *Geometric Mechanics of Locomotion and Optimal Coordinate Choice*. PhD thesis, Carnegie Mellon University, Pittsburgh, 2011.

[36] Ross L. Hatton and Howie Choset. Geometric motion planning: The local connection, stokes theorem, and the importance of coordinate choice. *The International Journal of Robotics Research*, 30(8):988–1014, 2011.

[37] Chihiro Hayashi. *Nonlinear oscillations in physical systems*. Princeton University Press, 2014.

[38] Shigeo Hirose. A study of design and control of a quadruped walking vehicle. *The International Journal of Robotics Research*, 3(2):113–133, 1984.

[39] Shigeo Hirose. *Biologically Inspired Robots: Serpentile Locomotors and Manipulators*. Oxford University Press, 1993.

[40] Shigeo Hirose and Makoto Mori. Biologically inspired snake-like robots. In *IEEE International Conference on Robotics and Biomimetics, 2004. ROBIO 2004.*, pages 1–7. IEEE, 2004.

[41] Qiang Huang, Kazuhito Yokoi, Shuuji Kajita, Kenji Kaneko, Hirohiko Arai, Noriho Koyachi, and Kazuo Tanie. Planning walking patterns for a biped robot. *IEEE Transactions on Robotics and Automation*, 17(3):280–289, Jun 2001.

[42] Takuji Ishikawa, M. P. Simmonds, and T. J. Pedley. Hydrodynamic interaction of two swimming model micro-organisms. *Journal of Fluid Mechanics*, 568:119–160, 2006.

[43] Hugh F Jones. *Groups, Representations and Physics*. CRC Press, 1998.

[44] Scott David Kelly and Rodrigo Abrajan-Guerrero. Propulsive heading control and damping-induced heading recovery for a free hydrofoil with an internal rotor.

[45] Scott David Kelly, Michael J. Fairchild, Peter M. Hassing, and Phanindra Tallapragada. Proportional heading control for planar navigation: The chaplygin beanie and fishlike robotic swimming. pages 4885–4890, June.

[46] Scott David Kelly and Richard M. Murray. The geometry and control of dissipative systems. In *Proceedings of the 35th IEEE Conference on Decision and Control*, volume 1, pages 981–986. IEEE, 1996.

[47] Scott David Kelly, Parthesh Pujari, and Hailong Xiong. Geometric mechanics, dynamics, and control of fishlike swimming in a planar ideal fluid. In *Natural Locomotion in Fluids and on Surfaces*, pages 101–116. Springer, 2012.

[48] Hiroshi Kimura, Yasuhiro Fukuoka, and Avis H. Cohen. Adaptive dynamic walking of a quadruped robot on natural ground based on biological concepts. *The International Journal of Robotics Research*, 26(5):475–490, 2007.

[49] Donald L. Koch and Ganesh Subramanian. Collective hydrodynamics of swimming microorganisms: Living fluids. *Annual Review of Fluid Mechanics*, 43:637–659, 2011.

[50] Horace Lamb. *Hydrodynamics*. Cambridge university press, 1932.

[51] Eric Lauga and Thomas R. Powers. The hydrodynamics of swimming microorganisms. *Reports on Progress in Physics*, 72(9):096601, 2009.

[52] Naomi Ehrich Leonard and Jerrold E. Marsden. Stability and drift of underwater vehicle dynamics: Mechanical systems with rigid motion symmetry. *Physica D: Nonlinear Phenomena*, 105(1):130–162, 1997.

[53] Zexiang Li and John F. Canny. *Nonholonomic Mmotion Planning*, volume 192. Springer Science & Business Media, 2012.

[54] Albert CJ Luo and Jianzhe Huang. Approximate solutions of periodic motions in nonlinear systems via a generalized harmonic balance. *Journal of Vibration and Control*, 18(11):1661–1674, 2012.

[55] Jerrold E. Marsden, Richard Montgomery, and Tudor S. Raiu. *Reduction, Symmetry, and Phases in Mechanics*, volume 436. American Mathematical Society, 1990.

[56] Jerrold E. Marsden and Tudor Ratiu. *Introduction to Mechanics and Symmetry: A Basic Exposition of Classical Mechanical Systems*, volume 17. Springer Science & Business Media, 2013.

[57] Jerrold E. Marsden and Jürgen Scheurle. The reduced euler-lagrange equations. *Fields Institute Comm*, 1:139–164, 1993.

[58] Tad McGeer. Passive dynamic walking. *The International Journal of Robotics Research*, 9(2):62–82, 1990.

[59] Juan B. Melli, Clarence W. Rowley, and Dzhelil S. Rufat. Motion planning for an articulated body in a perfect planar fluid. *SIAM Journal on Applied Dynamical Systems*, 5(4):650–669, 2006.

[60] RE Mickens. A generalization of the method of harmonic balance. *Journal of Sound and Vibration*, 111(3):515–518, 1986.

[61] Louis Melville Milne-Thomson. *Theoretical hydrodynamics*. Courier Corporation, 1968.

[62] T. Miloh and A. Galper. Self-propulsion of a maneuvering deformable body in a perfect fluid. In *Proc. Roy. Soc. London A*, volume 442, pages 273–299, 1993.

[63] Kristi A. Morgansen, Benjamin I. Triplett, and Daniel J. Klein. Geometric methods for modeling and control of free-swimming fin-actuated underwater vehicles. *IEEE Transactions on Robotics*, 23(6):1184–1199, 2007.

[64] Makoto Mori and Shigeo Hirose. Development of active cord mechanism acm-r3 with agile 3d mobility. In *Intelligent Robots and Systems, 2001. Proceedings. 2001 IEEE/RSJ International Conference on*, volume 3, pages 1552–1557. IEEE, 2001.

[65] Makoto Mori and Shigeo Hirose. Three-dimensional serpentine motion and lateral rolling by active cord mechanism acm-r3. In *2002 IEEE/RSJ International Conference on Intelligent Robots and Systems*, volume 1, pages 829–834. IEEE, 2002.

[66] Richard M. Murray, Zexiang Li, and S. Shankar Sastry. *A mathematical introduction to robotic manipulation*. CRC press, 1994.

[67] Richard M. Murray and S. Shankar Sastry. Nonholonomic motion planning: Steering using sinusoids. *IEEE Transactions on Automatic Control*, 38(5):700–716, 1993.

[68] Eadweard Muybridge. *Animals in Motion*. Courier Corporation, 2012.

[69] Umashankar Nagarajan, George Kantor, and Ralph Hollis. The ballbot: An omnidirectional balancing mobile robot. *The International Journal of Robotics Research*, 2013.

[70] Yoshihiko Nakamura and Ranjan Mukherjee. Exploiting nonholonomic redundancy of free-flying space robots. *IEEE Transactions on Robotics and Automation*, 9(4):499–506, 1993.

[71] J. N. Newman and Theodore Yao-Tsu Wu. Hydromechanical aspects of fish swimming. In *Swimming and Flying in Nature*, pages 615–634. Springer, 1975.

[72] James P. Ostrowski. Reduced equations for nonholonomic mechanical systems with dissipative forces.

[73] James P. Ostrowski. *The Mechanics and Control of Undulatory Robotic Locomotion*. PhD thesis, California Institute of Technology, 1996.

[74] James P. Ostrowski and Joel W. Burdick. The geometric mechanics of undulatory robotic locomotion. *The International Journal of Robotics Research*, 17(7):683–701, 1998.

[75] James P. Ostrowski, Joel W. Burdick, Andrew D. Lewis, and Richard M. Murray. The mechanics of undulatory locomotion: The mixed kinematic and dynamic case. In *Proceedings of the 1995 IEEE International Conference on Robotics and Automation*, volume 2, pages 1945–1951 vol.2, May 1995.

[76] James P. Ostrowski, Jaydev P. Desai, and Vijay Kumar. Optimal gait selection for nonholonomic locomotion systems. *The International Journal of Robotics Research*, 19(3):225–237, 2000.

[77] James P. Ostrowski, Andrew Lewis, Richard Murray, and Joel W. Burdick. Nonholonomic mechanics and locomotion: The snakeboard example. In *Proceedings of the 1994 IEEE International Conference on Robotics and Automation*, pages 2391–2397. IEEE, 1994.

[78] Emiliya Passov and Yizhar Or. Dynamics of purcells three-link microswimmer with a passive elastic tail. *The European Physical Journal E*, 35(8):1–9, 2012.

[79] C. M. Pooley, G. P. Alexander, and J. M Yeomans. Hydrodynamic interaction between two swimmers at low reynolds number. *Physical Review Letters*, 99(22):228103, 2007.

[80] Edward M. Purcell. Life at low reynolds number. *Am. J. Phys*, 45(1):3–11, 1977.

[81] Victor B. Putz and Julia M. Yeomans. Hydrodynamic synchronisation of model microswimmers. *Journal of Statistical Physics*, 137(5-6):1001–1013, 2009.

[82] J.E. Radford and Joel W. Burdick. Local motion planning for nonholonomic control systems evolving on principal bundles. *A, A*, 1:3, 1998.

[83] Marc H. Raibert. *Legged robots that balance*. The MIT Press, Cambridge, MA, Jan 1985.

[84] Marc H. Raibert, Kevin Blankespoor, Gabriel Nelson, and Rob Playter. Bigdog, the rough-terrain quadruped robot. *IFAC Proceedings Volumes*, 41(2):10822 – 10825, 2008. 17th IFAC World Congress.

[85] Pierre Rouchon, Michel Fliess, Jean Lévine, and Philippe Martin. Flatness, motion planning and trailer systems. In *Proceedings of the 32nd IEEE Conference on Decision and Control*, pages 2700–2705. IEEE, 1993.

[86] P. G. Saffman. The self-propulsion of a deformable body in a perfect fluid. *Journal of Fluid Mechanics*, 28(02):385–389, 1967.

[87] Uluc Saranli, Martin Buehler, and Daniel E. Koditschek. Rhex: A simple and highly mobile hexapod robot. *The International Journal of Robotics Research*, 20(7):616–631, 2001.

[88] Michael Sfakiotakis, David M. Lane, and J. Bruce C. Davies. Review of fish swimming modes for aquatic locomotion. *IEEE Journal of Oceanic Engineering*, 24(2):237–252, Apr 1999.

[89] Elie A. Shammas. *Generalized Motion Planning for Underactuated Mechanical Systems*. PhD thesis, Carnegie Mellon University, Pittsburgh, 2006.

[90] Elie A. Shammas, Howie Choset, and Alfred A. Rizzi. Geometric motion planning analysis for two classes of underactuated mechanical systems. *The International Journal of Robotics Research*, 26(10):1043–1073, 2007.

[91] Elie A. Shammas, Howie Choset, and Alfred A. Rizzi. Towards a unified approach to motion planning for dynamic underactuated mechanical systems with non-holonomic constraints. *The International Journal of Robotics Research*, 26(10):1075–1124, 2007.

[92] Alfred Shapere and Frank Wilczek. Efficiencies of self-propulsion at low reynolds number. *Journal of Fluid Mechanics*, 198:587–599, 1989.

[93] Alfred Shapere and Frank Wilczek. Geometry of self-propulsion at low reynolds number. *Journal of Fluid Mechanics*, 198:557–585, 1989.

[94] Shin-Min Song and Kenneth J. Waldron. *Machines That Walk: The Adaptive Suspension Vehicle*. MIT Press, Cambridge, MA, USA, 1988.

[95] Steven H Strogatz. *Nonlinear dynamics and chaos: with applications to physics, biology, chemistry, and engineering*. CRC Press, 2018.

[96] Daniel Tam and Annete E. Hosoi. Optimal stroke patterns for purcells three-link swimmer. *Physical Review Letters*, 98(6):068105, 2007.

[97] Geoffrey Taylor. Analysis of the swimming of microscopic organisms. In *Proceedings of the Royal Society of London A: Mathematical, Physical and Engineering Sciences*, volume 209, pages 447–461. The Royal Society, 1951.

[98] M. S. Triantafyllou, G. S. Triantafyllou, and D. K. P. Yue. Hydrodynamics of fishlike swimming. *Annual Review of Fluid Mechanics*, 32(1):33–53, 2000.

[99] Gregory C. Walsh and S. Shankar Sastry. On reorienting linked rigid bodies using internal motions. *IEEE Transactions on Robotics and Automation*, 11(1):139–146, 1995.

[100] Eric R. Westervelt, Jessy W. Grizzle, Christine Chevallereau, Jun Ho Choi, and Benjamin Morris. *Feedback Control of Dynamic Bipedal Robot Locomotion*, volume 28. CRC press, 2007.

[101] Stephen Wiggins. *Introduction to applied nonlinear dynamical systems and chaos*, volume 2. Springer Science & Business Media, 2003.

[102] Cornell Wright, Austin Buchan, Ben Brown, Jason Geist, Michael Schwerin, David Rollinson, Matthew Tesch, and Howie Choset. Design and architecture of the unified modular snake robot. In *2012 IEEE International Conference on Robotics and Automation (ICRA)*, pages 4347–4354. IEEE, 2012.

[103] Cornell Wright, Aaron Johnson, Aaron Peck, Zachary McCord, Allison Naaktgeboren, Philip Gianfortoni, Manuel Gonzalez-Rivero, Ross L. Hatton, and Howie Choset. Design of a modular snake robot. In *2007 IEEE/RSJ International Conference on Intelligent Robots and Systems*, pages 2609–2614. IEEE, 2007.

[104] Theodore Yao-Tsu Wu. Hydromechanics of swimming of fishes and cetaceans. *Advances in Applied Mechanics*, 11:1–63, 1971.